Numerical Study of Laser Parameters on the Instability of the Keyhole during Laser Welding

by

Saeid SAEDIARDAHAEI

MANUSCRIPT-BASED THESIS PRESENTED TO ÉCOLE DE TECHNOLOGIE SUPÉRIEURE IN PARTIAL FULFILLEMENT FOR THE DEGREE OF DOCTOR OF PHILOSOPHY
PH.D.

MONTREAL, AUGUST 14, 2025

ÉCOLE DE TECHNOLOGIE SUPÉRIEURE
UNIVERSITÉ DU QUÉBEC

BOARD OF EXAMINERS (THESIS PH.D.)

THIS THESIS HAS BEEN EVALUATED

BY THE FOLLOWING BOARD OF EXAMINERS

Mr. Xuan-Tan Pham, Thesis Supervisor
Department of Mechanical Engineering, École de Technologie Supérieure

Mr. François Duhaime, President of the Board of Examiners
Department of Construction Engineering, École de Technologie Supérieure

Mrs. Marlène Sanjosé, Member of the jury
Department of Mechanical Engineering, École de Technologie Supérieure

Mr. Jacques Lanteigne, External Evaluator
Institut de recherche Hydro-Québec

Mr. Chi-Cong Nguyen, External Member of the jury
Maya Heat Transfer Technologies Ltd.

THIS THESIS WAS PRESENTED AND DEFENDED IN THE PRESENCE OF A BOARD OF EXAMINERS AND PUBLIC ON JULY 3RD, 2025

AT ÉCOLE DE TECHNOLOGIE SUPÉRIEURE

ACKNOWLEDGMENT

Doing a Ph.D. is not just about completing a research project, it's a journey full of ups and downs, uncertainty, setbacks, and sacrifices. It takes real motivation, resilience, and perseverance to get through it. I'm truly grateful to all the people who helped me make it to the finish line.

First, I want to give my sincere thanks to my supervisor and Ph.D. director, Prof. Tan Pham. He stood by me through every step, even during the slowdowns, the problems, and the tough times. His guidance, encouragement, and trust in me from the very beginning played a huge role in making this thesis possible.

I also want to thank the members of my thesis committee, Prof. Marlene Sanjose and Prof. François Duhaime from École de Technologie Supérieure (ÉTS), Dr. Jacques Lanteigne from Institut de recherche Hydro-Québec, and Dr. Chi-Cong Nguyen from MAYA Heat Transfer technologies Ltd. for agreeing to evaluate my work and for their valuable feedback.

Big thanks to all the researchers, lab staff, and technicians at ÉTS who helped me with the experimental parts of my research. Your support made a real difference. A special thanks to Fonds de Recherche du Québec (FRQ) who supported this project financially and made the journey easier.

To my friends and colleagues, thank you for being there, for cheering me on, and for making this whole journey a lot more bearable.

To my family, especially my amazing and beloved wife, thank you for standing by me through the hard moments, for believing in me, and for celebrating the wins, big or small. And to my lovely mom and brother, your endless support and love were always what kept me going, especially when things got tough.

And last but definitely not least, I want to thank myself for not giving up, for pushing through the hardest days, for staying true to my goals, and for having the courage to ask for help when I needed it. I am proud of how far I have come.

I am dedicating this thesis to my father, who passed away 26 years ago but has always been with me, somewhere, somehow, guiding and supporting me in my endeavors.

ÉTUDE NUMÉRIQUE DES PARAMÈTRES LASER SUR L'INSTABILITÉ DU TROU DE SERRURE LORS DU SOUDAGE LASER

Saeid SAEDIARDAHAEI

RESUME

Le soudage laser en mode « trou de serrure » permet une pénétration profonde dans des métaux comme l'aluminium en formant une cavité induite par la vaporisation du matériau. Cependant, ce procédé est particulièrement sensible aux instabilités du trou de serrure et aux fluctuations du bain fondu, ce qui peut entraîner des défauts tels que la porosité et les projections de métal, compromettant ainsi la qualité du joint soudé. L'observation directe et le contrôle de cette cavité sont difficiles en raison du rayonnement intense et de la dynamique rapide du procédé. La simulation numérique constitue donc une alternative précieuse pour étudier ces phénomènes.

Cette thèse vise à examiner numériquement l'effet des paramètres du soudage laser sur la stabilité du trou de serrure dans l'aluminium. L'objectif est d'identifier les paramètres (puissance laser, diamètre du faisceau, fréquence/durée d'impulsion, forme d'onde, etc.) qui aggravent ou atténuent l'instabilité du trou de serrure, et de proposer des stratégies de modulation (notamment par le façonnage de la courbe de puissance) pour stabiliser le procédé et améliorer la qualité du soudage.

Un modèle multiphysique complet a été développé sous COMSOL Multiphysics, intégrant une théorie du mélange modifiée, une méthode *Level-Set* pour le suivi de la surface libre du bain fondu et de l'interface vapeur/liquide, ainsi qu'une approche enthalpie-porosité pour les changements de phase. Ce modèle a permis d'analyser le soudage laser par onde continue et par impulsions modulées en puissance. Des études paramétriques ont été menées en faisant varier la puissance laser (2–6 kW), le rayon du faisceau, la fréquence et la durée des impulsions, le nombre d'impulsions et la forme d'onde (rectangulaire, triangulaire, sinusoïdale, cosinusoïdale, etc.). En complément, une méthode de plan d'expériences de Taguchi combinée à une analyse relationnelle grise (GRA) a été utilisée pour évaluer plusieurs critères de qualité du soudage et déterminer les combinaisons optimales pour la stabilité et la pénétration.

Les simulations montrent que l'augmentation de l'intensité laser (puissance élevée et impulsions longues) et l'utilisation d'un faisceau plus concentré améliorent significativement la pénétration (jusqu'à environ 80 %), mais au prix d'une intensification des oscillations du trou de serrure si les impulsions sont trop longues ou trop fréquentes. En particulier, des fréquences d'impulsion élevées et un cycle marche/arrêt rapide accentuent les fluctuations du bain fondu et augmentent le risque de fermeture du trou de serrure. L'analyse des forces a révélé que les effets de tension superficielle (liés à la courbure du trou de serrure) et la

résistance dans la zone pâteuse (force d'amortissement de Darcy) dominent l'instabilité en régime d'onde pulsée, affectant négativement l'équilibre avec la pression de recul et induisant des oscillations du trou de serrure. De manière cruciale, une modulation de puissance plus progressive s'est révélée efficace pour stabiliser la cavité: les impulsions rectangulaires ont permis la pénétration la plus profonde (supérieure à celle de l'onde continue à énergie équivalente), tandis que les formes triangulaires ou décroissantes ont généré un trou de serrure plus stable et cylindrique avec moins de fluctuations (au prix d'une légère perte de profondeur). Par ailleurs, l'optimisation des formes d'onde a montré que l'utilisation d'une faible amplitude (~1000 W) et d'une fréquence basse à moyenne (~100–400 Hz), combinées à un profil de puissance cosinusoïdal, améliore nettement la stabilité tout en conservant une bonne pénétration. Parmi tous les paramètres étudiés, l'amplitude des impulsions s'est révélée être le facteur le plus influent sur la qualité du soudage (responsable de plus de 50 % de la variation), suivie de la fréquence et de la forme de l'impulsion.

Cette étude numérique apporte un éclairage nouveau sur l'instabilité du trou de serrure en soudage laser et démontre que la modulation ciblée des paramètres laser permet de renforcer significativement la stabilité du procédé. En sélectionnant des formes d'onde appropriées et des conditions opératoires modérées (en évitant les pics de puissance extrêmes et les fréquences trop élevées), il est possible d'obtenir des soudures profondes et de haute qualité en aluminium, tout en réduisant les risques de défauts. Ces résultats offrent des lignes directrices concrètes pour l'optimisation des paramètres de soudage laser et soulignent la valeur des simulations multiphysiques dans la compréhension des interactions complexes entre le laser et la matière.

Mots-clés: trou de serrure, soudage laser, instabilité, pression de recul, force d'amortissement de Darcy, effet Marangoni, effet de courbure, profondeur de pénétration du trou de serrure, mise en forme des impulsions, comportement des écoulements, interface vapeur/liquide, interface solide/liquide., optimisation, instabilité, analyse relationnelle grise

NUMERICAL STUDY OF LASER PARAMETERS ON THE INSTABILITY OF THE KEYHOLE DURING LASER WELDING

Saeid SAEDIARDAHAEI

ABSTRACT

Keyhole mode laser welding is capable of achieving deep penetration in metals like aluminum by forming a vapor-induced cavity ("keyhole") during welding. However, this process is highly susceptible to keyhole instabilities and fluctuations that can lead to defects (e.g., porosity and spatter), undermining weld quality. Direct observation and control of the keyhole are challenging due to intense optical emissions and rapid dynamics, so numerical simulation offers a valuable alternative to investigate these phenomena.

This thesis aims to numerically examine how laser welding parameters affect keyhole stability in aluminum. The goal is to identify which parameters (laser power, spot size, pulse frequency/duration, waveform shape, etc.) exacerbate or mitigate keyhole instability, and to propose parameter modulation strategies (especially via power waveform shaping) to stabilize the keyhole and improve overall weld quality.

A comprehensive multiphysics simulation model was developed in COMSOL Multiphysics, integrating a modified mixture theory, a level-set method for tracking the vapor/liquid and molten pool free surface, and an enthalpy-porosity approach for phase change. Using this model, both continuous wave and power-modulated pulsed laser spot welding scenarios were analyzed. Parametric studies varied laser power (2–6 kW), beam spot radius, pulse frequency, pulse duration, number of pulses, and pulse shape (rectangular, triangular, sinusoidal, cosinusoidal, etc.). Additionally, a Taguchi design of experiments combined with Grey Relational Analysis was employed to evaluate multiple weld-quality responses and determine optimal parameter combinations for stability and penetration.

The simulations reveal that increasing laser intensity (higher power and longer pulses) and using a smaller beam spot greatly improve penetration (up to ~80% deeper welds) but also intensify keyhole oscillations and instability if pulses are too prolonged or frequent. In particular, higher pulse frequencies and rapid on-off cycling of the laser amplify melt pool fluctuations and increase the tendency for keyhole collapse. Force analysis showed that surface tension effects (due to keyhole curvature) and mushy-zone drag (Darcy damping) dominate the instability during pulse wave modulation, negatively affecting the balance with recoil pressure, leading to keyhole oscillations. Importantly, smoother power modulation proved effective in stabilizing the keyhole: rectangular pulses achieved the deepest penetration (exceeding that of continuous wave under equivalent conditions), whereas triangular and ramp-down pulse shapes produced a more stable, cylindrical keyhole with reduced fluctuations (at the cost of slightly shallower penetration). Furthermore, systematic waveform optimization indicated that low pulse amplitude (~1000 W) and low-to-medium pulse frequencies (≈100–

400 Hz), combined with a cosinusoidal power profile, significantly improve process stability while maintaining adequate penetration. Among the parameters studied, pulse amplitude was found to have the strongest effect on weld quality (contributing over 50% of performance variation), followed by pulse frequency and waveform shape.

This numerical study provides new insights into the instability of the keyhole during laser welding and demonstrates that tailored laser parameter modulation can substantially enhance welding stability. By selecting appropriate power waveforms and moderate operating conditions (avoiding extreme peak powers and overly high frequencies), it is possible to achieve deep, high-quality aluminum welds with minimal defect formation. The findings offer practical guidelines for optimizing laser welding parameters and underscore the value of multiphysics simulations in unraveling complex laser–material interaction dynamics.

Keywords: keyhole, laser welding, instability, recoil pressure, Darcy's damping force, Marangoni effect, curvature effect, keyhole penetration depth, pulse shaping, fluid flow behavior, vapor/liquid interface, solid/liquid interface, optimization, instability, grey relational analysis

TABLE OF CONTENTS

Page

LIST OF TABLES

Page

LIST OF FIGURES

Page

LIST OF ABBREVIATIONS

LS	Level-set
MW	Modulated wave
PW	Pulsed wave
PWM	Pulse wave modulation
CW	Continuous wave
LC	Laser characteristics
LBW	Laser beam welding
HAZ	Heat affected zone
OA	Orthogonal array
ANOVA	Analysis of variance
GRA	Grey relational analysis
GRC	Grey relational coefficient
GRG	Grey relational grade
DOF	Degree of freedom
RSD	Relative standard deviation
SD	Standard deviation
TEPT	Thermal enthalpy porosity technique
MMT	Modified mixture theory

LIST OF SYMBOLS

T_m	Melting temperature; [K]
T_V	Vaporization temperature; [K]
T_s	Solidus temperature; [K]
T	Temperature; [K]
dT_m	Smoothing interval of melting; [K]
dT_V	Smoothing interval of vaporization; [K]
k_s	Thermal conductivity of solid; [W/m/K]
k_l	Thermal conductivity of liquid; [W/m/K]
k_g	Thermal conductivity of gas; [W/m/K]
L_m	Latent heat of fusion; [J/kg]
L_v	Latent heat of evaporation; [J/kg]
R	Universal gas constant; [J/mol/K]
Cp_s	Specific heat of solid; [J/kg/K]
Cp_l	Specific heat of liquid; [J/kg/K]
Cp_g	Specific heat of gas; [J/kg/K]
$Cp_{Al,eff}$	Equivalent specific heat capacity; [J/kg/K]
μ_s	Dynamic viscosity of solid; [Pa.s]
μ_l	Dynamic viscosity of liquid; [Pa.s]
μ_g	Dynamic viscosity of gas; [Pa.s]
d	Form factor for Gaussian distribution
C	Coefficient in Darcy's law
b	Coefficient in Darcy's law
R_{eff}	Effective radius of a laser beam; [m]
d	Dendrite dimension; [m]
M	Molecular mass of aluminum; [kg/mol]
h	Convective heat transfer coefficient; [W/m^2/K]
f	Laser frequency; [Hz]
$\vec{g}$	Gravity; [m/s^2]

p	Pressure; [atm]
$\vec{u}$	Velocity; [m/s]
t	Time; [s]
F_{Darcy}	Darcy damping Force per unit volume; [N/m^3]
$F_{Buoyancy}$	Buoyancy force per unit volume; [N/m^3]
$V_{f,1}$	Volume fraction of fluid 1
$V_{f,2}$	Volume fraction of fluid 2
D_m	Gauss function around the melting temperature
D_V	Gauss function around the vaporization temperature
K	Mushy zone inverse permeability constant used in Darcy damping formula; [1/m^2]
P_{sat}	Saturated vapor pressure; [atm]
P_{atm}	Atmospheric pressure; [atm]
V_L	Volume fraction of liquid
V_s	Volume fraction of solid
$\vec{n}$	Normal vector on the vapor/liquid interface
$\vec{k}$	Tangential vector on the vapor/liquid interface
B_t	Temporal laser distribution function used to apply pulses
$SD_j^{(i)}$	Standard deviation of the j-th response of the i-th test
$RSD_j^{(i)}$	Relative standard deviation of the j-th response of the i-th test
n	Total number of time steps
m	Total number of responses for the optimization technique
$x_j^{(i)}$(t)	Time-dependent value of the j-th response for the i-th test
$\bar{x}_j^{(i)}$	Mean of the time-dependent value of the j-th response over all total time steps

X_{ij}	Original value of the j-th response of the i-th test
$X_{ij}{}^{*}$	Normalized value of the j-th response of the i-th test
X_j	Set of all values of the j-th response over all test experiments
$X_{ij}{}^{*,ideal}$	Ideal normalized response
Δ_{ij}	Deviation of the normalized value for the j-th response of the i-th test
Greek	
γ	Level-set parameter; [m/s]
ε	Level-set parameter; [m]
δ	Delta function
ϕ	Level-set function (variable)
α	Absorptivity of aluminum on 1064 nm laser
ξ	Surface emissivity
ξ	The distinguishing coefficient in optimization approach
β_L	Thermal expansion coefficient; [1/K]
β_R	Retro-diffusion coefficient
ρ	Density; [kg/m^3]
μ	Dynamic viscosity; [Pa.s]
σ	Surface tension coefficient; [N/m]
Subscripts	
L	Liquid
V	Vapor/vaporization
m	Melting
g	Gas
st	Surface tension
r	Radial direction
z	Axial direction

INTRODUCTION

Context of research

In recent years, high-power laser welding has found widespread application across various industrial sectors, including automotive manufacturing, aerospace, pipeline construction, reactor vessels, and the medical device industry (Gao et al., 2018; Katayama et al., 2010). This welding technique has emerged as a highly promising solution due to its capacity to efficiently join thick metal plates, particularly aluminum. Aluminum and its alloys are extensively used owing to their advantageous properties such as high strength-to-weight ratio, excellent thermal and electrical conductivity, strong resistance to oxidation and corrosion, and high reflectivity. As a result, improving the quality of laser welding on aluminum offers substantial benefits for industries ranging from transportation to healthcare (Assuncao & Williams, 2013; Cavilha Neto et al., 2021; Hajavifard et al., 2016).

Laser welding operates in two distinct modes: conduction and keyhole. In the conduction mode, heat is transferred at relatively low power densities, resulting in shallow fusion of the material. In contrast, the keyhole mode employs high power densities (typically exceeding 10^6 W/cm^2), which elevate the material temperature beyond its vaporization point. This induces intense metal evaporation and creates a vapor channel referred to as a keyhole driven by recoil pressure. The formation of the keyhole enables deep weld penetration, often spanning several millimeters to centimeters (Dal & Fabbro, 2016; Steen & Mazumder, 2010).

Laser welding offers several advantages, including high production speeds, reduced energy consumption, narrower heat-affected zones, and minimized weld bead widths (Svenungsson et al., 2015). Nevertheless, controlling process-induced defects remains critical due to the potential environmental, economic, and safety consequences of faulty welds (Courtois et al., 2013; Steen & Mazumder, 2010). Common welding defects include humping (Bunaziv et al., 2020), porosity (Tan & Shin, 2014), spatter (Wu et al., 2017), and other structural imperfections, all of which significantly compromise the integrity and reliability of welded

components. Among these, porosity commonly caused by keyhole instability is particularly problematic in aluminum welding. These defects are frequently linked to dynamic fluctuations of the keyhole, melt pool oscillations, and keyhole collapse, underscoring the need for advanced numerical and experimental strategies to enhance weld stability and ensure high-quality, defect-free joints (Guo et al., 2018; Lin et al., 2017).

Research problem

Experimental investigations of laser welding processes, particularly in keyhole mode, are often prohibitively complex and costly. Moreover, direct observation of the keyhole dynamics during welding is extremely challenging due to the intense brightness of the plasma and process radiation. Given the critical role of laser welding across numerous manufacturing sectors, there is a growing need to develop robust and accurate numerical models capable of optimizing laser parameters to ensure stable keyhole formation and minimize welding defects. Aluminum, despite its many advantageous properties, poses significant challenges in both experimental and numerical studies. Its high reflectivity and thermal conductivity often lead to numerical convergence issues, making accurate simulation more difficult. Furthermore, the current body of research on keyhole mode laser welding of aluminum remains limited, especially in terms of capturing the detailed physical phenomena and identifying the influence of key laser parameters on defect formation. This lack of comprehensive understanding contributes to frequent defects such as porosity, keyhole collapse, and melt pool instability that compromise the structural integrity and reliability of welded components in critical industries (Bunaziv et al., n.d.).

To address this gap, the present study aimed to develop a high-fidelity numerical simulation framework specifically tailored for laser welding of aluminum. This model will serve as a predictive tool to analyze keyhole stability and to optimize laser process parameters, with the ultimate goal of achieving defect-free welds and advancing the quality and performance of aluminum weld joints.

Objectives and research steps

Enhancing the quality of laser welding particularly in keyhole mode when applied to aluminum offers substantial benefits across multiple sectors, including medical device manufacturing, healthcare technology, mechanical engineering, automotive production, and aerospace applications. This research project sought to contribute to these industries by developing an advanced numerical framework that aligns with experimental observations. The primary objectives of the study were as follows:

- To develop a high-fidelity numerical simulation that accurately captures all relevant physical phenomena and phase interactions in good agreement with experimental results.
- To identify and analyze the critical laser parameters influencing keyhole instability, with the aim of minimizing instabilities.
- To develop an optimization technique for the simulation framework to ensure having a reliable predictive tool, enabling the possibility to choose the best sets of parameters for high-quality welding, minimizing instabilities and defect formation probability.

Approach and methodology

The numerical modeling of keyhole mode laser welding involves simulating a set of highly coupled multiphysics phenomena, including heat transfer, fluid flow, and phase transformations such as melting, evaporation, and solidification. Additionally, laser–material interaction effects such as optical absorption and multiple internal reflections within the keyhole might play a role in weld quality but are challenging to model accurately.

Given the complexity of the keyhole welding process and the wide range of uncertain parameters contributing to instability, the initial phase of this research focused on developing a novel and robust two-dimensional axisymmetric model to simulate stationary laser spot welding on aluminum. This model, designed in COMSOL Multiphysics, was validated against experimental results from both the literature and also with our own experimental setup to

ensure both physical accuracy and computational efficiency. The methodology and findings from this phase are presented in Chapter 2 and were published in *Thermo* journal. The model enabled analysis of various laser process parameters such as power, spot radius, and frequency under both continuous and modulated power conditions. All relevant phases (solid, liquid, and vapor) were considered in the simulation, with appropriate simplifications to maintain numerical stability and reduce computational cost.

Building upon this foundation, the next phase focused on a deeper analysis of pulse modulation strategies with the goal of identifying the physical forces responsible for keyhole instability. Special attention was given to forces and conditions contributing to keyhole instability, such as surface tension, Darcy damping, hydrodynamic effects, and fluid flow behavior. This step, detailed in Chapter 3 and published in *Materials* journal, evaluated how different pulse shapes and temporal power distributions influence keyhole dynamics and process stability. In addition, it identified the reasons behind keyhole instability, responsible forces, and ways to minimize their impact to stabilize keyhole and laser welding process.

In the final phase of the project, following successful model development and validation, a multi-response optimization framework was introduced using a Taguchi-based statistical approach. This method was employed to predict welding performance and determine optimal combinations of laser parameters under specific system configurations. To support this analysis, an experimental setup was developed, and the results were used to further confirm the predictive capabilities of the numerical model. These findings are presented in Chapter 4 and were submitted to *Materials* journal for publication. In addition, a novel laser power profile (cosinusoidal) was also added to the existing methods to improve welding quality.

Organization of thesis

This thesis is organized in four main chapters. Following this introduction, Chapter 1: theoretical background of Laser welding is reviewed.

Chapter 2 includes the first published paper in Thermo journal entitled " Comparative Numerical Analysis of Keyhole Shape and Penetration Depth in Laser Spot Welding of Aluminum with Power Wave Modulation" which was extracted from the outcomes of this thesis project. This chapter focuses on the first part of the project, which propose the methodology introduced in this project to simulate the spot laser welding of aluminum. In addition, it comparatively analyzes the impact of various laser parameters and pulse shapes on the keyhole penetration depth.

In Chapter 3, the paper entitled " Toward stabilizing the keyhole in laser spot welding of aluminum: Numerical analysis", published in *Materials* journal, is presented. This paper focuses on the next part of the project, which studies the underlying mechanisms, forces and reasons behind the instability of the keyhole using quantitative force analysis and proposes alternatives of pulse distribution manipulation, to minimize the keyhole instability and improve the process stability and keyhole penetration depths.

Chapter 4 includes the last paper entitled " Multi-Response Optimization of Aluminum Laser Spot Welding with Sinusoidal and Cosinusoidal Power Profiles Based on Taguchi-Grey Relational Analysis" submitted to *material* journal. This paper presents the last step of this project which aims at investigating the effect of sinusoidal and cosinusoidal pulse shapes on the keyhole instability and depth with experimental validation. It also introduces a novel multi-response Taguchi-based Grey relational analysis to offer a predicting platform and statistical approach facilitating the identification of desirable welding parameter combinations in favor of welding performance.

In the conclusion chapter, the conclusions of the whole project are presented. This chapter highlights the research discoveries and limitations and provide suggestions for future works.

CHAPTER 1

THEORITICAL BACKGROUND OF LASER WELDING

Laser welding is widely used in industries such as automotive, aerospace, energy, and medical manufacturing due to its ability to produce precise, deep, and high-quality welds at high speeds. Compared to traditional fusion-based methods, it offers distinct advantages including narrow heat-affected zones, minimal distortion, and compatibility with automated systems, making it well-suited for modern, high-efficiency production involving advanced materials and complex geometries.

Despite its numerous advantages, laser welding, particularly in keyhole mode, presents several technical challenges. The process involves intense energy concentration and rapid thermal cycles, resulting in complex interactions between heat transfer, fluid dynamics, and phase transformations. These interactions can lead to various defects such as porosity, spatter, humping, and keyhole collapse, which compromise weld integrity. The instability of the keyhole itself, driven by a balance of forces including recoil pressure, surface tension, Darcy damping force, hydrostatic/hydrodynamic pressures, buoyancy, and gravity is a major source of defect formation. This is especially critical when welding materials like aluminum, which exhibit high reflectivity and thermal conductivity, further complicating process control and simulation accuracy. Addressing these challenges requires a deep understanding of the underlying physical phenomena and the development of predictive numerical models to optimize process parameters and ensure weld quality.

This chapter presents a brief theoretical overview of laser welding and its challenges. Detailed modeling approaches and findings are discussed in Chapters 2 to 4.

1.1 Introduction

Welding is a fabrication process that joins materials, typically metals or thermoplastics, by applying heat, pressure, or a combination of both. The joint is formed as the materials cool and

solidify. While some materials are easily weldable, others require specialized techniques, and certain alloys are considered difficult or unsuitable for conventional welding.

Welding techniques are generally classified into fusion welding and solid-state welding. In fusion welding, materials are melted to form the joint, while in solid-state welding, bonding occurs without melting, typically through pressure and plastic deformation.

A variety of welding methods are employed across industries depending on the material type and application. These include fusion-based processes such as arc welding, laser beam welding, and electron beam welding, as well as solid-state techniques like friction welding and ultrasonic welding (Bunaziv et al., n.d.; Khedr et al., 2022).

1.2 Fundamentals of laser welding

Laser beam welding (LBW) is a high-precision technique that employs a focused laser beam as a heat source to join metal components. The resulting welds are typically narrow and deep, with exceptionally high welding speeds, making LBW especially suitable for industrial applications such as automotive manufacturing. LBW can be performed in two primary modes: conduction mode and keyhole (deep-penetration) mode, the latter being essential for welding thicker sections of material (Hong & Shin, 2017).

This process relies on extremely high power densities, typically around 1 MW/cm², which result in rapid heating and cooling cycles, as well as well-defined heat-affected zones. The laser spot size varies between 0.2 mm and 13 mm, although smaller spot sizes are generally preferred for welding applications. The penetration depth is primarily governed by power density and the focal point location; for optimal results, the focal point is usually positioned just below the surface of the workpiece (Hong & Shin, 2017; Steen & Mazumder, 2010; Svenungsson et al., 2015).

LBW can operate in either continuous or pulsed modes, depending on the specific application, and is capable of welding a wide range of metals including carbon steel, stainless steel, titanium, and aluminum. The process is highly valued for its weld quality, precision, and efficiency. Welding speed increases with both power density and material thickness (Steen & Mazumder, 2010). A schematic overview of the laser welding setup and its components is presented in Figure 1.1 (Kumar & Sinha, 2018).

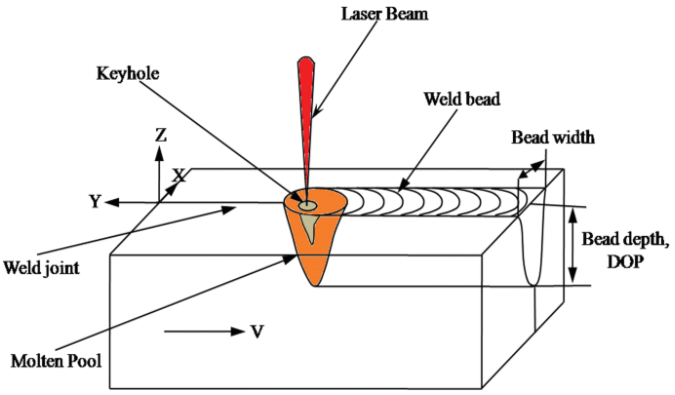

(a)

(b)

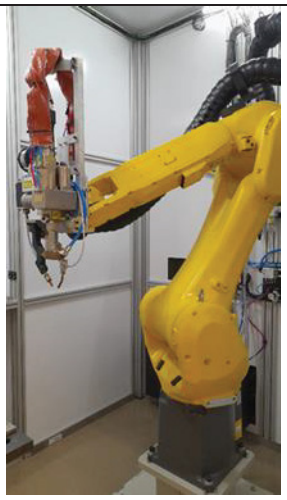

(c)

Figure 1.1 Schematic of laser welding with (a) different welding definitions and components, (b), and (c) experimental setup of laser welding source and laser head
(a) Taken from Kumar et al. (2018, p. 5)

Given the characteristics of laser welding, it offers several advantages over conventional welding methods (Bunaziv et al., 2020; Hong & Shin, 2017; Nabavi et al., 2023; Svenungsson et al., 2015) such as:

- Minimized heat-affected zone (HAZ): The highly focused laser beam reduces the volume of material exposed to heat, which helps preserve the mechanical properties of the base material. Since excessive thermal exposure can degrade material strength and performance, LBW is well-suited for applications requiring minimal metallurgical alteration.
- Low thermal distortion: A smaller HAZ also results in reduced residual stresses and distortion in the welded components, which is particularly beneficial for precision assemblies.
- No vacuum requirement: Unlike electron beam welding, which requires a vacuum environment, laser welding can be performed in ambient air. This enhances its practicality and cost-effectiveness for high-volume production settings, such as the automotive industry.
- High precision and speed: Laser welding supports fast processing rates and excellent control over weld geometry, making it ideal for automated and large-scale manufacturing applications.
- Deep penetration and narrow welds: The ability to achieve full-penetration welds with narrow beads allows LBW to efficiently join thick materials without excessive filler or multi-pass operations.

1.2.1 Keyhole and conduction modes

Laser welding typically operates in one of two regimes: conduction mode and keyhole mode. The primary distinction between these modes lies in the power density, defined as the laser power per unit area. In conduction mode, the power density is relatively low, resulting in surface melting and shallow penetration. This mode is suitable for thin materials and applications requiring minimal thermal impact. In contrast, keyhole mode employs significantly higher power densities, causing the material to vaporize and form a cavity known

as keyhole that allows for deep penetration, making it ideal for thicker components (SaediArdahaei & Pham, 2024a; Steen & Mazumder, 2010). These two regimes are schematically illustrated in Figure 1.2 (Assuncao et al., 2012).

1.2.1.1 Conduction mode

Conduction mode laser welding operates at relatively low power densities, typically below 1 MW/cm². At this level, the energy input is insufficient to induce boiling at standard welding speeds, and as a result, no keyhole formation occurs (Steen & Mazumder, 2010). Instead, the laser beam melts the surface of the material, and heat is transferred inward primarily through thermal conduction, leading to melting of the subsurface region without significant vaporization (Assuncao & Williams, 2014). The effective range of power density for conduction mode varies depending on the thermophysical properties of the material being welded.

The process begins when the laser beam irradiates the surface of the workpiece, generating heat that diffuses into the material. This results in a shallow, wide molten pool, characteristic of conduction mode welding, as illustrated in Figure 1.2 (a).

1.2.1.2 Keyhole mode

The focused laser beam is among the most powerful energy sources available for welding, capable of delivering power densities comparable to those of an electron beam. At such high intensities, typically exceeding 1 MW/cm², material evaporation becomes inevitable for any absorbent surface. In this regime, known as keyhole mode or penetration mode, the energy delivered to the workpiece surface is sufficient to induce rapid melting, vaporization, and even ionization, forming a plasma (Steen & Mazumder, 2010; Svenungsson et al., 2015).

The process begins almost instantaneously, with metal vaporization occurring within 10^{-6} to 10^{-8} seconds of laser exposure. The vapor exerts a recoil pressure on the surrounding molten

metal, displacing it and forming a gas-filled cavity, or keyhole, which extends vertically into the material. The cavity remains open and stable due to the continuous expansion of vapor pressure within it. As the laser beam moves across the workpiece, the keyhole also progresses forward, transferring heat to the adjacent material through its walls (Bunaziv et al., n.d.; Steen & Mazumder, 2010). This results in a narrow, deep molten pool that solidifies behind the keyhole, producing a characteristic deep-penetration weld as shown in Figure 1.2 (b).

The keyhole also acts as an optical blackbody, trapping the incoming laser radiation through multiple internal reflections. This significantly enhances energy absorption efficiency, ensuring that a large portion of the laser energy is effectively used for melting and vaporization. This mechanism is depicted in Figure 1.3 (Liu et al., 2020).

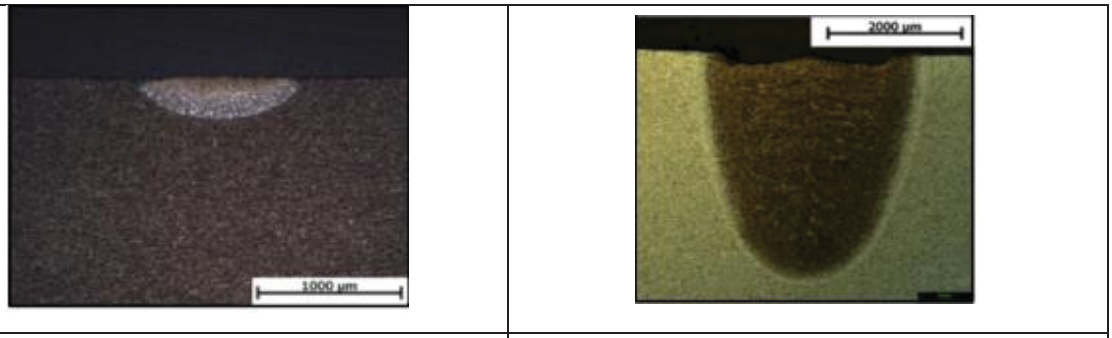

Figure 1.2 Two Laser welding regimes for (a) Conduction mode without evaporation, and (b) keyhole mode with evaporation
Taken from Assuncao et al. (2012, p. 823)

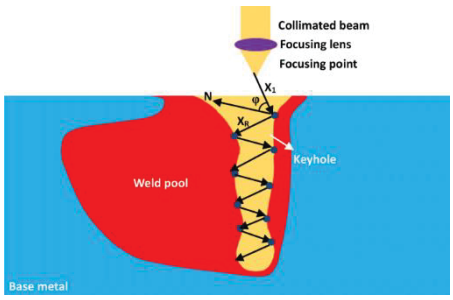

Figure 1.3 multiple reflections of laser beam within the keyhole
Taken from Peng Liu et al. (2020, p. 737)

1.3 Physical Phenomena in keyhole mode laser welding

Keyhole mode laser welding involves numerous coupled physical phenomena, including laser–material interaction, heat transfer, fluid flow, phase transformation, solid mechanics, and metallurgical behavior. Each of these contributes to the overall dynamics and quality of the welding process. However, the present thesis focuses specifically on a subset of these phenomena outlined by the dashed red line in Figure 1.4 which includes the interaction between heat transfer, fluid flow, and keyhole dynamics within the molten region.

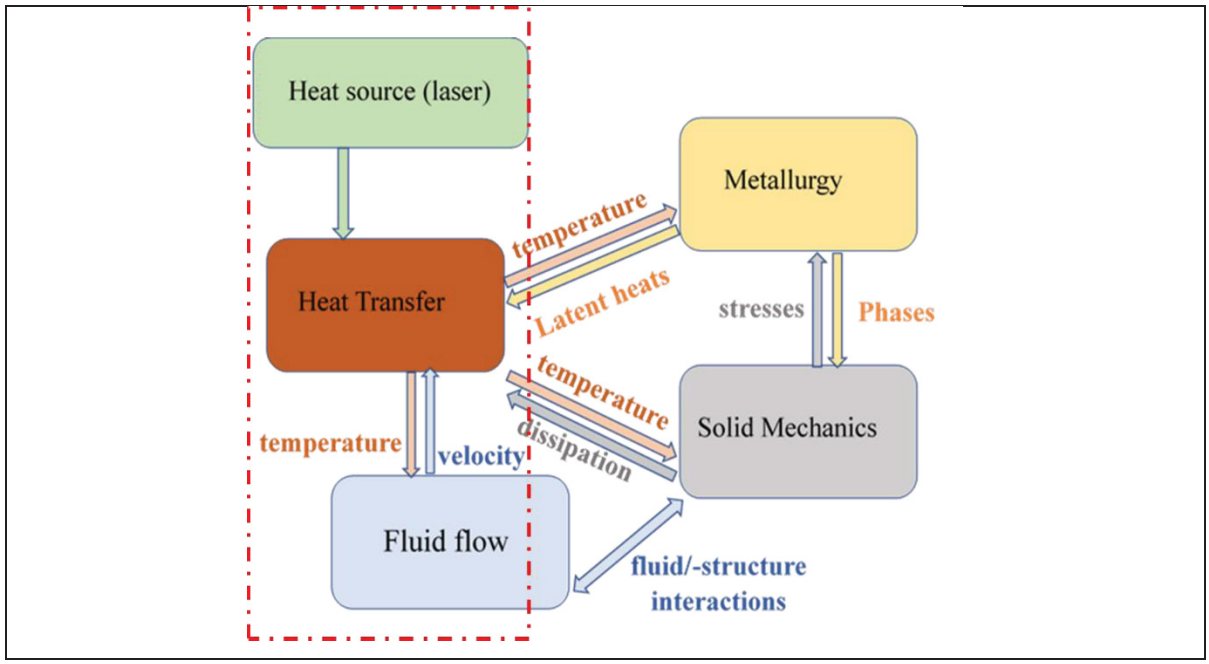

Figure 1.4 Available physics during keyhole mode laser welding

1.3.1 Available Phases in keyhole mode laser welding

During keyhole mode laser welding, three primary phases such as solid, liquid, and vapor are involved, along with their corresponding phase transformations: melting, vaporization, and solidification. In addition to these, plasma may also form as a fourth transient phase. This plasma originates either from the vaporized metal (metallic plasma) or from the interaction between the metal vapor and the shielding gas (shroud gas plasma) (SaediArdahaei & Pham,

2024a; Steen & Mazumder, 2010). However, due to the significant complexity it adds to numerical modeling, plasma effects are neglected in this thesis.

These phases along with their transformations are illustrated in Figure 1.5, where the material undergoes rapid melting as the laser irradiates the surface, transitioning from solid to liquid. When the local temperature exceeds the boiling point, the liquid metal is further transformed into vapor, contributing to the formation of recoil pressure and keyhole development. As the laser beam moves along the weld line, or when the laser heat source turns off in pulsed wave modulation scenarios or after the welding finishes, regions that are no longer exposed to the heat source undergo solidification, completing the thermal cycle.

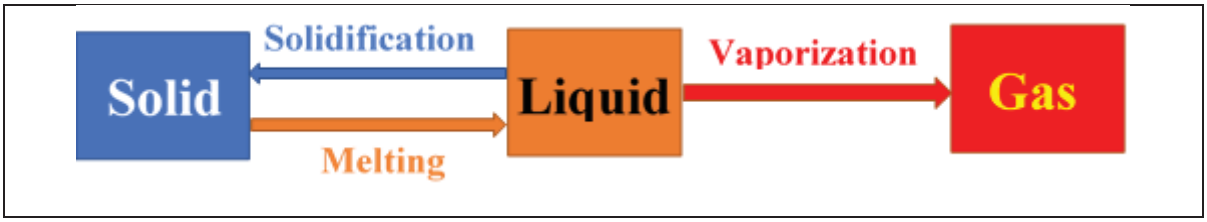

Figure 1.5 Available phases and phase transformations considered in the process

1.3.2 Heat transfer mechanisms within the laser welding process

Heat transfer in laser welding occurs through three fundamental mechanisms: radiation, convection, and conduction.

1.3.2.1 Conduction

Conduction refers to the transfer of heat from regions of higher temperature to regions of lower temperature within a material or between materials in contact, without any macroscopic movement of the material itself. In metals, this process is primarily facilitated by free electrons and atomic lattice vibrations (Özişik, 1993).

In conduction mode laser welding, heat transfer is predominantly governed by conduction due to the absence of significant fluid motion in the weld pool. When the laser beam irradiates the

surface of the workpiece, it induces a localized temperature rise. This thermal energy is then conducted into the material along three-dimensional spatial directions, resulting in the formation of a shallow, hemispherical molten pool (Steen & Mazumder, 2010).

1.3.2.2 Convection

Convection refers to heat transfer facilitated by the macroscopic movement of fluid, which carries thermal energy from one region to another. This mechanism can occur either naturally driven by buoyancy forces resulting from temperature-induced density differences or be forced, in which case an external source initiates fluid motion.

In the context of laser welding, convection within the molten pool arises primarily from temperature gradients in the material. These gradients generate fluid motion due to variations in surface tension (Marangoni/curvature effects) and density (natural convection), leading to enhanced heat distribution across the weld zone (He et al., 2005).

1.3.2.3 Radiation

Radiation is a mode of heat transfer in which thermal energy is emitted from the surface of a body in the form of electromagnetic waves, typically infrared radiation. This mechanism does not require any physical medium or contact, unlike conduction and convection. Any object with a temperature above absolute zero (0 K) continuously radiates energy outward, and the intensity of this radiation increases with temperature. In the context of laser welding, as the weld pool temperature rises, it emits thermal radiation to the surrounding environment, contributing to overall heat loss during the process (Courtois et al., 2014).

1.3.3 Fluid flow with keyhole mode laser welding

The flow behavior within the molten pool and around the keyhole is governed by multiple interacting forces. The dominant driving mechanisms include recoil pressure, Marangoni

(shear surface tension) force, buoyancy, Darcy damping, and the curvature effect of surface tension. Recoil pressure acts on the keyhole walls and drives material outward, promoting cavity formation. Marangoni flow, driven by surface tension gradients along the free surface, governs lateral fluid motion. Buoyancy arises from temperature-dependent density variations. Darcy damping resists melt motion in the mushy zone, contributing significantly to the collapse or closure of unstable keyholes. Additionally, the curvature effect imposes a normal surface tension force dependent on the local geometry of the melt surface, influencing both cavity shape and dynamic stability. These forces are tightly coupled, resulting in complex, non-linear flow patterns and contributing to fluctuations and instabilities within the keyhole and molten pool (Courtois et al., 2013; Qin et al., 2011; SaediArdahaei & Pham, 2024a, 2024b). These forces along with solid/liquid, vapor/liquid interfaces are shown in Figure 1.6 (SaediArdahaei & Pham, 2024a).

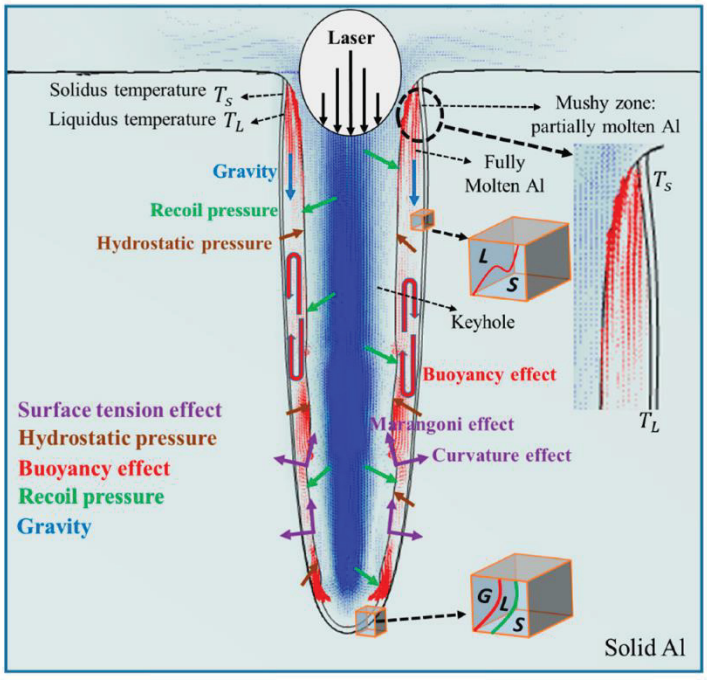

Figure 1.6 Schematic depiction of the keyhole and molten pool with various driving forces and characteristics

Taken from Ardahaei et al. (2024, p. 237)

1.3.3.1 Buoyancy force

Buoyancy force arises from temperature-induced density gradients within the molten pool, resulting in longitudinal fluid motion. During laser welding, the temperature distribution decreases from the central region, directly irradiated by the laser, to the edges of the molten pool near the melting temperature. In contrast, the density follows the opposite trend: cooler molten metal at the periphery becomes denser and sinks, while the hotter, lighter fluid near the center rises upward, establishing a natural convection loop within the weld pool (Amara & Fabbro, 2008).

1.3.3.2 Recoil pressure

In keyhole mode laser welding, the intense evaporation of molten metal generates recoil pressure, which plays a central role in keyhole formation and evolution. This pressure displaces the surrounding liquid metal outward as the keyhole deepens. Simultaneously, the Marangoni effect and hydrodynamic pressure assist in circulating the displaced metal upward, while hydrostatic pressure, increasing with keyhole depth, resists this upward flow (Courtois et al., 2012).

Recoil pressure also drives strong fluid motion near the keyhole front and along the keyhole wall, pushing molten metal backward and feeding the bulk flow within the weld pool. Prior studies have confirmed that in full-penetration welds, recoil pressure is one of the forces influencing melt dynamics and weld pool stability (Zhou et al., 2006).

1.3.3.3 Surface tension

In laser welding, surface tension at the melt pool interface significantly influences fluid flow behavior and contributes to keyhole instability, primarily by acting to close the cavity. Its effect on the melt flow arises from two distinct components. The first is the curvature effect, where surface tension generates a normal force proportional to the local curvature of the free surface.

The second is the Marangoni effect, a tangential force along the free surface driven by temperature-dependent surface tension gradients. Both components are critical in determining the flow structure and stability within the molten pool (Brackbill et al., 1992; Saadlaoui et al., 2018).

1.3.3.4 Darcy Damping force

Darcy's damping force accounts for the frictional resistance to fluid flow in the mushy zone the region where the material transitions from liquid to solid during cooling. This resistance is modeled using the Carman-Kozeny relationship, derived from Darcy's law for porous media, and is implemented as a volumetric source term in the Navier-Stokes equations. The damping effect becomes particularly significant in regions where solidification is dominant, acting to suppress fluid motion by forcing the velocity to approach zero in solid regions (Herbinger et al., 2016; H. Wang et al., 2007).

To control the strength of this damping, a material-dependent parameter is introduced based on the local liquid fraction. A constant, typically ranging from 10^4 to 10^8, is selected based on prior experimental studies or through sensitivity analyses to ensure numerical stability. Additionally, a small correction factor is used to avoid division by zero. In simulations using COMSOL, this force is crucial for accurately representing buoyancy-driven flow within the mushy zone, and it strongly influences the fluid dynamics and keyhole stability, especially during solidification multi-pulse wave laser welding (Herbinger et al., 2016; H. Wang et al., 2007).

1.4 Keyhole instabilities and collapse

The stability of the keyhole is a critical factor in the success of keyhole mode laser welding. In fact, the feasibility of maintaining this welding regime depends largely on the ability to sustain a stable keyhole throughout the process. As previously discussed, fluid flow in this regime is highly complex, and the keyhole wall undergoes dynamic and irregular fluctuations.

During keyhole mode laser welding, various driving forces and pressures act simultaneously, directly influencing the shape and behavior of the keyhole and the surrounding molten pool. These forces can either work to open or close the keyhole, and their interactions determine its stability.

A stable keyhole exists when these competing forces are in dynamic equilibrium. However, fluctuations in any of the dominant forces, particularly under high-energy and time-dependent conditions, can disturb this balance and lead to keyhole collapse, often accompanied by defect formation such as porosity or incomplete fusion. Among all the forces, recoil pressure plays a dominant role in keeping the keyhole open. Therefore, any factor, force or pressure that reduces or destabilizes the recoil pressure such as a drop in laser intensity, improper pulsing, or inaccurate sets of laser parameters can lead to instability and collapse of the keyhole, lowering the weld quality and increasing the probability of defect formation (SaediArdahaei & Pham, 2024b; Svenungsson et al., 2015).

Although theoretical models can predict the required balance of forces for keyhole stability, the phenomenon remains extremely complex in practice. The keyhole wall exhibits severe oscillations due to rapid fluctuations in local pressures and forces. Consequently, keyhole instabilities and collapse are commonly observed in experiments, highlighting the importance of their investigation in simulations to better anticipate defect formation and optimize process parameters.

Keyhole shape undergoes rapid temporal and spatial fluctuations, including regular pulsing and lateral flapping which can be seen in Figure 1.7 (Matsunawa, 2002; Yu & Zhao, 2023).

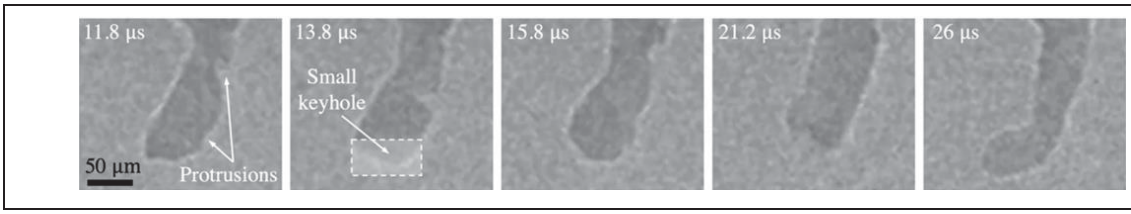

Figure 1.7 Temporal and erratic keyhole wall behavior
Taken from Tao et al. (2023, p. 5)

1.5 Material Aspects: Welding of Aluminum

Welding aluminum presents significant challenges due to its intrinsic thermophysical properties. Its high reflectivity at common laser wavelengths reduces energy absorption, necessitating higher power densities for effective melting. Additionally, high thermal conductivity causes rapid heat dissipation, making it difficult to maintain a stable melt pool and increasing the risk of incomplete fusion or solidification-related defects. Moreover, the process window is relatively narrow, with limited tolerance for joint gap misalignment, and the material is highly prone to defects such as porosity, hot cracking, and keyhole instability especially in keyhole mode laser welding. These difficulties are further exacerbated by the presence of a stable aluminum oxide layer with a much higher melting point than the base metal, and by the material's high hydrogen solubility, which promotes gas entrapment during solidification.

Despite these challenges, high-quality aluminum welds are crucial in industries such as automotive, aerospace, energy systems, and electronics, where the demand for lightweight yet strong structures continues to grow. The ability to perform reliable laser welding on aluminum allows for faster production, reduced material distortion, and enhanced mechanical performance, making it essential for modern high-performance manufacturing systems (Bunaziv et al., n.d., 2024; Okon, n.d.).

1.6 Some typical defects in keyhole mode laser welding

Laser welding is associated with several common defects in the final welded specimen, including humping, porosity, spatter, cracking, and undercuts. While many of these imperfections can be mitigated through careful adjustment of process parameters, such as laser power, speed, and focus, the complex and multiphysics nature of the laser welding process poses significant challenges. Effective defect suppression requires not only optimal parameter selection, but also a comprehensive understanding of the underlying physical phenomena, including thermal gradients, fluid flow, phase transitions, and force interactions within the molten pool.

1.6.1 Porosity

Porosity refers to the formation of gas-filled cavities or voids within the weld metal due to the entrapment of gas or non-metallic inclusions during solidification, as illustrated in Figure 1.8 (Tan & Shin, 2014). Prior studies have identified keyhole geometry and solidification time as the two dominant factors influencing porosity formation in laser welding processes. In keyhole mode laser welding, porosity is primarily caused by keyhole instability and collapse, which can lead to the entrapment of vapor within the rapidly solidifying molten pool. This defect can be mitigated through pulse modulation strategies that enhance keyhole stability particularly by reducing pulse width and avoiding sudden collapse events (Lin et al., 2017; Tan & Shin, 2014).

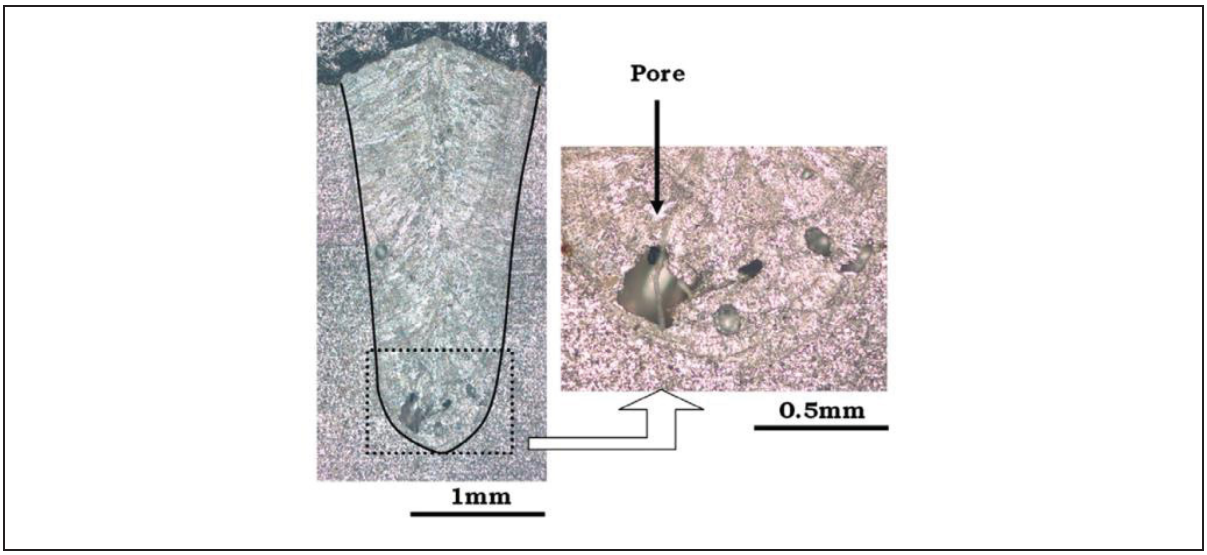

Figure 1.8 Porosity formation during keyhole mode laser welding
Taken from Tan et al. (2014, p. 12)

1.6.2 Spatters and undercuts

Spatter refers to the ejection of molten metal droplets from the weld pool, which subsequently adhere to the surrounding surface, often degrading the weld quality and appearance. This phenomenon typically results from keyhole instability, excessive recoil pressure, or rapid

fluctuations in melt flow dynamics. The spatter formation mechanism is illustrated in Figure 1.9 (a) (Young et al., 2020).

An undercut is defined as an unfilled groove or depression along the edge of the weld bead, as shown in Figure 1.9 (b). This defect can compromise the mechanical integrity of the joint by acting as a stress concentrator. Undercuts typically result from inappropriate laser parameters, such as excessive power, high welding speeds, poor pulse control, or keyhole instability, which lead to incomplete filler distribution or melt ejection from the weld edge (Xu et al., 2021).

1.6.3 Cracking

Crack formation in keyhole mode laser welding is typically attributed to high thermal gradients and rapid solidification rates, which induce tensile stresses in the mushy zone during cooling. This phenomenon, commonly referred to as solidification cracking as shown in Figure 1.10, can significantly degrade the mechanical properties and structural integrity of the weld, potentially leading to premature failure of the final product.

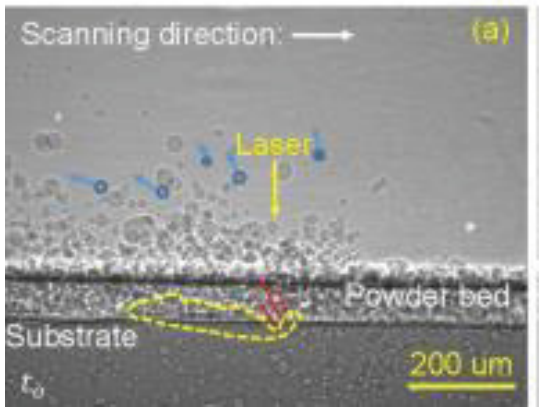

(a)

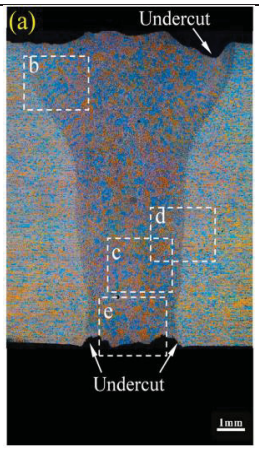

(b)

Figure 1.9 (a) formation of Solid spatters (blue circles) in laser welding, (b) formation of undercuts
(a) Taken from Zachary et al. (2020, p. 2)
(b) Taken from Xu et al. (2021, p. 9)

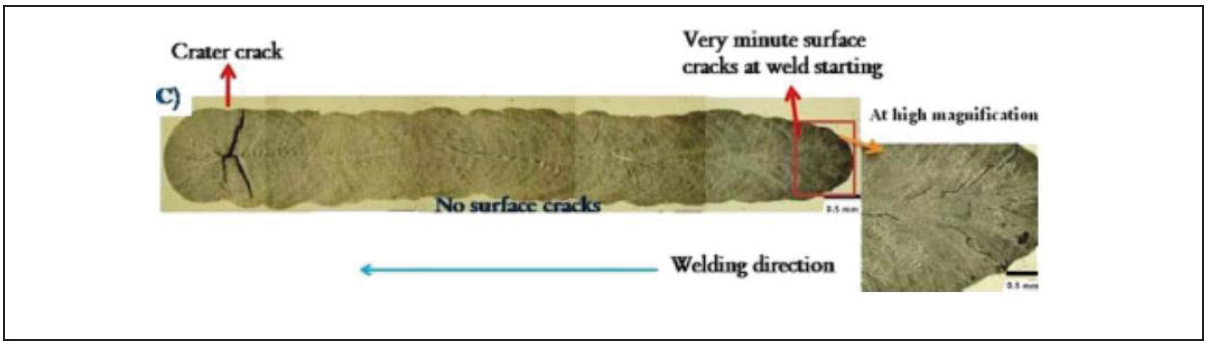

Figure 1.10 Cracking during Keyhole mode laser welding
Taken from Chelladurai et al. (2015, p. 581)

1.7 Numerical modeling of laser welding

Numerical simulation plays a vital role in understanding and optimizing laser welding processes by providing detailed insights into complex multiphysics phenomena such as heat transfer, fluid flow, phase change, and keyhole dynamics. Compared to experimental investigations which are often costly, time-consuming, and limited by the inability to observe internal phenomena due to intense process radiation, simulations offer a controlled and flexible environment for exploring a wide range of parameters and conditions (Courtois et al., 2014; Ribic et al., 2009). Various numerical techniques have been employed for laser welding modeling, including the Finite Element Method (FEM) for thermal analysis, Volume of Fluid (VOF) and Level Set (LS) methods for tracking free surfaces and keyhole evolution. These tools enable high-fidelity modeling of keyhole behavior, weld pool dynamics, and defect formation mechanisms, making simulation an indispensable complement to experimental research (Ki et al., 2002; Zhao et al., 2011).

1.8 Pulse shaping and process control

Pulse shaping is an effective strategy in laser welding used to control energy delivery and improve keyhole stability. By modulating the temporal profile of laser power, it becomes possible to reduce defects such as porosity and keyhole collapse, particularly in pulsed or spot welding processes. These tailored power inputs influence recoil pressure, melt flow, and solidification behavior, thereby enhancing weld quality and consistency.

Pulse shaping has emerged as an effective strategy in laser welding to improve thermal control, keyhole stability, and defect suppression. By modulating the temporal profile of laser power through shapes such as ramp-down, step-down, triangular, or preheating-cooling sequences researchers have shown significant improvements in weld quality, particularly for challenging materials like aluminum and Al-Cu joints. For instance, ramp-down and step-down pulse shapes were demonstrated to reduce solidification cracking in 5083 aluminum by controlling the cooling rate and decreasing the vulnerable zone at the end of solidification (Jia et al., 2021).

In dissimilar metal welding (e.g., Al-Cu), tailored pulse shapes enhanced absorption efficiency and limited the formation of brittle intermetallic compounds (IMCs), thus improving mechanical strength and electrical conductivity of the joints (Ma et al., 2024; Mathivanan & Plapper, 2019). Additionally, Hajavifard et al. showed that optimized pulse shaping especially ramp-down combined with initial coupling, can achieve deeper penetration with fewer defects even under low-power welding setups (Hajavifard et al., 2016).

In summary, this chapter provided a theoretical foundation for understanding the laser welding process, with a focus on keyhole mode welding of aluminum. The fundamental principles of heat transfer, fluid flow, and phase transformations were reviewed alongside the key forces affecting weld pool behavior, including recoil pressure, surface tension (curvature and Marangoni effects), buoyancy, and Darcy damping. Common welding defects such as porosity, cracking, and spatter were discussed in relation to these underlying mechanisms. Special emphasis was placed on the challenges of welding aluminum, due to its high reflectivity, thermal conductivity, and narrow process window. Numerical modeling was introduced as a critical tool for investigating such complex, multiphysics phenomena, and pulse shaping was highlighted as a promising strategy for improving keyhole stability and weld quality. The following chapters will present detailed numerical investigations into novel pulse modulation strategies, keyhole instability analysis, and the development of stability enhancement techniques, supported by validated simulation results and parametric studies.

CHAPTER 2

COMPARATIVE NUMERICAL ANALYSIS OF KEYHOLE SHAPE AND PENETRATION DEPTH IN LASER SPOT WELDING OF ALUMINUM WITH POWER WAVE MODULATION

Saeid SaediArdahaei and Xuan-Tan Pham [a]

[a] Department of Mechanical Engineering, École de Technologie Supérieure, 1100, Notre-Dame West, Montreal, Quebec, Canada H3C 1K3

Paper published in *Thermo*[1], May 2024

Abstract

Keyhole mode laser welding is a valuable technique for welding thick materials in industrial applications. However, its susceptibility to fluctuations and instabilities poses challenges, leading to defects that compromise weld quality. Observing the keyhole during laser welding is challenging due to bright process radiation, and existing observation methods are complex and expensive. This paper alternatively presents a novel numerical modeling approach for laser spot welding of aluminum through a modified mixture theory, a modified level-set (LS) method, and a thermal enthalpy porosity technique. The effects of laser parameters on keyhole penetration depth are investigated, with a focus on laser power, spot radius, frequency, and pulse wave modulation in pulsed wave (PW) versus continuous wave (CW) laser welding. PW laser welding involves the careful modulation of power waves, specifically adjusting the pulse width, pulse number, and pulse shapes. Results indicate a greater than 80 percent increase in the keyhole penetration depth with higher laser power, pulse width, and pulse number, as well as decreased spot radius. Keyhole instabilities are also more pronounced with higher pulse width/numbers and frequencies. Notably, the rectangular pulse shape demonstrates substantially deeper penetration compared to CW welding and other pulse shapes. This study enhances understanding of weld pool dynamics and provides insights into optimizing laser welding parameters to mitigate defects and improve weld quality.

[1] Thermo 2024, 4(2), 222-251

Keywords: keyhole; instability; recoil pressure; vapor/liquid interface; solid/liquid interface; keyhole penetration depth

2.1 Introduction

In recent years, high-power laser welding has been extensively utilized in diverse industrial sectors, such as automotive manufacturing, astronautics and aeronautics, pipelines, and reactor vessel (Gao et al., 2018; Katayama et al., 2010), to name a few. High-power laser welding is a promising candidate for industrial use due to its potential to efficiently join thick plates of various metals, including aluminum and steel. It enables single-pass welding of thick plate metals while considerably increasing the welding efficiency (Quintino et al., 2007). There are two laser welding modes: conduction and keyhole. In conduction mode, low energy power density deposition through shaped beam distribution leads to material fusion, but with weak penetration. Conversely, the keyhole mode benefits from high energy power density (above 10^6 W cm^{-2}), raising the material's temperature above its vaporization point. This leads to metal evaporation from the material surface, during which a keyhole is formed inside the material due to the vaporization pressure produced, also known as recoil pressure; the result is a deep weld penetration, ranging from millimeters and extending to centimeters (Dal & Fabbro, 2016; Steen & Mazumder, 2010). Different laser types, including continuous wave (CW), pulsed wave (PW), and modulated wave (MW) lasers, can be employed for welding, depending on the material being used. Aluminum and its alloys possess desirable properties such as oxidation and corrosion resistance, thermal and electrical conductivity, high reflectivity, low density, and strength. PW lasers effectively overcome the reflectivity of aluminum by delivering high energy density during pulse initiation while controlling the average power to minimize the overall heat. PW lasers are thus suitable options for welding aluminum and its alloys (Assuncao & Williams, 2013; Cavilha Neto et al., 2021; Hajavifard et al., 2016). Laser welding technology offers benefits such as high production rates, low energy input, faster welding speeds, smaller heat-affected zones, and narrower weld beads (Svenungsson et al., 2015). However, monitoring and controlling defects resulting from improper laser welding is

crucial in order to prevent environmental and economic consequences (Courtois et al., 2013; Svenungsson et al., 2015). Laser welding is associated with several defects, including humping (Bunaziv et al., 2020), porosities (Tan & Shin, 2014), spatters (Wu et al., 2017), and other imperfections induced by a small beam diameter. Additionally, geometric defects such as a lack of fusion (Yang & Jiang, 2021), sagged welds (Frostevarg, 2018), and concave root surfaces (Eshtayeh et al., 2015) can arise from imprecise beam positioning or pore formation during deep penetration welding as a result of high cooling rates (Courtois et al., 2013; Lee et al., 2002; Svenungsson et al., 2015). These defects considerably undermine the reliability of manufactured products (Guo et al., 2018). According to the literature, the majority of these defects arise from the dynamic variations in the keyhole, keyhole collapse, and melt pool oscillations. In particular, porosities resulting from keyhole instabilities are prevalent in aluminum welding, highlighting the importance of controlling keyhole and melt pool fluctuations for welding process stability and quality (Katayama et al., 2010; Lin et al., 2017). Scientists use experimental observations and numerical simulations to monitor laser welding and keyhole dynamics. However, high-quality laser welds performed through experiments often rely on trial and error, which is time-consuming, costly, and not environmentally friendly. The challenge is amplified when welding materials with high thermal conductivity or volatile chemical elements such as aluminum and its alloys. Experimentation also fails to accurately identify an efficient window of welding parameters due to the severe fluctuations of the keyhole and molten pool during the welding process (Pang et al., 2015; Wu et al., 2018). On the other hand, the time scale for keyhole formation and laser welding is in the order of one microsecond (10^{-6} s), making direct experimental observations difficult and invisible to the naked eye (Pang et al., 2016). Researchers have also used high-speed cameras to observe keyhole dynamics, but are limited to capturing surface phenomena of the fusion zone and vapor plume above the keyhole, missing important vapor plume dynamics inside. However, understanding keyhole fluctuations is closely tied to the behavior of vapor plumes, as the dynamics of vapor plumes can influence the stability and morphology of the keyhole (Tan et al., 2013). Alternatively, numerical simulations offer significant opportunities to model and comprehend the underlying mechanisms representing keyhole dynamics, which enables the prediction of defect formation (Duggirala et al., 2021; Li et al., 2019). To get a better grasp of

the mechanisms responsible for defect formation, numerical models should take into account fluid flow in the fusion zone, and determine the dynamic keyhole shape, which is tightly coupled with phase change, heat transfer, and fluid flow (Courtois et al., 2014). One of the early studies in this context was conducted by (Lee et al., 2002), who proposed a model of heat and fluid flow to describe spot laser welding. Their study integrated the Volume of Fluid (VOF) method into their model, addressing vapor phase and molten pool surface displacement, while also investigating dynamic instabilities and keyhole oscillations. In another study, Medal et al. developed a model for stationary laser welding and used a moving mesh method (Arbitrary Lagrangian–Eulerian) to track the free surface (Medale et al., 2007). Even though they considered recoil pressure and vaporization impacts at the free surface through specific boundary conditions, the presence of mesh distortion hindered the prediction of large displacements beyond the early stages of keyhole formation. Pang et al. used the LS method to expand a model for predicting keyhole formation and studied keyhole instability mechanisms under different heat input conditions (Pang et al., 2014). Courtois et al. presented a comprehensive heat and fluid flow model for laser welding, incorporating all three phases (liquid, solid, and vaporized metal) while employing the LS method to track the liquid/vapor interface. Their model effectively predicted keyhole oscillations and porosity formation, with acceptable agreements with experimental results. However, the significantly higher laser wavelength used in their research, compared to what is typically used in industrial welding, raises concerns about its applicability. Furthermore, the omission of the Marangoni effect, driven by temperature-induced surface tension gradients, might impact keyhole dynamics and the overall welding process, thereby forcing a further assessment of these factors (Courtois et al., 2013, 2014). Matsunawa and Katayama (Matsunawa et al., 2000, 2001) carried out a series of experimental investigations studying the impact of keyhole instability in deep penetration laser welding. Their findings corroborated the correlation between porosity formation and keyhole instabilities, which has not been examined in other welding fusions. The study disclosed an unstable keyhole in CW, exhibiting dynamic variations in size, shape, and depth. This led to bubble formation at the bottom part of the molten pool. An obstruction of the upward bubble flow by solidified metal resulted in keyhole-induced porosity. To control and address keyhole instability and its significant impact on defect formation, various methods

have been proposed, such as pulse modulation (Matsunawa et al., 2001), the use of side assisting gas (Kawahito et al., 2009), dual-beam welding (Wu et al., 2018), and beam oscillation (Ke et al., 2021). Ke et al. numerically studied keyhole-induced porosity in laser beam oscillating welding of 5A06 aluminum alloy. They evaluated the impact of different laser paths, including oscillating and non-oscillating paths, using a hybrid heat source model comprising an adaptive Gaussian profile with a double ellipsoid heat source. The results indicated that beam oscillation contributed to the formation of broader and more stable keyholes, a shallower and larger molten pool, and a more complex fluid flow, which minimized the likelihood of keyhole collapse, bubble formation, and porosity formation. Pulse modulation is another technique that can reduce the oscillation and instability of molten pools and keyholes (Ke et al., 2021). Matsunawa et al. extensively investigated keyhole and molten pool behavior, revealing that keyhole stability is adversely affected by intense metal evaporation on the keyhole wall at its front position. This leads to porosity formation inside the weld pool and in the final product. Their findings indicated that keyhole-induced porosity could be significantly suppressed by employing pulse modulation. By implementing proper duty cycles and frequencies in pulse modulation, the number of porosities can be reduced through the effective removal of holes benefiting from subsequent pulses and appropriate overlapping ratios (Matsunawa et al., 2001).

It can be seen in the literature that the energy density of the laser plays a crucial role in keyhole formation and behaviors. To the best of our knowledge, the impact of various laser energy pulse shapes on keyhole mode laser welding has not yet been covered in the literature; also, current pulse shapes are mostly confined to rectangular pulse shapes. The present study aims to investigate the impact of various laser energy pulse shapes (trapezium, triangular, rectangular, and variant–rectangular) on the keyhole and molten pool shape in a 2D axisymmetric configuration case. The results of keyhole penetration depth and morphology for these pulse shapes are compared with those from continuous laser welding to analyze the impact of pulse modulation on keyhole formation. Moreover, aluminum was chosen as the base metal for the investigation, as laser welding on it presents challenges in terms of numerical convergencies, and only a very limited number of numerical works have explored laser welding on the metal. Furthermore, given that aluminum is much lighter than other metals such

as steel, and given its high thermal conductivity, which makes it highly reflective, studying its weldability and improving its welding efficiency are a must, and greatly relevant to automotive manufacturing. Correspondingly, a novel numerical model equipped with modified techniques, such as modified mixture theory and the modified LS method, is utilized to investigate the phase transformations and coupled physics in this problem. The former defines the material properties in the entire domain, including the gas, solid, and liquid states, while the latter tracks the vapor/liquid interface inside the material due to the evaporation phenomena during laser welding. Additionally, the model developed in this paper is validated by comparing it with experimental results obtained by (Qin et al., 2011), shown in Section 4.1 of the Results and Discussion Section.

2.2 System Description and Material

The present paper presents a comparative numerical study of keyhole dynamics and the molten pool shape during laser spot welding of aluminum. A 2D axisymmetric model was utilized to represent the base metal. Its dimensions and configuration are depicted in Figure 2.1 (a). The choice of a 2D axisymmetric model for the simulation is rationalized based on the stationary spot laser welding assumption in this work. The laser beam position remains fixed within the coordinate system during the spot laser application, making the laser welding rotationally symmetric with respect to the vertical z-axis. This configuration thus represents a transversal cross-section of the sample for keyhole monitoring, as shown in Figure 2.1 (b). The plane used to monitor the keyhole morphology and depths in the Result and Discussion Section is also depicted in Figure 2.1 (c). It is worth mentioning that all the simulations, developments, models, and the investigated results of keyhole morphology and depth in the present paper were built in the graphical user interface of COMSOL Multiphysics 5.6. Using this software, the transition from a 2D axisymmetric model to a 3D model is accessible immediately. While COMSOL simplifies the process and offers 3D simulation results for our model, it is important to note that the software automatically imposes symmetry conditions for axisymmetric assumptions during calculations. This means it disregards variations and fluctuations occurring outside the plane of symmetry. Consequently, this excludes three-dimensional flow patterns or

convective currents, which play a role in influencing heat transfer and material transport dynamics within the weld pool region. Therefore, the model could not be considered a fully comprehensive 3D representation and does not fully mimic industrial scenarios. Nonetheless, it serves as a crucial initial step towards 3D modeling, aiding in the validation of the numerical model.

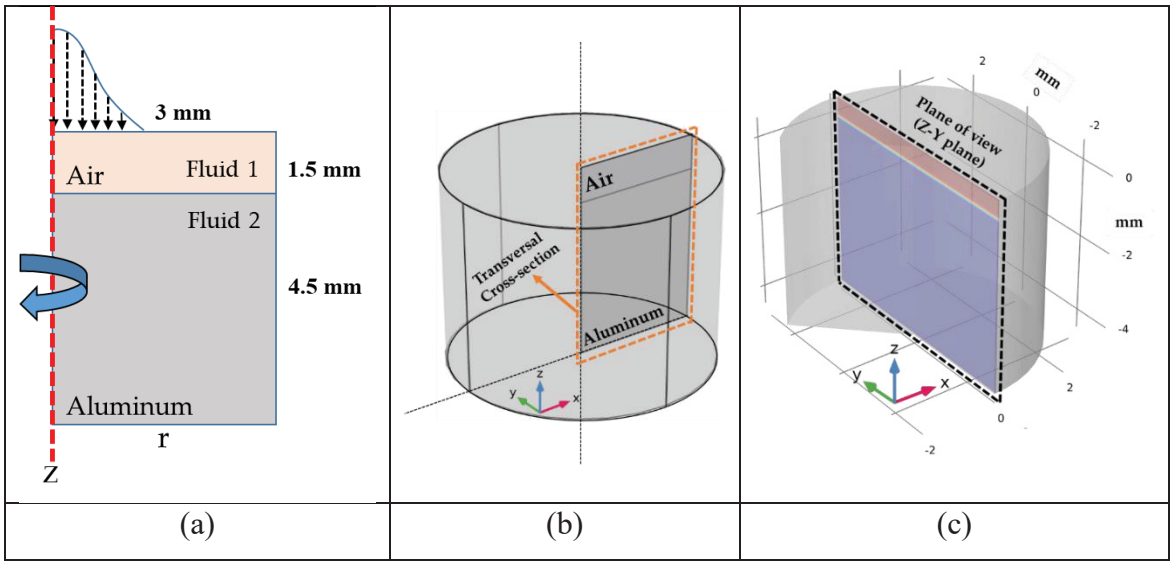

Figure 2.1 Schematic depiction of (a) 2D axisymmetric configuration of laser welding with Gaussian distribution used in the simulation and (b,c) 3D illustration of the problem generated in COMSOL Multiphysics 5.6 with definitions of the transversal cross-section of the domain and the plane used to monitor the keyhole morphology and penetration

The material used as the base metal was aluminum and its properties are presented in Table 2.1. Moreover, a series of tests were designed to investigate the impact of various laser and process parameters. All the investigated cases are presented in Table 2.2. Both CW and PW laser welding were examined for a detailed comparison. The PW laser welding was initially studied under different laser characteristics (LC), with the impact of various spot radii, laser frequency, and laser power on the keyhole penetration depth and shape investigated. Then, an investigation was performed into MW laser welding to examine the effects of pulse modulation, specifically, through the power modulation of waves, on the keyhole penetration depth. Various parameters, such as the pulse number, pulse width, and pulse shapes, were looked at. The pulse shapes selected for this study included rectangular, trapezium, and

triangular shapes, as well as multi-shape pulses such as rectangular–triangular, rectangular–trapezium, and variant–rectangular pulses. Results were compared with those of CW laser welding to determine the cases exhibiting the greatest stability and keyhole penetration depth. The equivalent average energy of the laser was kept constant for the pulse shape impact, ensuring that investigated cases were physically comparable under identical operational conditions and heat source characteristics. The different pulse shapes utilized in the present paper are shown in Figure 2.2.

Table 2.1 Thermophysical properties of aluminum
Adapted from Cho et al., (2018), Zhang et al., (2014), Zhang et al., (2016)

Property	**Symbol**	**Magnitude**
Solidus temperature	T_s	847 (K)
Liquidus temperature	T_l	905 (K)
Vaporization temperature	T_V	2743 (K)
Solid density	ρ_s	2700 (kg/m^3)
Liquid density	ρ_l	2385 (kg/m^3)
Solid thermal conductivity	k_s	238 (W/m/K)
Liquid thermal conductivity	k_l	100 (W/m/K)
Solid specific heat capacity	$C_{p,s}$	917 (J/kg/K)
Liquid specific heat capacity	$C_{p,l}$	1080 (J/kg/K)
Latent heat of fusion	L_m	3.896×10^5 (J/kg)
Latent heat of vaporization	L_V	9.462×10^6 (J/kg)
Radiation emissivity	ξ	0.2
Convective heat transfer coefficient	h	20 (W/m^2/K)
Thermal expansion coefficient	β	2.36×10^{-5} (1/K)
Dynamic viscosity	μ	1.6×10^{-3} (Pa.s)
Surface tension coefficient	σ	$0.95 \times (1 + 0.13 \times (1 - T/T_m))^{1.67}$ (N/m)
Surface tension coefficient with temperature	$\partial\sigma/\partial T$	-0.3×10^{-3} (N/m/K)

Table 2.2 List of the investigated sample cases with related operating properties for variations in laser characteristics (LC) and for modulated wave (MW) welding. An identical total 20 J laser power was used for cases MW10-17 and CW

Case No.	Laser Power	Pulse Width	Number of Pulses	Frequency of Laser	Period of Pulse	Pulse Shape	Spot Radius	Total on Time
Impact of spot radius								
LC1	6 kW	2 ms	1	100 Hz	0.01 s	Rectangular	300 µm	0.002 s
LC2	6 kW	2 ms	1	100 Hz	0.01 s	Rectangular	425 µm	0.002 s
LC3	6 kW	2 ms	1	100 Hz	0.01 s	Rectangular	525 µm	0.002 s
LC4	6 kW	2 ms	1	100 Hz	0.01 s	Rectangular	725 µm	0.002 s
Impact of frequency								
LC5	6 kW	1 ms	3	50 Hz	0.0066 s	Rectangular	300 µm	0.003 s
LC6	6 kW	1 ms	3	100 Hz	0.0033 s	Rectangular	300 µm	0.003 s
LC7	6 kW	1 ms	3	150 Hz	0.0022 s	Rectangular	300 µm	0.003 s
Impact of laser power								
LC8	2 kW	3 ms	1	100 Hz	0.01 s	Rectangular	300 µm	0.003 s
LC9	4 kW	3 ms	1	100 Hz	0.01 s	Rectangular	300 µm	0.003 s
LC10	6 kW	3 ms	1	100 Hz	0.01 s	Rectangular	300 µm	0.003 s
Impact of pulse width								
MW1	6 kW	0.5ms	1	100 Hz	0.01 s	Rectangular	300 µm	0.0005 s
MW2	6 kW	1 ms	1	100 Hz	0.01 s	Rectangular	300 µm	0.001 s
MW3	6 kW	2 ms	1	100 Hz	0.01 s	Rectangular	300 µm	0.002 s
MW4	6 kW	3 ms	1	100 Hz	0.01 s	Rectangular	300 µm	0.003 s
Impact of pulse number								
MW5	4 kW	0.5 ms	2	100 Hz	0.005 s	Rectangular	300 µm	0.001 s
MW6	4 kW	0.5 ms	6	100 Hz	0.0016 s	Rectangular	300 µm	0.003 s
MW7	4 kW	0.5 ms	10	100 Hz	0.001 s	Rectangular	300 µm	0.005 s
MW8	4 kW	0.5 ms	14	100 Hz	0.00071 s	Rectangular	300 µm	0.007 s
MW9	4 kW	0.5 ms	18	100 Hz	0.00055 s	Rectangular	300 µm	0.009 s
Impact of continuous laser welding								
CW	2 kW	10 ms	1	100 Hz	0.01 s	Continuous	300 µm	0.01 s
Impact of pulse shape								
MW10	4 kW	5 ms	1	100 Hz	0.01 s	Rectangular	300 µm	0.005 s
MW11	4 kW	8 ms	1	100 Hz	0.01 s	Trapezium	300 µm	0.008 s
MW12	4 kW	10 ms	1	100 Hz	0.01 s	Triangle	300 µm	0.01 s
MW13	4 kW	8 ms	1	100 Hz	0.01 s	Trap.: t2	300 µm	0.008 s
MW14	1–3 kW	Variant	1	100 Hz	0.01 s	Var.-Rect.	300 µm	0.01 s
MW15	2–4 kW	Variant	1	100 Hz	0.01 s	Rect.-Tri.	300 µm	0.008 s
MW16	2–3 kW	Variant	1	100 Hz	0.01 s	Rect.-Trap.	300 µm	0.008 s
MW17	2–3 kW	Variant	1	100 Hz	0.01 s	Rect.-Rect.	300 µm	0.008 s

Var.: variant, Rect.: Rectangular, Trap.: Trapezium, Tri. Triangle, t2: type 2.

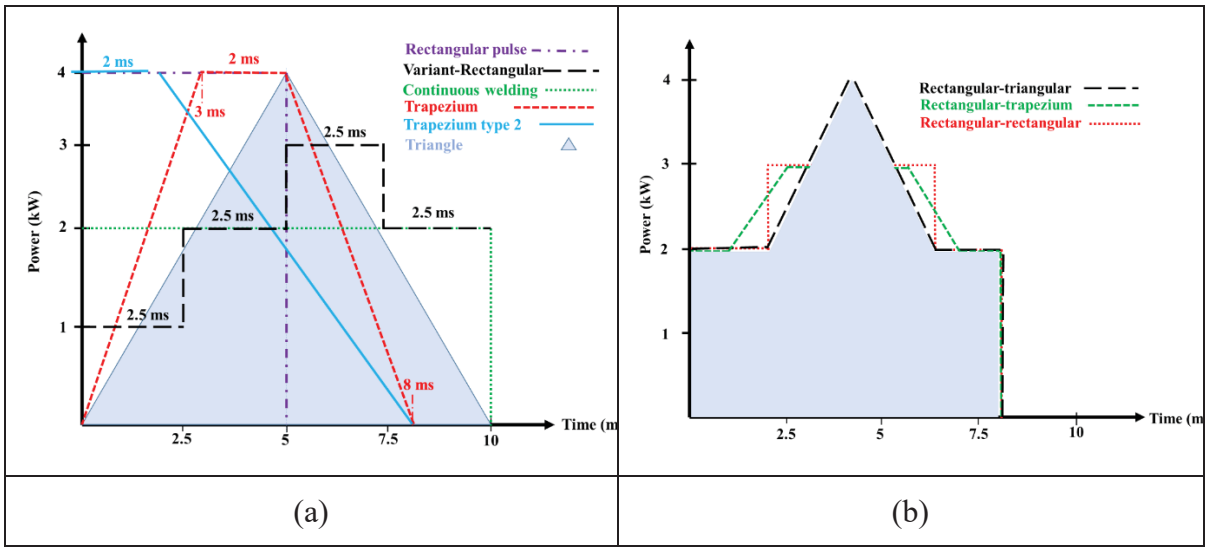

Figure 2.2 Complete schematic of all the laser energy pulse shapes used for power modulation for (a) MW10-MW14 and (b) MW15-MW17

2.3 Numerical Approach and Methods

2.3.1 Heat and Fluid Flow Model

Laser heating occurs when the energy absorbed by the base metal from the laser beam converts into thermal energy. Subsequently, the temperature of the material surface increases due to the absorbed energy of the laser by the material. When the temperature surpasses the melting and vaporization thresholds, the material undergoes consecutive phase transitions, including fusion and evaporation, leading to keyhole formation (T. Zhang et al., 2021). The dynamics of the fluids are modeled by adding the impacts of recoil pressure, surface tension, and hydrostatic and hydrodynamic pressures (Svenungsson et al., 2015; T. Zhang et al., 2021). Recoil pressure acts to open the keyhole, while the other forces act to close it, with the surface tension effect dominating the shape of the vapor/liquid interface, particularly at the top of the melt pool. The surface tension effect is attributable to two factors, namely, the Marangoni effect and the curvature effect, caused by the tangential and normal forces exerted on the free surface of the fluid (Chen et al., 2019; Svenungsson et al., 2015). Among the methods developed to model the free surface during a finite element computation, the modified LS method, as an Eulerian approach, is used in this study to model the free surface of the fluid and the vapor/liquid

interface, as well as calculate the tangential and normal components of the free surface. Additionally, a new method called modified mixture theory is used to deal with phase transitions and discontinuities at the interfaces in the finite element computation (Kong & Kovacevic, 2010; Y. Zhang et al., 2014). The present paper aims to use the above approaches to represent and simulate the keyhole formation and the molten pool while taking into account the surface tension effects, free surface motion, buoyancy forces, recoil pressure, evaporation impacts, and mass loss due to evaporation. The following assumptions were made in the numerical investigation:

- The flow of molten material inside the fusion zone was assumed Newtonian, incompressible, and laminar.
- The temperature-dependent effects on the thermophysical properties and absorption coefficients were neglected for the sake of simulation simplicity.
- A porous medium, saturated with the liquid molten metal, was assumed for the mushy zone (Y. Zhang et al., 2014).
- A Gaussian laser beam distribution was assumed for the heat source.
- The impact of natural convection was added using the Boussinesq approximation (Ardahaie et al., 2019).
- Plasma and the Knudsen layer were not taken into account.
- Multiple reflections of the laser beam were neglected in this model.
- The masking effect was not considered due to our explicit assumption of neglecting multiple reflections and stationary Gaussian distribution, and the laser beam is assumed to uniformly irradiate the keyhole wall without obstruction.
- The vaporized material known as metallic vapor was considered an ideal gas and transparent to the incoming laser beam.
- The thermal enthalpy porosity technique was used to track the solid/liquid interface and adds the impacts of temperature-dependent phase transitions (melting and vaporization) on the specific heat capacity in the heat transfer model (Y. Zhang et al., 2014).

2.3.2 Governing Equations

This section presents the Navier–Stokes and conservation equations in a standard format applicable to 2D axisymmetric configurations. It is noted that under the 2D axisymmetric assumption, the gradient of parameters is independent of the rotational angle. The transport phenomena in all three phases are calculated by simultaneously solving the equations of mass conservation, momentum, and energy conservation (Equations (2.1)– (2.3)):

$$\nabla \cdot \vec{u} = 0 \tag{2.1}$$

$$\rho\left(\frac{\partial \vec{u}}{\partial t} + (\vec{u} \cdot \nabla)\vec{u}\right) = \nabla \cdot [-pI + \mu(\nabla\vec{u} + (\nabla\vec{u})^T)]) + \rho\vec{g} + \vec{F}_{Vol} \tag{2.2}$$

$$\rho C_p \frac{\partial T}{\partial t} + \rho C_p \vec{u} \cdot \nabla T = \nabla \cdot (k\nabla T) \tag{2.3}$$

where T represents the temperature, ρ denotes material density, C_p is the specific heat capacity, k stands for the thermal conductivity, and $\vec{u}$ the velocity vector. Moreover, I denotes the identity matrix, p represents the pressure, μ is the dynamic viscosity, and $(\nabla\vec{u})^T$ indicates the transpose of the gradient of the velocity vector $\vec{u}$. $\rho\vec{g}$ represents the effect of gravity, $\vec{F}_{Vol}$ is the total body force which comprises impacts of surface tension ($\vec{F}_{st}$) and buoyancy effect ($\vec{F}_{Buoyancy}$) through a Boussinesq approximation and Darcy damping force ($\vec{F}_{Darcy}$), which are further described later in this work. The present paper uses various methods to model the melting/solidification and evaporation phase changes. The melting/solidification is modeled using the thermal enthalpy porosity technique (Bonacina et al., 1973; Y. Zhang et al., 2014), while the evaporation is modeled using the conservative modified LS method (Olsson & Kreiss, 2005). Moreover, modified mixture theory is also utilized to apply the mixture effects easing the finite element computation at the interface, especially for the elements combined with more than one phase (Kong & Kovacevic, 2010; Y. Zhang et al., 2014). Together with the LS method, modified mixture theory helps to deal with the discontinuities at the interfaces during the transition from one phase to another. It is noted that all these methods and the mixture properties were added to the heat transfer, laminar flow, and level-set interfaces of

COMSOL individually. Then, to apply the coupling effects of these methods and interfaces to work simultaneously in favor of the calculation, a specific coupling interface of COMSOL Multiphysics named the Multiphysics interface was used. Correspondingly, the laminar flow, mixture properties, and level-set were coupled using the two-phase flow interface while the laminar flow and the heat transfer interfaces were coupled using the nonisothermal flow of the Multiphysics interface. The two coupling effects were then coupled under the Multiphysics interface of COMSOL. The methods used in this paper are given in detail in the subsequent sections.

2.3.3 Modified Mixture Theory

Some previous studies applied modified mixture theory for the solid and liquid phases (Kong & Kovacevic, 2010), due to the coexistence of the solid and liquid phases in a single cell for some regions within the mushy zone. The method uses a mixture of material properties derived from both solid and liquid states for density, specific heat, conductivity, and dynamic viscosity, thereby referred to as a mixture theory. However, the present study proposes that the so-called mixture theory can be further developed and extended for application to all three phases in the same fashion. Domain 2 in Figure 2.1 contains all three phases following the occurrence of melting and vaporization when the keyhole is formed. Therefore, to account for the impact of each phase in the case of the coexistence of all three phases in a single cell, a mixture of properties derived from all three states (solid, liquid, gas) is also used for the material properties to help solve the governing equations.

2.3.3.1 Conduction Mode

In the initial stages of the welding process, the primary welding mode is the conduction mode, which consists of the solid and liquid phases. Here, the temperature is not high enough to induce evaporation, but rather only exceeds the melting temperature to initiate melting. Therefore, only the liquid and solid phases are available in this mode. To represent the material properties in this mode, a mixture of temperature-dependent properties of solid and liquid

phases of the material is defined, and the domain is considered as a bulk mixture of solid/liquid phases (Steen & Mazumder, 2010). Equations (2.4)– (2.7) are used to describe this mode:

$$\rho_{sl} = V_s\rho_s + \rho_l V_l \tag{2.4}$$

$$k_{sl} = V_s k_s + k_l V_l \tag{2.5}$$

$$\mu_{sl} = V_s\mu_s + \mu_l V_l \tag{2.6}$$

$$Cp_{sl} = \frac{\rho_s}{\rho_{sl}} V_s Cp_s + \frac{\rho_l}{\rho_{sl}} V_l Cp_l \tag{2.7}$$

where ρ, k, μ, Cp are the density, thermal conductivity, dynamic viscosity, and specific heat capacity of the aluminum, respectively. Moreover, V is specified as the volume fraction of the material, which is distinguished by using s and l subscripts for the solid and liquid phases.

2.3.3.2 Transition and Keyhole Mode

The more the heat flux of the laser is irradiated on the surface of the aluminum, the more the temperature is increased until the temperature reaches the boiling temperature of the material. The aluminum therefore transitions from conduction to keyhole mode by exceeding the boiling temperature. At this stage, Domain 2 comprises solid, liquid, and gas phases of aluminum because a portion of the aluminum is vaporized and forms the keyhole (Steen & Mazumder, 2010). Hence, to account for the material properties in this mode and solve the Navier–Stokes equations, a mixture of solid, liquid, and gas temperature-dependent properties of the material is defined. In this approach, each cell in the domain is treated as a liquid with properties of a mixture of solid, liquid, and gas phases.

This section presents the equations used to define the mixture properties of the computational domain. The notations *g*, *l*, and *s* in the following equations are used to specify the gas, liquid, and solid phases, where ρ_{sl}, and ρ_{slg} denote the densities of the bulk mixture of solid/liquid and solid/liquid/gas, respectively. Equations (2.8)– (2.10) define the mixture properties for this mode:

$$\rho_{slg} = \rho_{sl} V_{f,2} + \rho_g V_{f,1} \tag{2.8}$$

$$k_{slg} = k_{sl} V_{f,2} + k_g V_{f,1} \tag{2.9}$$

$$Cp_{slg} = \frac{\rho_{sl}}{\rho_{slg}} V_{f,2} Cp_{Al,eff} + \frac{\rho_g}{\rho_{slg}} V_{f,1} Cp_g \tag{2.10}$$

where $V_{f,1}$ and $V_{f,2}$ are respectively the volume fraction of gas (Domain 1) and the volume fraction of solid/liquid bulk (Domain 2). ρ_{slg}, k_{slg}, and Cp_{slg} are the density, thermal conductivity, and specific heat capacity of the bulk mixture of gas/liquid/gas in Domain 2, respectively.

2.3.4 Tracking the Solid/Liquid Interface

2.3.4.1 Thermal Enthalpy Porosity Technique

To comprehend the definition of $Cp_{Al,eff}$, an enthalpy porosity technique commonly used to account for the phase change transition in fixed-grid techniques has been defined (Bonacina et al., 1973; Y. Zhang et al., 2014). The technique defines an equivalent specific heat capacity $Cp_{Al,eff}$ to add the latent heat effects of fusion and vaporization in which the temperature interval for melting and vaporization are based on Equations (2.12) and (2.13), respectively. Taking two Gauss functions of D_m and D_V around the melting temperature (T_m) and vaporization temperature (T_V) and multiplying them by latent heats of fusion (L_m) and vaporization (L_V), the equivalent specific heat capacity is defined by adding the specific heat of solid/liquid mixture Cp_{sl} to the equation, as presented in Equations (2.11)– (2.13). The smoothing interval for the fusion (dT_m) is set to 29 K, based on the solidus and liquidus temperatures of the material ($\frac{T_l - T_s}{2}$) (Mayi et al., 2020). In this study, the smoothing interval of vaporization (dT_V) is set to 50 K, as proposed by Tomashchuk et al. (Tomashchuk et al., 2016):

$$Cp_{eff} = Cp_{sl} + L_m D_m + L_V D_V \tag{2.11}$$

$$\text{(a) } D_m = exp^{\left(\frac{-(T-T_m)^2}{dT_m{}^2}\right)} \Big/ \sqrt{\pi dT_m{}^2} \qquad \text{(b) } T_m - dT_m \rightarrow T_m + dT_m \tag{2.12}$$

$$\text{(a) } D_V = exp^{\left(\frac{-(T-T_V)^2}{dT_V{}^2}\right)} \Big/ \sqrt{\pi dT_V{}^2} \qquad \text{(b) } T_V - dT_V \to T_V + dT_V \tag{2.13}$$

The enthalpy porosity technique also helps to identify and localize the solid/liquid interface during fusion caused by laser welding. In this technique, the melt interface is treated implicitly using a quantity known as the volume fraction of liquid (V_l), which is presented in Equation (2.14). In fact, the partially solidified region known as the mushy zone is treated as a porous medium. For each of the cells, the liquid fraction represents the porosity inside, in which the porosity and the liquid velocity are zero for the fully-solidified regions. The flow in the mushy zone follows the Darcy law, which induces a Darcy damping force. This force is governed by a frictional dissipation within the mushy zone based on the Carman–Kozeny equation, Equation (2.17), for flow through a porous medium. Consequently, the more the porosity in the mushy zone diminishes, the more the velocity and permeability decrease, and the liquid velocity becomes zero for the fully-solidified regions (Wei et al., 2016; Y. Zhang et al., 2014). The Darcy damping force can be defined in the momentum equation, Equation (2.2), using a source term specified in Equations (2.16) and (2.17)**,** where *b* is used to avoid division by zero, *d* is a constant proportional to the dendrite size, which is considered constant and set to 10^{-2} cm (Pang et al., 2011), and V_l and V_s are volume fractions of liquid and solid.

$$V_l = \begin{cases} 1, & T > T_l \\ \dfrac{T - T_s}{T_l - T_s}, & T_s \le T \le T_l \\ 0, & T < T_s \end{cases} \tag{2.14}$$

$$V_S = 1 - V_l \tag{2.15}$$

$$F_{Darcy\ Damping} = -\mu_l K \vec{u} \tag{2.16}$$

$$K = \frac{\frac{180}{d^2}(1 - V_l)^2)}{V_l{}^3 + b} \tag{2.17}$$

2.3.5 Tracking the Vapor/Liquid Interface

2.3.5.1 Modified Level-Set Method

Due to the numerous driving forces and temperature-dependent material properties acting on it, the liquid/vapor interface is the most challenging phenomenon to tackle in keyhole mode laser welding. To address this challenge, this study proposes a modified format of the conservative LS method, which integrates the Volume of Fluid (VOF) and the narrow band LS method while incorporating a gas dynamic source term (Olsson & Kreiss, 2005). This source term considers the effects of evaporation and the boiling effect induced by mass loss and recoil pressure on the interface. The standard and general format of the transport equation of the LS method is presented in Equation (2.18):

$$\frac{\partial \phi}{\partial t} + \vec{u} \cdot \nabla \phi + \gamma_{ls} \nabla \cdot \left(\phi(1-\phi) \frac{\nabla \phi}{|\nabla \phi|} - \epsilon_{ls} \nabla \phi \right) = 0 \tag{2.18}$$

where γ_{ls} is the reinitialization parameter related to the flow velocity and ϵ_{ls} the parameter that controls the interface thickness. Furthermore, ϕ is the level-set variable defined using a Heaviside function (Olsson & Kreiss, 2005). The LS variable varies smoothly between 0 and 1 within the interface layer and is set to 0.5 for the vapor/liquid interface, as shown in Equation (2.19). The definition of this variable throughout all elements of the computational domain, along with its transport using fluid flow calculations, helps to track the vapor/liquid interface and distinguishing between gaseous and condensed phases.

$$\phi(x,t) = \begin{cases} 0, & T > T_V, & dist(x, \Gamma(t)) < -\epsilon_{ls} \\ 0.5, & T_l < T < T_V, & |dist(x, \Gamma(t))| \leq \epsilon_{ls} \\ 1, & T < T_l, & dist(x, \Gamma(t)) > \epsilon_{ls} \end{cases} \tag{2.19}$$

Here, γ_{ls}, the reinitialization parameter, ensures that the level set function of $\phi(x,t)$, remains a signed distance function near the interface $\Gamma(t)$, where $\phi(x,t) \approx dist(x, \Gamma(t))$. In this study,

the surface tension force was explicitly decomposed into two distinct components: the normal curvature-driven capillary force ($\gamma\vec{n}k$), and the tangential Marangoni shear stress ($\nabla_s\gamma$). The unit normal vector ($\vec{n}$) as well as curvature (k) of the interface are defined and computed directly from LS function $\phi(x,t)$ using Equations (2.20) and (2.21) (Kong & Kovacevic, 2010; Y. Zhang et al., 2014).

In a 2D axisymmetric configuration, r, and z are the radial and axial coordinates. The tangential surface gradient operator $\nabla_s\,\gamma$ is implemented using $(\mathrm{I}-\vec{n}\otimes\vec{n})\cdot\nabla_\gamma$ where I is the identity tensor, $\vec{n}$ the normal vector to the interface, and $\vec{n}\otimes\vec{n}$ is the dyadic (tensor) product of the normal vector with itself, resulting in a projection onto the normal direction. Also, ∇_γ is the full spatial gradient of the surface tension field defined by $(\partial\gamma/\partial r)\vec{e}_r+\ (\partial\gamma/\partial z)\vec{e}_z$ where $\vec{e}_r$, and $\vec{e}_z$ are radial and axial unit vectors, respectively.

$$\vec{n}=\frac{\nabla\phi}{|\nabla\phi|} \tag{2.20}$$

$$k=\nabla\cdot\left(\frac{\nabla\phi}{|\nabla\phi|}\right) \tag{2.21}$$

Moreover, a delta function of the ϕ variable is defined in Equation (2.22) to facilitate smooth transitions and phase traversal at the interfaces during the finite element computation (Y. Zhang et al., 2014). This parameter definition aids in minimizing discontinuities, particularly for temperature-dependent material properties and forces that should only apply at the interface, such as the surface tension, recoil pressure, and the laser heat source. By multiplying these forces along with any other terms with the delta function, they are confined to the vapor/liquid interface during calculations, ensuring they possess a non-zero value solely at that interface.

$$\delta=6|\phi(1-\phi)||\nabla\phi| \tag{2.22}$$

2.3.6 Definition of Source Terms and Driving Forces on the Interface

2.3.6.1 Recoil Pressure, Mass Loss, and Evaporative Source Term of Heat Flux

As mentioned before, when the laser beam irradiates on the material surface, a keyhole is formed as the temperature exceeds the vaporization point, leading to the formation of a vapor pressure known as recoil pressure. The mass loss rate due to evaporation is derived by writing Navier–Stokes, continuity, and energy equations across the Knudsen layer. The mass loss rate is then expressed by the Hertz–Langmuir relation (Mayi et al., 2020), as presented in Equation (2.23):

$$\dot{m}_{H-L} = \sqrt{\frac{M}{2\pi R}} \frac{P_{sat}(T)}{\sqrt{T}} (1 - \beta_r) \tag{2.23}$$

where β_r represents the retro-diffusion coefficient and considered zero here based on what offered by Courtois et al. (Courtois et al., 2014), while R and M denote the universal gas constant and the molar mass of the evaporated particles, respectively. Moreover, P_{sat} is the saturated vapor pressure expressed based on the Clausius–Clapeyron law as presented in Equation (2.24) (Mayi et al., n.d., 2020), where P_{atm} is defined as the atmospheric pressure and T_v the evaporation temperature at the atmospheric pressure.

$$P_{Sat} = P_{atm}\, exp\left[\frac{ML_v}{RT_v}\left(1 - \frac{T_v}{T}\right)\right] \tag{2.24}$$

The literature commonly employs empirical formulas to describe the recoil pressure. Mayi et al. (Mayi et al., 2020) introduced a formula for recoil pressure as $P_{rec} = {}^{1}/_{2}\,(1 + \beta_r)P_{Sat}(T)$ while Lee et al. (Lee et al., 2002) and Geiger et al. (Geiger et al., 2009) proposed that the recoil pressure can be determined as $P_{rec} \cong 0.54P_{atm}\exp\left(\Delta H_{LV}\, T - T_{LV}/RTT_{LV}\right)$, where ΔH_{LV} represents the evaporation enthalpy. However, a more tangible approach is to add the impact of the recoil pressure into the continuity equation by introducing a source term, as presented by Zhang et al. (Y. Zhang et al., 2014) and Courtois et al. (Courtois et al., 2014). Due to the

differences between the gaseous and liquid densities ($\rho_l - \rho_v$) in the vicinity of the vapor/liquid interface, the incompressibility of the fluid phases cannot be satisfied on two opposite sides of the interface. Hence, a source term is added to the continuity equation using the delta function of the LS variable defined in Section 3.2.3 to smooth the transition between phases for density variations and also add the mass loss impact and the recoil pressure. Correspondingly, the source term will be non-zero only on the interface, as presented in Equation (2.25) for the modified continuity equation, and the incompressibility of phases is satisfied for all the regions far from the interface (Courtois et al., 2014; Y. Zhang et al., 2014):

$$\nabla \cdot \vec{u} = \delta(\phi)\dot{m}_{H-L}\left(\frac{\rho_l - \rho_v}{\rho^2}\right) \tag{2.25}$$

Moreover, another source term is also added to the transport equations of the LS variable to enhance the impact of evaporation phenomena induced by mass loss only on the interface. The source term will smooth the transport of the LS variable in the finite element computation on both sides of the interface using the delta function of the LS variable, volume fractions of gaseous and liquid phases, and their corresponding densities. The modified form of the transport equations of the LS variable is presented in Equation (2.26).

$$\frac{\partial \phi}{\partial t} + \vec{u} \cdot \nabla\phi - \delta(\phi)\dot{m}_{H-L}\left(\frac{V_{f,1}}{\rho_v} + \frac{V_{f,2}}{\rho_l}\right) + \gamma_{ls}\nabla.\left(\phi(1-\phi)\frac{\nabla\phi}{|\nabla\phi|} - \epsilon_{ls}\nabla\phi\right) = 0 \tag{2.26}$$

where $V_{f,1}$ and $V_{f,2}$ are the volume fraction of gas (Domain 1) and the volume fraction of solid/liquid bulk (Domain 2), respectively.

2.3.7 Definition of the Surface Tension Impact and Boussinesq Approximation

Given the role of the delta function of the LS variable in smoothing transitions between phases and the application of the driving forces only on the interface, the surface tension impact and the buoyancy force are added to the momentum equation as body forces. Equations (2.27) and (2.28) are presented for the surface tension force (curvature and Marangoni effect) and the

buoyancy force, respectively. Equation (2.28) considers the buoyancy effect but only within the molten aluminum using the term ϕ, and the effect is neglected in the gas phase due to intense vapor velocity. Then, the final format of the Navier–Stokes equations is presented in Equation (2.29). It should be noted that the buoyancy force is only applied within the molten pool utilizing the LS variable ϕ, and its impact is negligible in the gas phase (Courtois et al., 2013, 2014).

$$\vec{F}_{st} = (\gamma \vec{n} k - \nabla_s \gamma)\delta(\phi) \tag{2.27}$$

$$\vec{F}_{Buoyancy} = -\rho_l \beta_l (T - T_m)\vec{g}\phi \tag{2.28}$$

$$\rho\left(\frac{\partial \vec{u}}{\partial t} + (\vec{u}\cdot\nabla)\vec{u}\right) = \nabla.[-pI + \mu(\nabla\vec{u} + (\nabla\vec{u})^T)]) + \rho\vec{g} - \rho_l\beta_l(T - T_m)\vec{g}\phi - \mu_l K\vec{u} + (\gamma\vec{n}k - \nabla_s\gamma)\delta(\phi) \tag{2.29}$$

where β_l is the thermal expansion coefficient and γ is the coefficient of surface tension.

2.3.8 Definition of the Heat Source and Evaporative Energy Equation

As depicted in Figure 1, the initial vapor/liquid interface is subjected to a Gaussian distribution of the laser heat flux before deformation. Evaporation loss occurs due to the laser's high energy density, with the laser energy calculated by Equations (2.30) and (2.31):

$$q_{Laser} = \frac{\alpha n P_{Laser}}{\pi R_{eff}^2} exp\left(\frac{-nr^2}{R_{eff}^2}\right) B_t \tag{2.30}$$

$$B_t = \begin{cases} 1, & t \le t_p \\ 0, & t > t_p \end{cases} \tag{2.31}$$

where P_{Laser} and B_t are the laser peak power and the temporal laser distribution used to apply the effect of the pulse wave laser welding, respectively. R_{eff} is the effective spot radius of the laser beam and t_p is the pulse duration. The parameter n denotes the form factor for the Gaussian distribution, which is set to 2 in the present paper, as used also by Zhang et al. (Y. Zhang et al., 2014). α is the absorption coefficient of aluminum which is considered proportional to $354.67 \times \sqrt{(-1 + 1.25 \times 10^{-2} \times T) \times 10^{-8}}$ as offered by Zhang et al. (Y.

Zhang et al., 2014). Moreover, in our approach, constant laser absorption is considered throughout the simulation domain. It is worth mentioning that aluminum is known to be a highly reflective material with high thermal conductivity, particularly in the spectrum commonly used in laser welding. As a result, the absorption coefficient of aluminum is relatively low compared to other materials, and the absorption of laser energy by the material remains constant within the typical operating parameters of this stationary pulsed spot laser welding. Furthermore, for the specific geometry and conditions considered in our simulation, the distribution of laser energy and absorption within the workpiece is governed by factors such as Gaussian laser beam profile, spot size, and material properties. These factors contribute to a relatively uniform distribution of absorbed laser energy within the keyhole region, supporting the assumption of constant absorption.

To apply the laser heat flux on the material surface and account for the energy loss due to evaporation, the delta function of the LS variable is utilized again. In fact, the energy loss due to evaporation is subtracted from the laser energy density, and the resulting energy is multiplied by the delta function of the LS variable to exert these effects on the vapor/liquid interface. This resulting energy is then added to the energy equation as a body force. The modified energy equation is presented in Equation (2.32):

$$\rho C_p \frac{\partial T}{\partial t} + \rho C_p \vec{u} \cdot \nabla T = \nabla \cdot (k \nabla T) + (q_{Laser} - Q_{vapor})\, \delta(\phi) \tag{2.32}$$

$$Q_{vapor} = -L_V \dot{m}_{H-L} \tag{2.33}$$

2.3.9 Numerical Schemes

The entire 2D axisymmetric model was developed using COMSOL Multiphysics 5.6 within the computational fluid dynamics module to calculate the fluid flow, heat transfer, and LS transport equations. A total of 37,500 elements were used for the computational domain after conducting a mesh independency check, and the mapped typed mesh with quadrilateral elements was used with extra fine meshes as depicted in Figure 2.3, which were calibrated for fluid dynamic calculation. The maximum and minimum element sizes were equally set to 0.02 mm. The simulation lasted for around 17 h for 10 ms of the laser welding process, and all the

calculations were done using a classical computer equipped with an Intel® Xenon® Gold 5118 CPU with 12 cores, 24 logical processors, and 128 GB RAM. All the time steps were chosen and set on 10 µs. A PARDISO direct solver with a preordering algorithm of Nested dissection multithreaded was used for the fluid flow calculation. The LS transport and heat transfer equations were solved using a PARDISO direct solver with the preordering algorithm of the automatic feature. It is worth mentioning that the viscosity at the vicinity of vapor and solid/liquid interface was defined using the level set variable, and dynamic viscosities of fluid 1 and 2, as shown in Figure 2.1 (a) applying equation of $\mu = \mu_1 + (\mu_2 - \mu_1)\phi$ as offered by (Kong & Kovacevic, 2010; Y. Zhang et al., 2014).

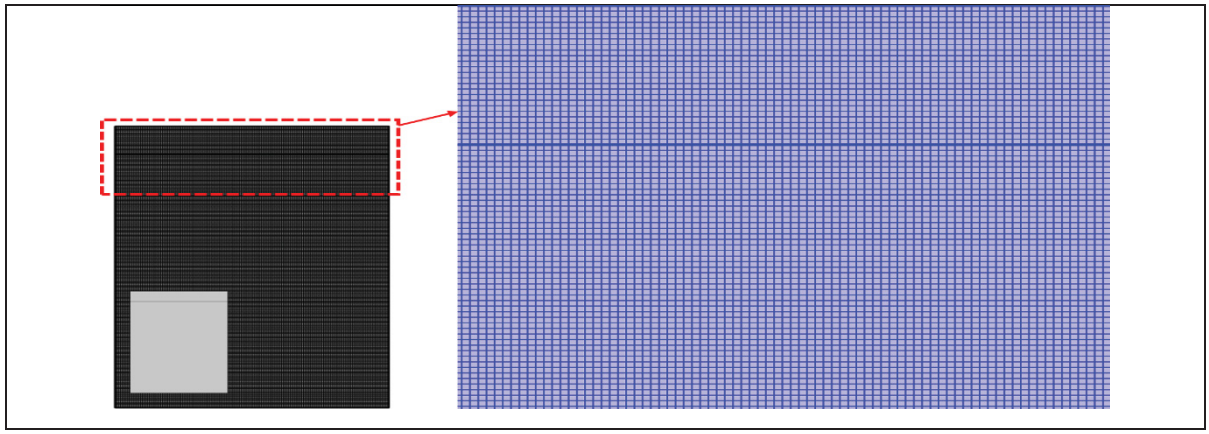

Figure 2.3 Computational domain and the generated extra fine mapped mesh

2.3.10 Sensitivity Analysis of the Numerical Parameters

In order to obtain reliable outcomes, the independency verification of the number of mesh elements, values of the reinitialization parameter, and the parameter controlling the interface thickness of the level-set technique were checked before the simulation process. The convergency trend and the keyhole depths were monitored as criteria for choosing the best parameters when conducting the sensitivity analysis. The analysis was done iteratively by refining simulation parameters through the steps given in Table 2.3. Initially, the mesh sensitivity analysis was performed by using four different numbers of mesh elements: 16,968, 24,320, 37,500, and 48,045. The total number of mesh elements is then selected to be 37,500

since the keyhole morphology and depth showed no considerable difference with further increase in mesh elements. Then, the analysis was conducted on level-set parameters, and the most optimum values for the reinitialization parameter and the parameter controlling the interface thickness were found to be 5 m/s and 0.03 mm, respectively. The chosen parameters showed better computational efficiency and convergency trend, and further variations in the parameters did not lead to significant changes in the keyhole depth and morphology.

Table 2.3 List of the investigated tests for sensitivity analysis of the used parameters, namely, number of mesh elements (NOME), reinitialization parameter (γ_{ls}), and the parameter controlling the interface thickness (ϵ_{ls})

Steps	Constant Values	Test Parameter	Values	Keyhole Depth
Step 1	Time step: 10 μs	NOME	16,968	4.128 mm
			24,320	4.011 mm
			37,500	3.948 mm
			48,045	3.921 mm
Step 2	$\gamma_{ls} = 3$ m/s	ϵ_{ls}	0.01 mm	Convergency error
			0.02 mm	4.058 mm
			0.03 mm	3.948 mm
			0.04 mm	3.942 mm
Step 3	$\epsilon_{ls} = 0.03$ mm	γ_{ls}	1 m/s	4.175 mm
			3 m/s	3.948 mm
			5 m/s	3.837 mm
			7 m/s	3.839 mm

2.4 Results and Discussions

This section presents the results of the investigated cases in detail. Temperature variations within the base metal, vapor/liquid interfaces, and keyhole/molten pool shapes are examined consecutively. The first part covers the validation of the numerical model developed in this study by comparing it with a previous experimental study. Then, an overall justification is provided for the underlying physical phenomena occurring during the laser welding process, along with an exploration of the methods proposed and employed to address present interfaces and phase changes. The subsequent subsections are devoted to the impact of various laser characteristics and power wave modulations on keyhole penetration and propagation.

2.4.1 Accuracy Verification of Simulation Results Using Experimental Validation

The proposed model in this paper is validated by comparing it with experimental results obtained by Qin et al. (Qin et al., 2011) Specifically, the keyhole penetration depth, shape, and diameter are compared to the morphology of the keyhole observed by Qin et al. (Qin et al., 2011). To ensure the physical comparability of the results, the simulation in this study employs the same laser characteristics as those used by Qin et al. (Qin et al., 2011). Correspondingly, the laser power and its pulse width were set to 18 J and 3 ms. Additionally, the laser's focal length and spot radius were both set to 60 mm and 300 μm, respectively. According to both simulation and experimental findings, the keyhole penetration depth was 3.837 mm numerically, closely aligning with the experimental value of 3.824 mm reported by Qin et al. (Qin et al., 2011). The morphology of the keyhole propagation was also compared with experimental results, as shown in Figure 2.4. The spot diameter of the keyhole on the surface in the simulation and experimental result were approximately 0.937 mm and 0.936 mm, respectively. Moreover, the maximum keyhole width reported experimentally was approximately 0.407 mm. Also, the keyhole width from the numerical simulations varies between 0.310 mm and 0.51 mm. It was found that the proposed numerical approach can well predict the keyhole both in depth and diameter. Good agreements were achieved between numerical and experimental results. On the other hand, there was a slight six to twelve percent deviation between the results achieved for the keyhole width, and this is attributable to several factors. Firstly, the material properties used in the simulation might not have been the same as the material properties presented in the experimental article. Secondly, the multiple reflections of the laser beam were neglected in the simulation. Hence, laser attenuation does not occur after each reflection, which keeps the laser density at a reasonable magnitude, leading to wider keyholes. Moreover, the metallic vapor in this paper was assumed to be transparent to the laser beam, and the plasma was also neglected. Together, these factors therefore affect the input energy arriving at the material surface, which is believed to be the main reason for the slight deviation between experimental and numerical results. Nevertheless, the present model successfully correlates with the experimental results in predicting the keyhole diameter on the

surface and the keyhole depth, in addition to offering acceptable magnitudes for the keyhole width.

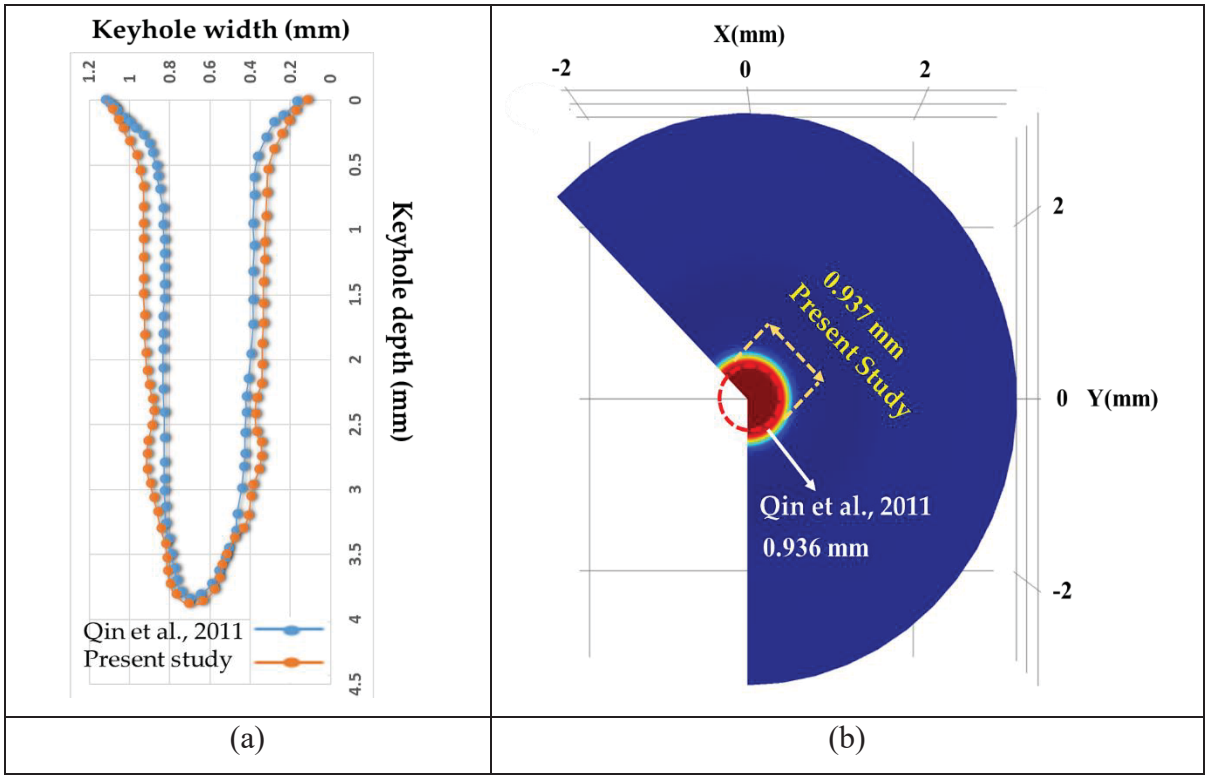

Figure 2.4 Comparison of (a) the keyhole morphology between the simulation (orange) and experimental (blue) results of Qin et al., (2011) and (b) the keyhole diameter on the surface Adapted from Qin et al., (2011)

2.4.2 Physical Phenomena in Laser Welding

Figures 2.5 and 2.6 depict the key aspects of the physical phenomena involved, such as the keyhole, molten pool, driving forces, pressures, mushy zone, and solidus/liquidus temperature lines. A series of driving forces, including the recoil pressure, buoyancy force, hydrodynamic and hydrostatic pressures, gravity, and surface tension effects (Marangoni and curvature effect), impose fluctuations of the keyhole and its propagation throughout the laser welding process. Figure 2.5 depicts the driving forces acting upon the keyhole and the molten pool. In this regard, the recoil pressure, which is colored green, aims to open the keyhole, while the hydrostatic pressure (brown) and surface tension forces (purple) try to collapse and close the keyhole (Chen et al., 2019). The buoyancy effect due to natural convection within the molten

pool and the gravity are specified in the figure in red and blue, respectively. The competition between these forces is the main reason for the keyhole instabilities, specifically for regions with higher temperature gradients, such as the liquid/vapor and solid/liquid interfaces. Moreover, the solidus/liquidus temperature contour line and the mushy zone (partially-molten material) are also visible in the picture.

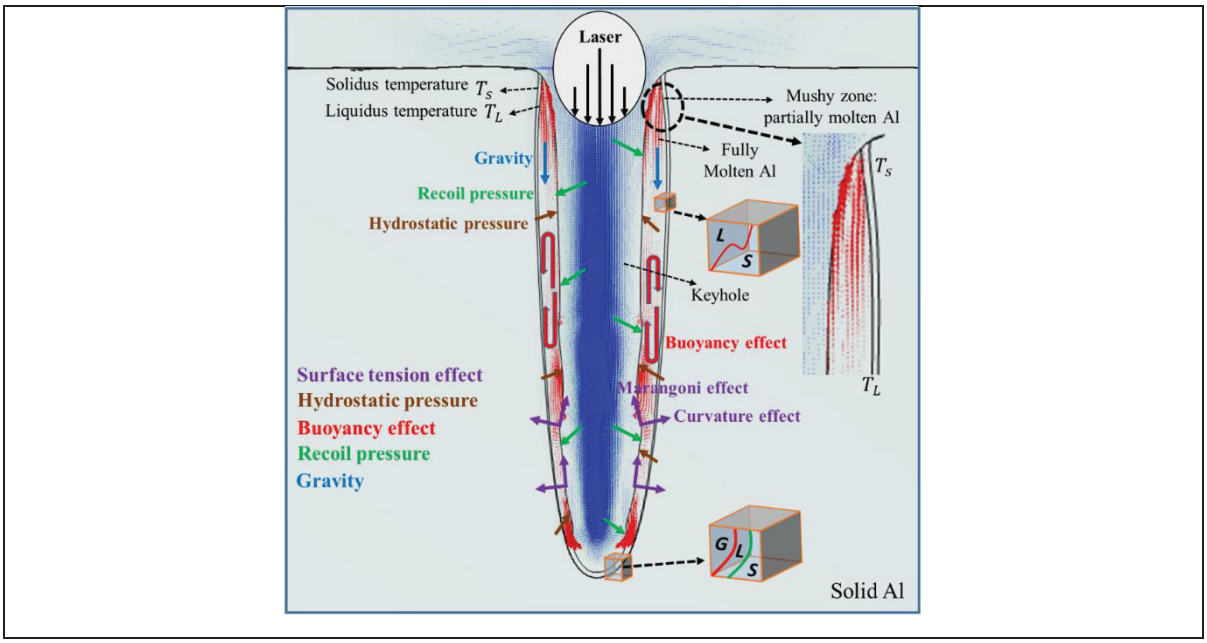

Figure 2.5 Schematic depiction of the keyhole, molten pool, driving forces and pressures, mushy zone, solidus, and liquidus temperature lines

Figure 2.6 presents the laser welding process stages in greater detail, using velocity contours in which black and white arrows indicate the material's flow direction in fluid 1 (keyhole and above the surface) and molten pool sections, respectively. Initially, the fusion begins when the laser is turned on, forming a solid/liquid interface as the temperature has not yet exceeded the vaporization threshold, which is evident within the first 30 µs. After 60 µs, the temperature rises above the vaporization point, forming a depression due to the recoil pressure following the localized vaporization. The pressure then pushes the liquid up and out of the keyhole, helping its penetration inside the material. This is corroborated by following the keyhole formation and propagation, as shown in the subsequent times after 60 µs of the process where the keyhole starts to form. As the keyhole penetrates deeper into the material, the temperature

gradients, surface tension effects, and other driving forces within the molten pool and keyhole intensify, leading to increased instabilities and fluctuations in the keyhole walls. These instabilities and fluctuations are more profound around the vapor/liquid interface, where the temperature gradients are amplified. This is observed after 3000 μs, where more arrows pile up around the fluctuating interfaces.

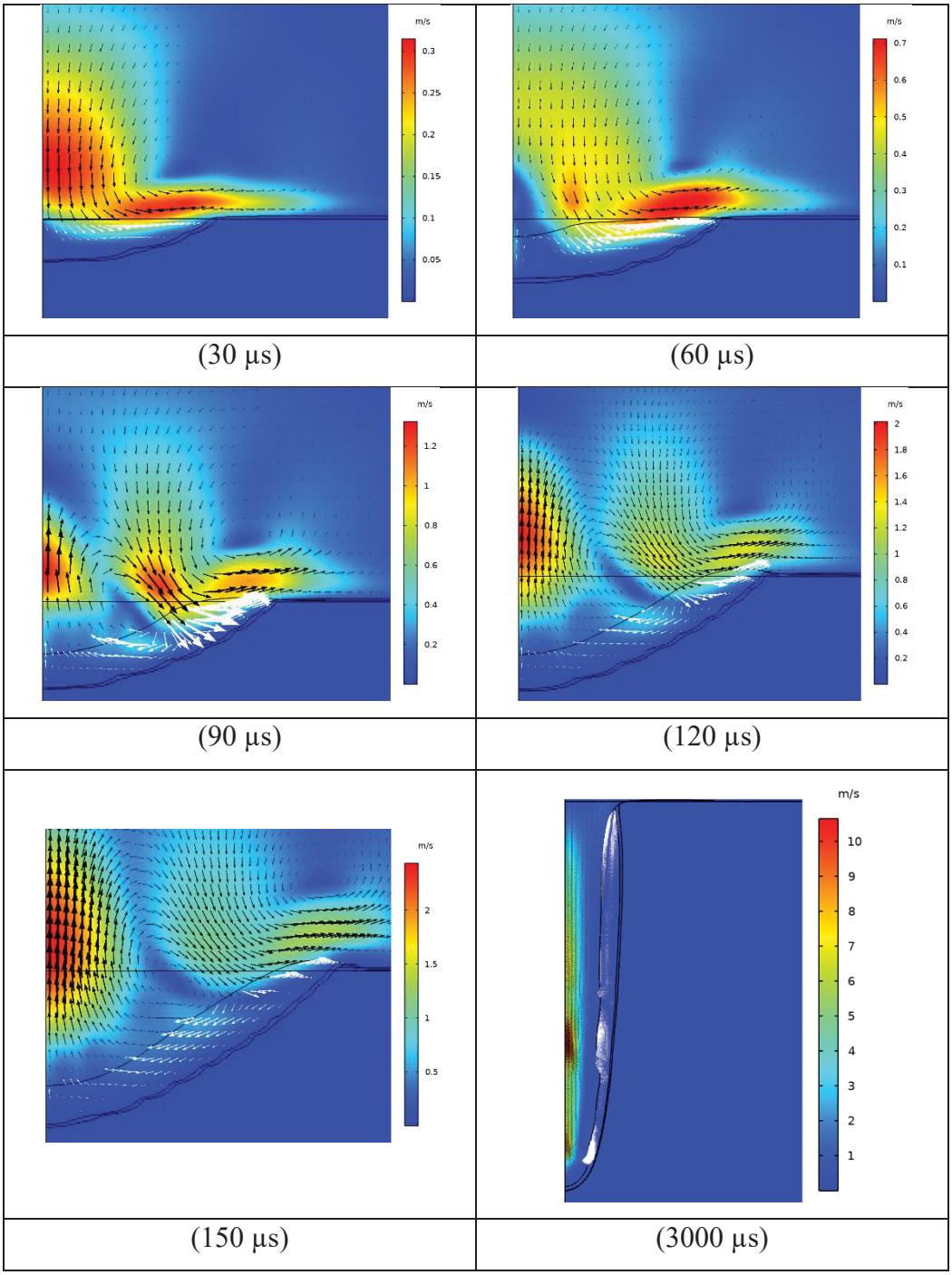

Figure 2.6 Keyhole penetration procedure for case LC10 with 6 kW laser power, 3 ms pulse width, and 300 μm spot radius

2.4.3 Analyzing the Impact of Laser Characteristics on the Morphology of the Keyhole

This section presents the impacts of the laser spot radius, laser frequency, and laser power on the keyhole penetration depth, and its propagation. Details of the laser characteristics used in this section are given for cases LC1 to LC10 in Table 2.2. For this section of the results, a rectangular pulse shape was employed for the laser density profile, as depicted in Figure 2.2 (a).

2.4.3.1 Effect of Spot Radius

This section examines the impact of the spot radius on the keyhole propagation and depth by analyzing four different spot radii under a constant laser power of 6 kW. Figure 2.7 illustrates the keyhole morphology for each spot radius during one pulse of laser welding. The results demonstrate that the more the spot radius is enhanced, the smaller the keyhole penetration depth becomes. It is observed that larger spot radii intensify the effect of the surface tension, reducing the tendency for laser penetration in the vertical direction while increasing it towards the sides. Consequently, smaller spot radii exhibit deeper keyholes. This behavior can be attributed to the fact that smaller spot radii concentrate the laser beam on a smaller area with a higher power, resulting in a faster temperature rise at the attack surface and quicker keyhole formation. The faster formation of the keyhole corresponds to the earlier dominance of the recoil pressure, which accelerates the keyhole propagation rate.

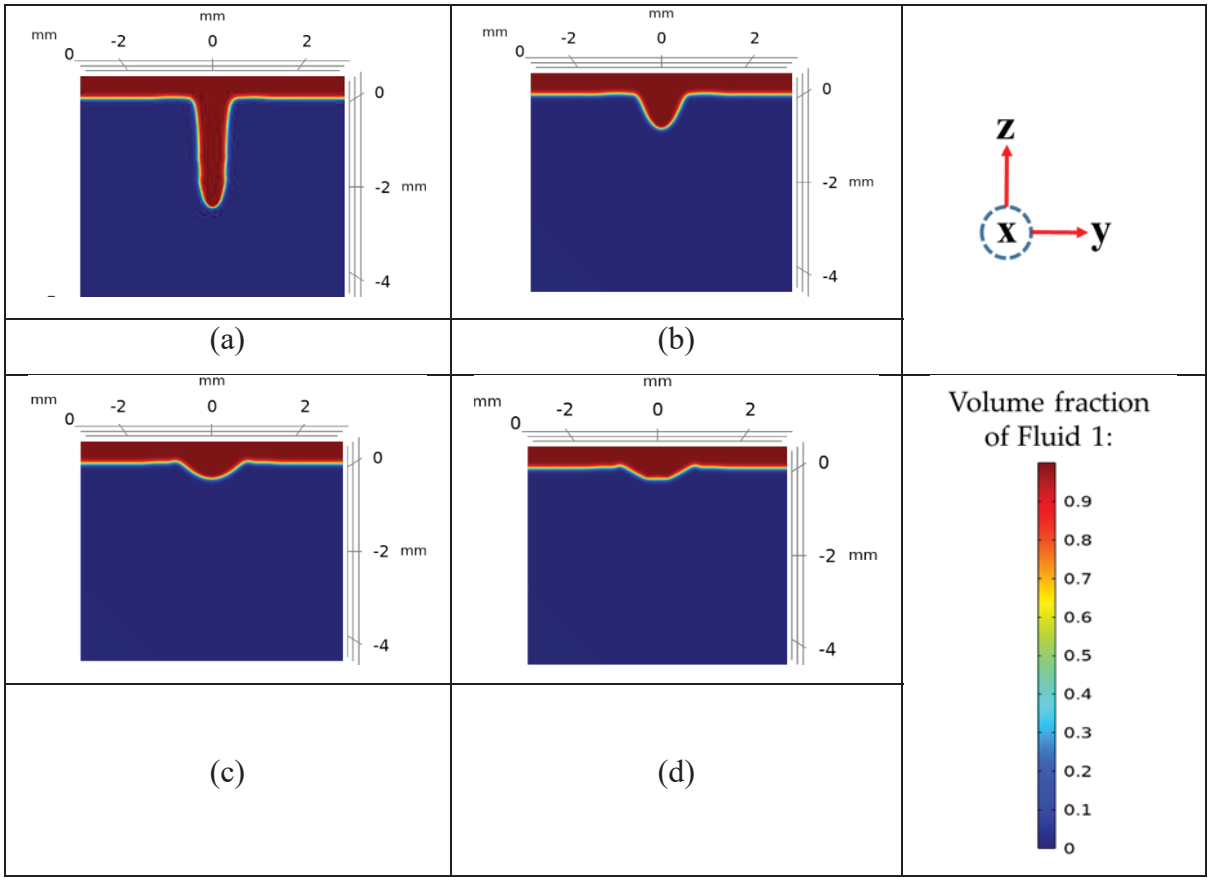

Figure 2.7 Morphology of keyhole for different spot radii after 2 ms of laser welding for (a) 300 µm spot radius, (b) 425 µm spot radius, (c) 525 µm spot radius, and (d) 725 µm spot radius

2.4.3.2 Impact of Laser Frequency

This section presents the impact of the laser frequency on the laser welding process through details given in Table 2.2 for cases LC5 to LC7. Simulations were conducted under 6 kW laser power using three laser rectangular pulses, with frequencies of 50 Hz, 100 Hz, and 150 Hz, to investigate their impact on the keyhole penetration depth and its propagation. A spot radius of 300 µm was chosen for this analysis due to its ability to achieve a deeper keyhole and a smoother surface melt ejection than with other spot radii. The pulse width is kept constant, while an increase in the laser frequency results in shorter pulse periods. Figure 2.8 illustrates that the keyhole penetration depth is gradually enhanced with higher laser frequencies. Notably, even though the total laser application time is shorter at 150 Hz than at 50 Hz, the

keyhole penetration depth is greater at 150 Hz. This characteristic may be advantageous for high-speed production systems. However, as depicted in Figures 2.8 and 2.9, higher laser frequencies lead to heightened keyhole instability and wall fluctuations. Figure 2.9 shows that at a laser frequency of 150 Hz, the keyhole becomes more unstable with steeper wall slopes after two pulse periods, enhancing the risk of sudden keyhole collapse and the formation of internal porosities.

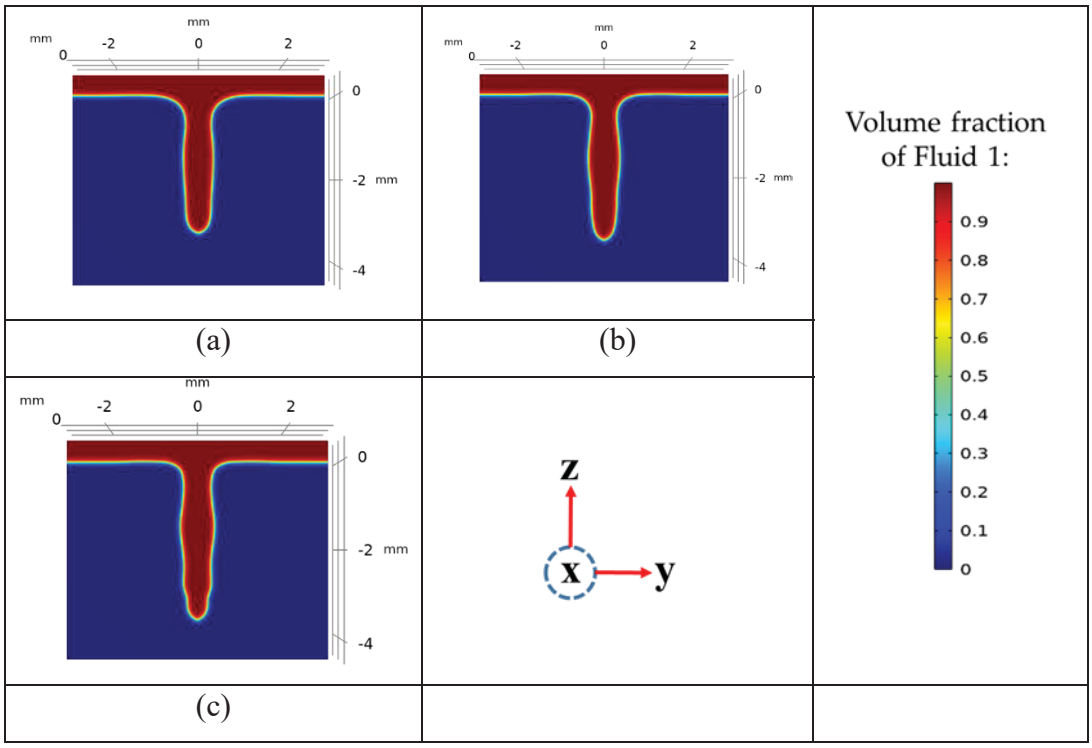

Figure 2.8 Morphology of keyhole for different laser frequencies after three pulses for (a) 50 Hz, (b) 100 Hz, and (c) 150 Hz

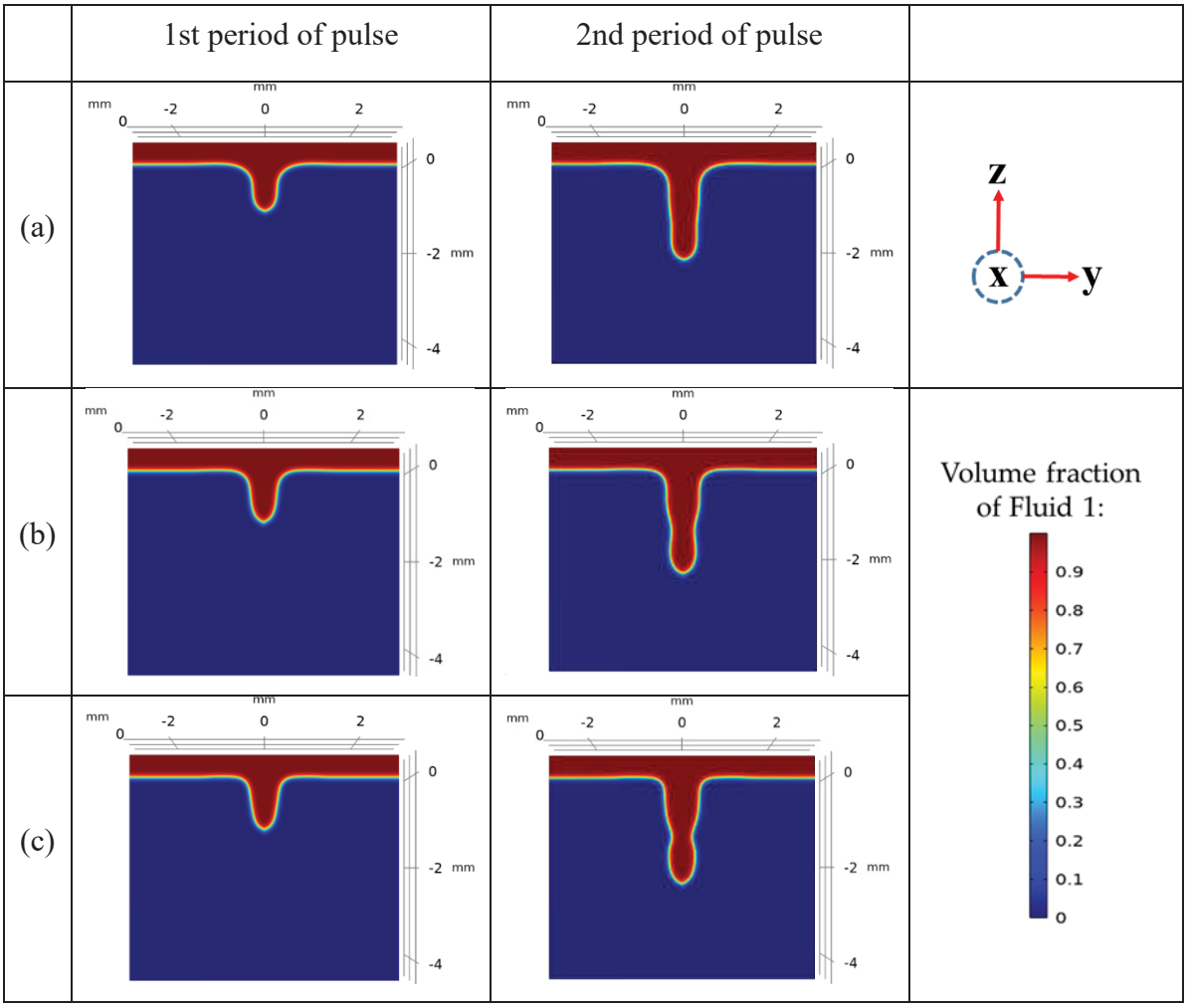

Figure 2.9 Morphology of keyhole for different laser frequencies at the end of the first and second pulse periods for (a) 50 Hz, (b) 100 Hz, and (c) 150 Hz

2.4.3.3 Impact of Laser Power

Based on the findings of the previous section for cases LC1 to LC7, a laser frequency of 100 Hz was selected as it offers a greater keyhole penetration depth than 50 Hz while exhibiting lower keyhole instabilities than 150 Hz. This section focuses on investigating the impact of the laser power on the keyhole penetration depth and instabilities under a constant frequency and pulse width during one laser welding pulse with a rectangular shape, as presented in greater detail in Table 2.2 for cases LC8 to LC10. Figure 2.10 illustrates a significant enhancement in keyhole penetration depth as the laser power is raised from 2 kW to 6 kW. This can be

attributed to the accelerated temperature rise at the material surface resulting from a higher laser power, which facilitates a faster keyhole formation and propagation, and ultimately leads to deeper keyhole penetration depths.

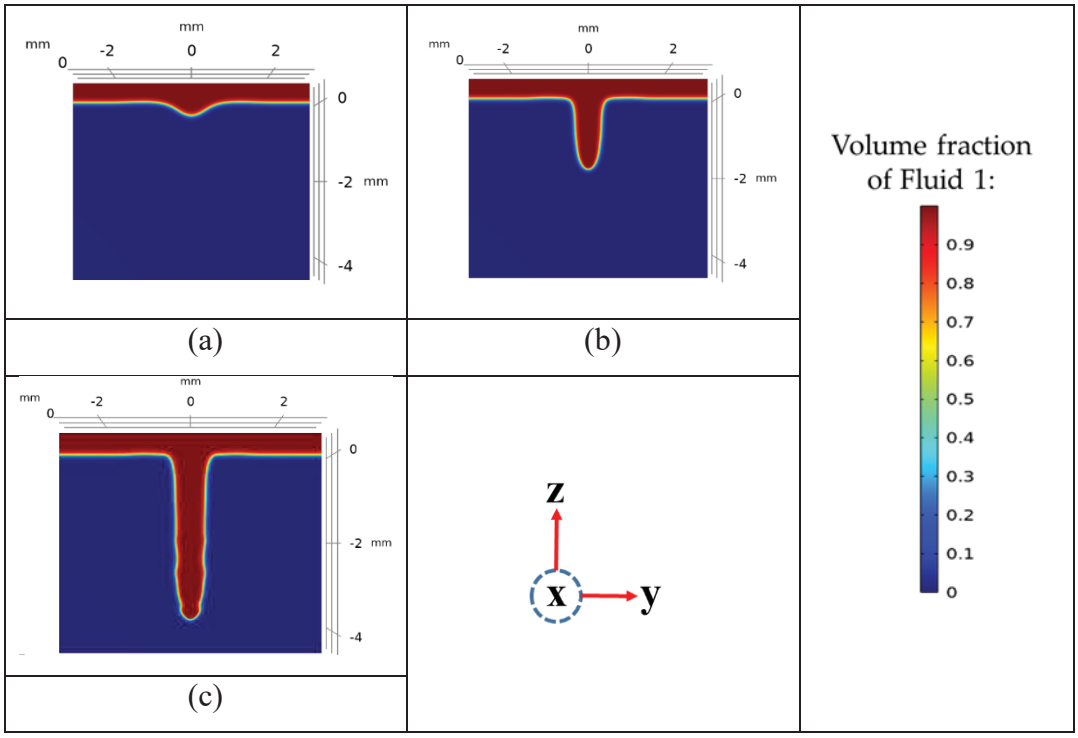

Figure 2.10 Morphology of keyhole for different laser powers after 3 ms for (**a**) 2 kW, (b) 4 kW, and (c) 6 kW

2.4.4 Analyzing the Impact of Modulated Wave Welding on the Morphology of the Keyhole

In this section, the impact of MW welding on keyhole propagation is investigated through the manipulation of pulse numbers, pulse width, and pulse shapes. Details of the laser characteristics used for this section are given for cases MW1 to MW17 in Table 2.2. The laser density profile employed for this section of the results uses various pulse shapes, as depicted in Figure 2.2.

2.4.4.1 Impact of Pulse Width

The effect of increasing the pulse width on the keyhole morphology is examined by using four different pulse widths (0.5 ms, 1 ms, 2 ms, and 3 ms) during one pulse of the laser with a rectangular shape, as specified for cases MW1 to MW4 in Table 2.2. Consistent with the previous sections, a laser peak power of 6 kW and a spot radius of 300 µm were chosen. Figure 2.11 illustrates that as the pulse width is increased, the keyhole penetration depth also improved. In fact, with higher pulse widths, the laser is irradiated on the surface over longer durations. Hence, the temperature rise in the material increases faster, leading to a faster keyhole initiation and propagation.

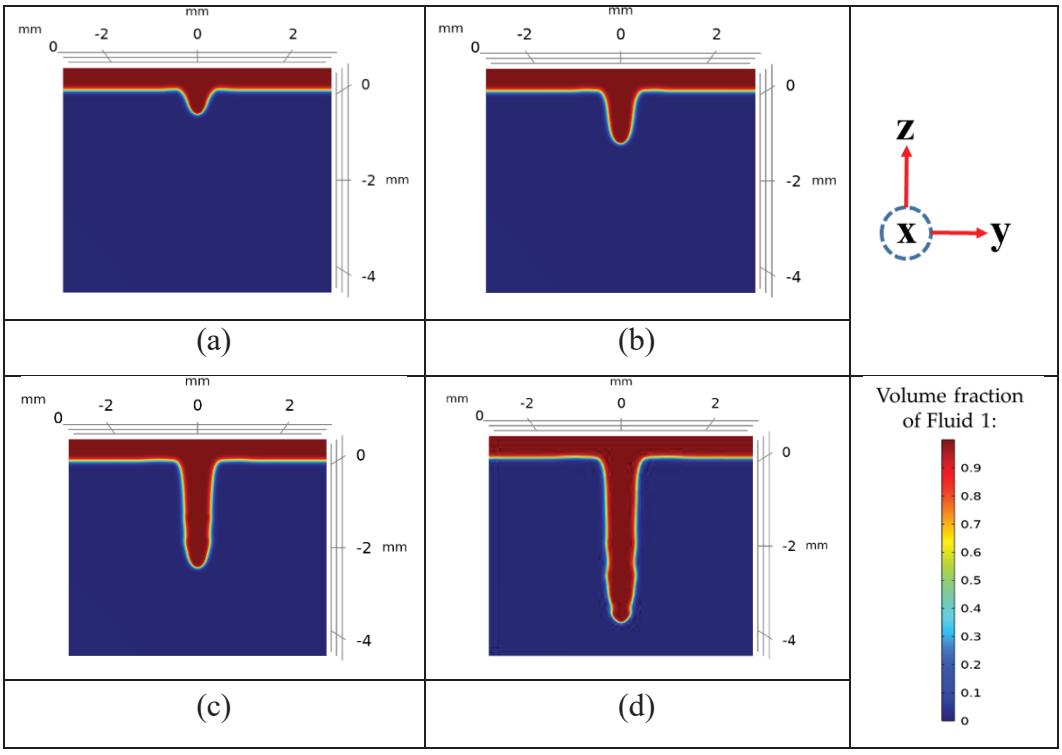

Figure 2.11 Morphology of the keyhole for different pulse widths of (a) 0.5 ms, (b) 1 ms, (c) 2 ms, and (d) 3 ms

2.4.4.2 Impact of Pulse Number

Here, the effects of different numbers (2, 6, 10, 14, and 18) of rectangular pulses over a period of 0.01 s of the laser welding process are compared. The details of the investigated cases (MW5 to MW9) for this parameter are given in Table 2.2. The number of pulses was increased while the total welding time and pulse width were held constant at 0.01 s and 0.5 ms, respectively. The laser power and frequency were also maintained at 4 kW and 100 Hz. As the number of pulses is enhanced, the period of each pulse is reduced, resulting in shorter intervals between laser pulses on the material surface. The keyhole morphology is then analyzed to understand the impact of the pulse number on the keyhole dynamics. Figure 2.12 demonstrates that increasing the pulse number leads to a greater keyhole penetration depth within the 0.01 s welding duration. This is due to the extended interaction time between the laser and the material. However, compared to single pulse cases with higher pulse widths, although the final keyhole shape at the end of each test has a wider and more curved shape, more fluctuations and instabilities are observed in the keyhole walls in the middle and initial regions of the penetration. This is due to the repeated on-and-off nature of the laser when using multiple pulses during the welding process. When the laser is turned off, the influence of the recoil pressure is significantly diminished, leading to a greater tendency for the keyhole to collapse. This is primarily driven by the effects of surface tension effect, hydrostatic and dynamic pressure, and other driving forces that contribute to closing the keyhole and causing fluctuations in the vapor/liquid interface. Hence, greater instabilities and wall fluctuations are observed when using multiple pulses through pulse number augmentation.

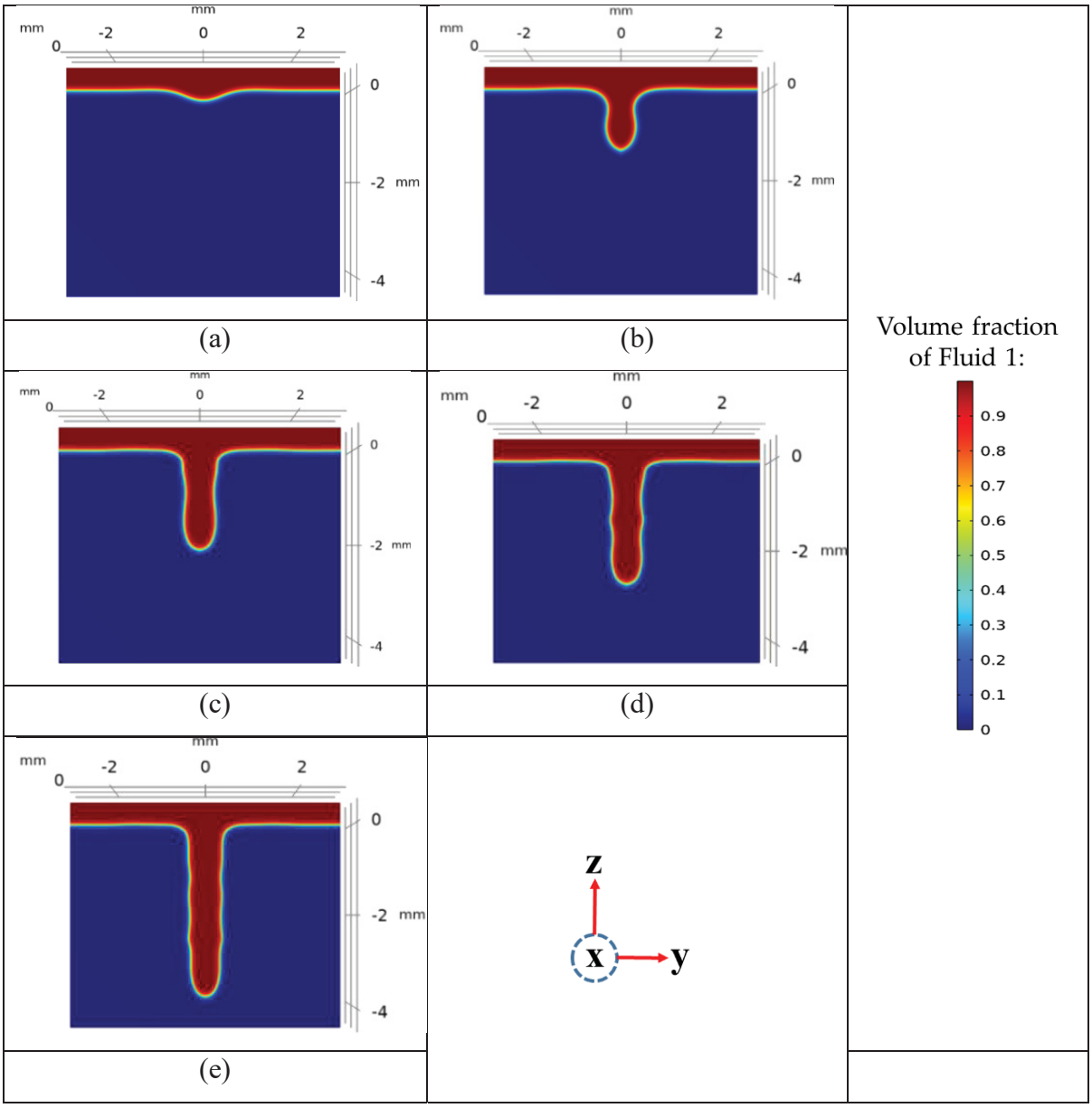

Figure 2.12 Morphology of the keyhole for different numbers of pulses: (a) 2 pulses, (b) 6 pulses, (c) 10 pulses, (d) 14 pulses, and (e) 18 pulses

2.4.4.3 Impact of Pulse Shape

In this section, the impact of power modulation is investigated for cases MW10 to MW17, using distinct pulse shapes, as depicted in Figure 2.2 and Table 2.2. A constant average laser energy of 20 J was applied for all cases, with a welding duration of 10 ms, to ensure

comparability. The results are compared with those of CW welding. Figure 2.13 shows the keyhole propagation morphology for different pulse shapes, including single-shape pulses (a–f) and multi-shape pulses (g–i). Among these, rectangular, trapezium (type 2 and type 1), and rectangular–triangular pulse shapes exhibit the highest keyhole penetration depths, 2.65 mm, 2.42 mm, 2.37 mm, and 2.13 mm, respectively. Rectangular–rectangular, variant–rectangular, and rectangular–trapezium pulse shapes offer intermediate depths of 1.9, 1.85, and 1.77 mm, respectively. CW welding demonstrates the lowest penetration depth of 1.51 mm, along with a smaller surface hole diameter. Notably, the variant–rectangular pulse shape produces a more stable and cylindrical keyhole, with a smaller keyhole depth/width ratio than other pulse shapes.

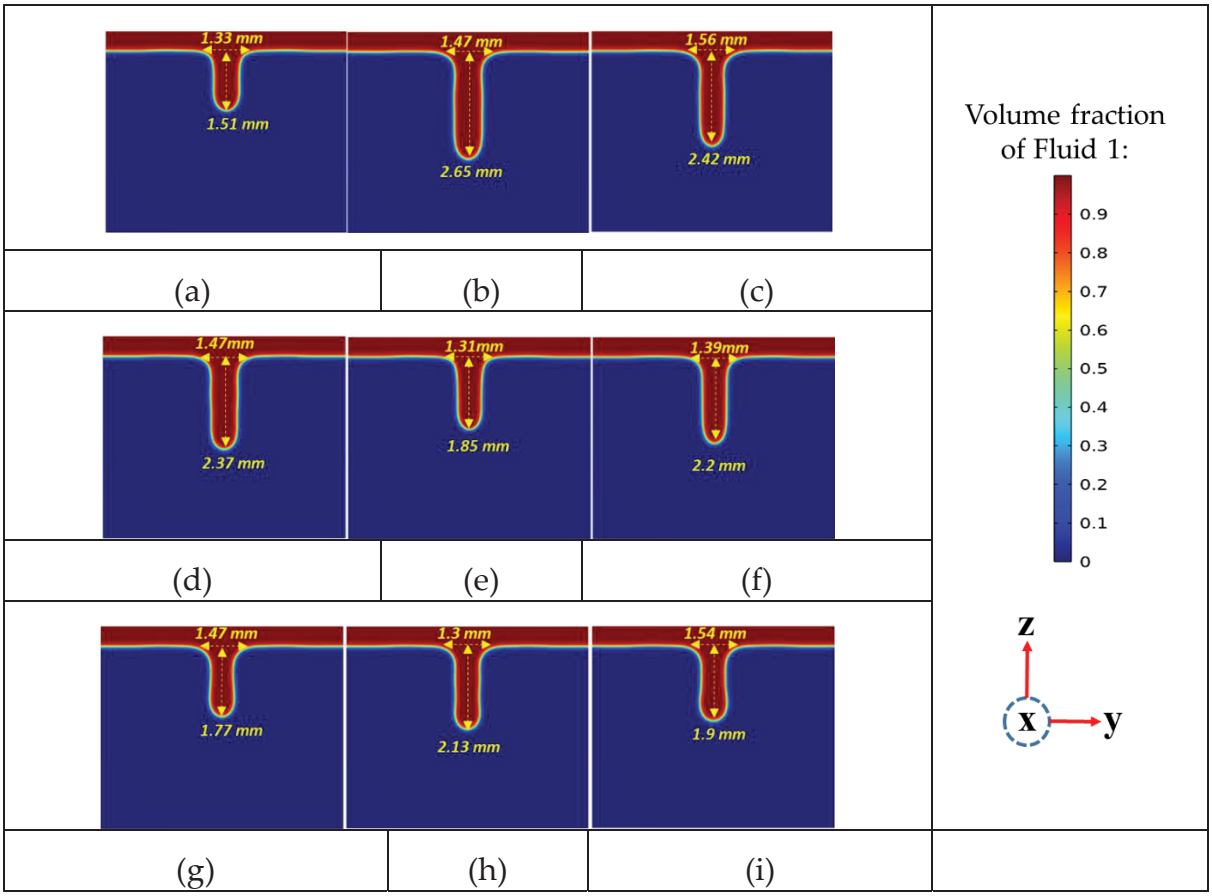

Figure 2.13 Morphology of keyhole for different pulse shapes, including (a) continuous welding, (b) rectangular pulse welding, (c) trapezium type 2, (d) trapezium type 1, (e) variant–rectangular, (f) triangular pulse welding, (g) rectangular–trapezium, (h) rectangular–triangular, and (i) rectangular–rectangular (rectangular)

2.4.5 Temperature Variations within the Base Metal

This section focuses on measuring and comparing the maximum temperatures within the base metal to gain insights into temperature variations in the laser welding process.

Figures 2.14–2.16 depict the maximum temperature variations within the different base metal cases. Figure 2.14 (a)–(c) displays the temperature variations, considering distinct spot radii, laser frequencies, and laser power, respectively. Figure 2.14(a) shows that the incidence of the laser beam on the material surface causes a sudden temperature increase, triggering a fusion phase change as the temperature exceeds the melting temperature. Subsequently, the temperature reaches approximately 2743 K, which is the vaporization threshold, and vaporization becomes an additional phase change added to the process alongside fusion. During a single pulse, the temperature changes smoothly upon reaching the vaporization point, reflecting dominant latent heat transfer and leading to a nearly constant temperature throughout the phase transition. After 2 ms (1 pulse), the laser shuts down, resulting in a drop in the maximum temperature within the base metal. The material begins to cool down until it reaches the solidification temperature, indicated by a dashed circle, leading to the solidification phase change. The temperature then decreases smoothly throughout the solidification process since the material loses its heat in a latent heat form. Further away from the solidification temperature interval, the material experiences steeper temperature drops as heat is lost in a sensible form until it reaches a stable temperature almost equal to ambient. Figure 2.14 (a) also shows that the temperature reaches its vaporization point faster for smaller spot radii (LC1). This leads to faster keyhole formation, resulting in faster and deeper penetration depths, as corroborated in Figure 2.7. In Figure 2.14 (b), the impact of different laser frequencies on temperature variations is examined using three pulses with reduced pulse periods, revealing similar trends for temperature variation as observed in Figure 2.14 (a). For a laser frequency of 50 Hz, the maximum temperature diminishes considerably after one pulse, reaching temperatures close to ambient. In contrast, frequencies of 150 Hz and 100 Hz exhibit higher temperatures at the end of the first pulses. This difference is attributable to the longer pulse periods in these cases, which allow the material to cool down more between each pulse. Another noteworthy feature, indicated by different line arrows in Figure 2.14 (b), is the gradual increase in maximum

temperature within the domain after each consecutive pulse. This is attributed to the overall temperature escalation in the base metal as the number of pulses increases. The phenomenon is more pronounced at 150 Hz due to its shorter pulse period, which limits the cooling of the material between pulses. Figure 2.14(c) shows that higher laser powers accelerate keyhole formation and propagation by allowing to reach the vaporization threshold faster. Moreover, the solidification process is prolonged at higher powers due to increased fusion throughout the material.

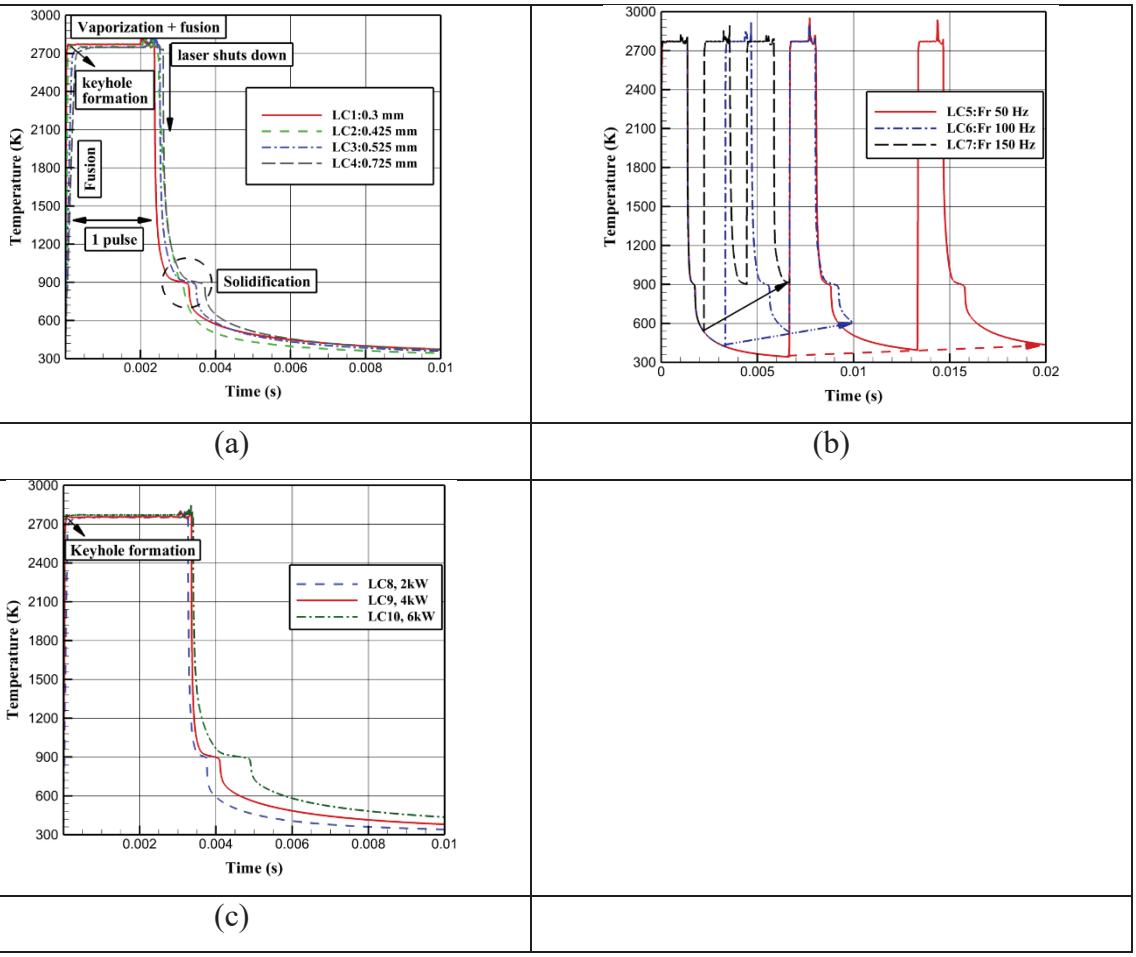

Figure 2.14 Maximum temperature variations within Domain 2, considering different (a) laser spot radii, (b) laser frequencies, and (c) laser powers

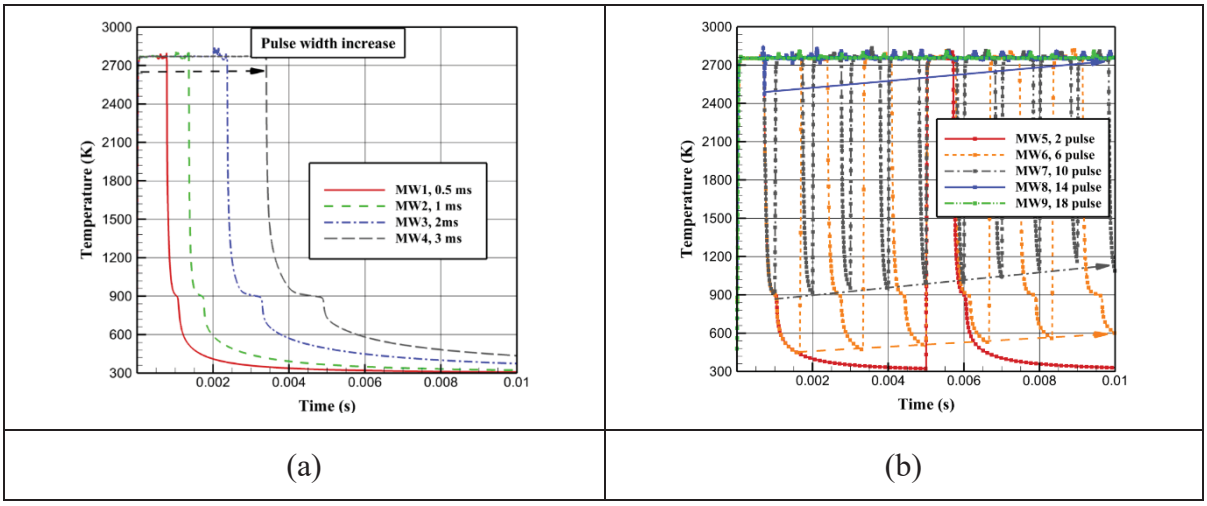

(a) (b)

Figure 2.15 Maximum temperature variations within Domain 2, considering different (a) pulse widths and (b) pulse numbers

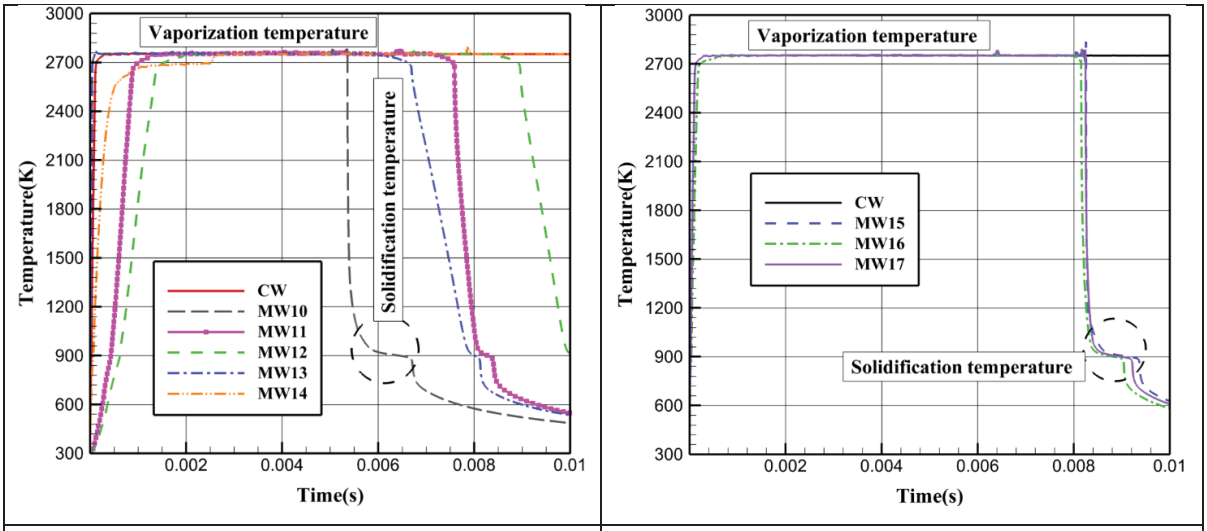

(a) (b)

Figure 2.16 Maximum temperature variations within Domain 2, considering different pulse shapes, compared to CW for (a) MW10-14 and (b) MW15-1

Figure 2.15 (a), and (b) depict the maximum temperature change for different pulse widths and pulse numbers. Figure 2.15 (a) shows the maximum temperature variation, while the pulse width enhanced from 0.5 ms to 3 ms. It is seen that longer solidification periods are observed as the pulse width increases. This might lead to higher keyhole fluctuations due to the impact of solidification on the interfaces, intensifying the surface tension effect. Moreover, with an

extended pulse width, the vaporization process is prolonged, resulting in deeper keyholes, as corroborated in Figure 2.11. Another visible feature from Figure 2.15 (a) is that for greater pulse widths, the final temperature of the material at the end of one pulse period is higher. This is due to the overall intensification in the material temperature thanks to more extended laser/material interactions induced by longer pulse widths. Figure 2.15 (b) illustrates the impact of an increase in the number of pulses through a fixed welding duration of 0.01 s. As can be seen, the more the pulse number is raised, the more the period of pulses is reduced. Hence, the material loses its chance to cool down significantly between pulses. Therefore, as the number of pulses enhances, the maximum temperature at the end of each pulse period is increased, up to the point where no reasonable temperature loss is seen between pulses, as shown for case MW9, which applies 18 pulses. The temperature variations are then similar to what is observed in continuous wave laser welding.

Figure 2.16 (a), and (b) depict the impact of various pulse shapes on the variations in maximum temperature within the base metal. Figure 2.16 (a) reveals that for continuous wave welding and the variant–rectangular pulse shape with ascending rectangular steps, the maximum temperature variations are approximately the same after the vaporization point is reached. There are descending temperature variations for MW10, MW13, MW11, and MW12, which correspond to rectangular, trapezium (type two/one), and triangular pulse shapes, respectively. This is due to a gradual power mitigation from 4 kW to 0 at the end of their pulse widths, 5 ms, 8 ms, 8 ms, and 10 ms, respectively. The temperature drop when using a rectangular pulse shape (MW10) is faster at the end of one pulse as it experiences a sudden power drop from 4 kW to 0. On the other hand, for trapezium (type 1: MW11 and type 2: MW13) and triangular pulse shapes (MW12), the temperature drops with smaller slopes since the laser power is decreased less rapidly but rather gradually than what is observed for MW10. There are no significant differences in the maximum temperature variations within the material when using multi-shape pulses, as can be seen in Figure 2.16 (b).

2.5 Conclusion

This paper presents a novel numerical approach utilizing COMSOL Multiphysics to simulate pulsed and continuous laser welding of aluminum in a 2D axisymmetric configuration. The study investigates the effects of laser parameters such as the spot radius, laser power, and laser frequency on keyhole penetration depth, propagation, and instabilities. Moreover, the impact of power wave modulation is also examined on keyhole dynamics through variations in the pulse width, pulse number, and pulse shape. The results are compared with continuous welding, and the following findings are observed.

- The more the spot radius is enhanced, the smaller the keyhole penetration depth, and the more intense the melt ejection. A reduction of over 80% in the keyhole penetration depth is observed with an increase in the spot radius.
- As the laser frequency increases, the keyhole wall instabilities and the tendency of the keyhole to collapse are amplified while the keyhole penetration depth is increased to some extent.
- With an increase in laser power from 2 kW to 6 kW, the keyhole penetration depth is improved by more than 80%.
- Extending the pulse width from 0.5 ms to 3 ms leads to an increase of over 80% in the keyhole penetration depth. Moreover, the keyhole wall becomes more unstable as pulse width is extended.
- If the welding duration is maintained at 0.01 s, the keyhole penetration depth increases significantly when using higher pulse numbers. However, more keyhole fluctuations and instabilities are observed due to multiple laser on-and-offs.
- The rectangular pulse shape has the greatest keyhole penetration depth among various pulse shapes, while variant–rectangular pulse shapes and triangular pulse shapes produce more keyhole stability with smaller depth/width ratios.

- At the end of the welding process, higher temperatures within the base metal, achieved during CW laser welding, do not necessarily correspond to deeper keyholes and welding efficiency.

CHAPTER 3

TOWARD STABILIZING THE KEYHOLE IN LASER SPOT WELDING OF ALUMINUM: NUMERICAL ANALYSIS

Saeid SaediArdahaei and Xuan-Tan Pham [a]

[a] Department of Mechanical Engineering, École de Technologie Supérieure, 1100, Notre-Dame West, Montreal, Quebec, Canada H3C 1K3

Paper published in *Materials*[2], September 2024

Abstract

The inherent instability of laser welding, particularly keyhole instability, poses significant challenges in industrial applications, leading to defects such as porosities that compromise weld quality. Various forces act on the keyhole and molten pool during laser welding, influencing process stability. These forces are categorized into those promoting keyhole opening and penetration (e.g., recoil pressure) and those promoting keyhole collapse (e.g., surface tension, Darcy's damping forces), increasing instability and defect likelihood. This paper provides a comprehensive instability analysis to uncover key factors affecting keyhole and process instability, presenting future avenues for improving laser welding stability. Using a novel numerical method for simulating laser spot welding on aluminum with COMSOL Multiphysics 5.6, we investigated the effect of laser pulse shaping on keyhole and process instability. Our analysis focused on keyhole morphology, fluid flow behaviour, and force analysis. The results indicated that the curvature effect, Marangoni effect, and Darcy's damping force are primary contributors to instability, with the curvature effect and Darcy's damping force being the most dominant. Additionally, erratic and high-velocity magnitudes induce intense fluid flow behaviour, exacerbating keyhole instability. Moreover, single/quadruple peak triangular and variant rectangular ramp-down pulse shapes produced the least instability, while multi-pulse rectangular shapes exhibited intense instability. It was found that combining triangular/rectangular pulse shapes can reduce force and keyhole instability by

[2] Material 2024, 17(19), 4741

smoothing spontaneous force spikes, resulting in a more stabilized welding process. Controlling fluid flow and abrupt force changes with appropriate pulse shaping is key to defect-free welded products.

Keywords: Keyhole; instability analysis; velocity; curvature effect; Marangoni effect; Darcy's damping force

3.1 Introduction

Laser welding is widely employed in automobile and aerospace manufacturing due to its ability to deeply penetrate materials, particularly aluminum alloys, which possess reliable characteristics such as lightweight, good corrosion resistance, and high strength as highlighted by (Miller et al., 2000), (L. Wang et al., 2023), and (Schubert et al., 2001), just to name a few. The fundamental processes occurring during laser–material interaction in high-energy-density laser processing encompass a range of intricate physical phenomena. These include dynamics related to surface tension, the generation of recoil pressure from vaporization, the formation of vapour plumes, attenuation and scattering of the laser beam by condensed plume materials, phase transitions such as melting, solidification, and vaporization, thermo-capillary driven flows (Marangoni convection and curvature effects), flow induced by recoil pressure, multiple reflections of the incident laser beam, and high-speed rates of heating and cooling (Aggarwal et al., 2024; Courtois et al., 2013; Tan & Shin, 2014). During laser welding, a high-intensity laser beam creates a 'keyhole' by heating the material above its vaporization point. This causes vaporization and mass loss, forming a hole. The resulting vapour pressure, or recoil pressure, helps penetrate the material and keep the keyhole open (Lee et al., 2002). Keyhole formation and stability throughout the laser welding process are influenced by various forces, including recoil pressure, surface tension (Marangoni and curvature effects), buoyancy, hydrostatic pressures, and gravity. These forces cause fluctuations in the keyhole and affect its propagation. Among them, recoil pressure and surface tension emerge as dominant factors, with recoil pressure opening the keyhole and surface tension attempting to close it (Chen et al., 2019). D. Schauer et al. emphasized the importance of surface tension and recoil pressure

on the keyhole wall. They identified a critical equilibrium point where these forces balance each other. Below this point, recoil pressure dominates, while above it, surface tension prevails. When surface tension becomes dominant, keyhole stability is compromised, potentially leading to collapse (Schauer, 1977). Figure 3.1 illustrates a schematic 3D depiction of laser welding, showing how the process instability causes periodic keyhole openings and collapses, as reported by (Jiang et al., 2019) and (Y.-X. Zhang et al., 2017). Understanding this dynamic behaviour and fluctuations in the keyhole, along with the inherent instability in laser welding, has constrained its widespread adoption within the industrial manufacturing sector, as noted by (You et al., 2015). Instabilities in laser welding, particularly with aluminum, lead to defects such as porosities (L. Wang et al., 2023), humps (Bunaziv et al., 2020), spatters (Wu et al., 2017), and other imperfections, significantly undermining the reliability of manufactured products. Most defects in laser welding of aluminum and its alloys mainly arise from aluminum's material properties (L. Huang et al., 2018), its rapid solidification rate (L. Huang et al., 2018), process-related instability (You et al., 2015), and high reflectivity (Ready, 1997). Zhang et al. (D. Zhang et al., 2018) found that instability in the process directly leads to defect formation and You et al. (You et al., 2015) highlighted that keyhole instability causes bubble formation in aluminum alloys. Huang et al. (L. Huang et al., 2018) noted that the rapid solidification rates of molten aluminum trap bubbles at the solidification front, resulting in porosities. Therefore, controlling fluctuations in the keyhole and melt pool is crucial for process stability and aluminum welding quality, as keyhole instabilities are a common cause of porosity, as emphasized by Lin et al. (Lin et al., 2017). A variety of experimental methods were employed in scholarly research to understand the laser welding process. Techniques included ex situ X-ray tomography for porosity analysis (Panwisawas et al., 2017), in situ high-speed imaging of the melt pool (Y. Huang et al., 2019) and vapour plume (Mohanta et al., 2020), and synchrotron-based X-ray imaging to observe melt pool dynamics and keyhole formation (Cunningham et al., 2019). These setups are often costly and complex, with some facing limitations in spatial or temporal resolution, hindering detailed observation of rapid phenomena. In addition, obtaining high-quality welds in high thermal conductivity materials or volatile elements, like aluminum and certain alloys (e.g., 5000 or 7000 series), frequently depends on a trial and error approach. The narrow welding parameter window for these

materials further complicates experimentation, as keyhole and weld pool behaviour exhibit erratic fluctuations (Pang et al., 2015). Hence, experimentation might fail to reliably identify the causes of keyhole instability, dominant forces, and fluid flow behaviour contributing to process instability and defect formation. Numerical simulations alternatively offer significant advantages over experimental methods for modelling and understanding keyhole dynamics and instabilities, providing a more efficient and cost-effective solution (Duggirala et al., 2021). Pulsed wave (PW) lasers are ideal for welding aluminum and its alloys, as they effectively overcome aluminum's reflectivity by providing high energy density at the start of the pulse while regulating the average power to reduce overall heat (Cavilha Neto et al., 2021; Hajavifard et al., 2016). Wang et al. (X. Wang et al., 2022) noted that using pulse wave modulation (PWM) in laser beams enhances welding stability. By adjusting laser characteristics like frequency, amplitude, and power, the size and stirring intensity of the molten pool can be effectively controlled. Matasunawa et al. (Matsunawa et al., 1998) conducted an extensive study on the dynamics of the molten pool and the keyhole, revealing that PWM significantly reduces porosity formation. They attributed this reduction to the efficient elimination of holes from the preceding pulse by the subsequent pulse, given an appropriate overlapping ratio. In another paper, Tsukamoto et al. (Tsukamoto et al., n.d.) confirmed that modulating laser power in pulses effectively stabilizes the keyhole and reduces porosity, particularly when the modulation frequency aligns with the natural oscillation frequency of the molten pool. Moreover, Heider et al. (Heider et al., 2015) studied power modulation when performing laser welding on copper, demonstrating that modulating power and frequency effectively reduced weld defects and increased penetration depth by up to 30%. Volpp et al. (Volpp & Vollertsen, 2019) also investigated methods to improve the Gaussian beam welding stability and discovered that the laser beam shaping helps keep the keyhole open, preventing its collapse. This highlights the importance of modifying the laser beam shape to ensure welding stability. However, these studies did not provide information on the dominant forces causing instability and defects, nor did they address how modulating laser power affected these forces. To evaluate the effect of laser pulse modulation on the stability of keyhole mode laser welding, numerical models must account for fluid flow dynamics in the melting pool and accurately capture the dynamic evolution of the keyhole, considering heat transfer, fluid motion, and

phase transitions. Scientists employed various modelling approaches to address these factors in their simulations. Pang et al. (Pang et al., 2014) employed the Level Set (LS) method to simulate keyhole formation and investigated the mechanisms of keyhole instability with varying heat inputs. Courtois et al. (Courtois et al., 2013) proposed a detailed laser welding model utilizing the LS method to trace the vapour/liquid interface, encompassing all metal phases. However, using a higher laser wavelength than typical industrial standards raises concerns about its practicality. Moraitis et al. (Moraitis & Labeas, 2008) employed the Finite Element Method (FEM) to develop a localized model that predicts keyhole morphology according to temperature profile. The model was based on solid mechanics and excluded fluid convection or the evolution of the free surface. Previous studies primarily focused on reducing defects through various operational and laser parameters but often lacked detailed explanations of the forces and fluid flow behaviours causing instabilities, both quantitatively and conceptually. Furthermore, the impact of pulse modulation on these instabilities and defect reduction was not thoroughly explored. While several studies have explored defect reduction and laser welding in other materials, a significant gap remains in understanding how advanced pulse modulation techniques, particularly non-rectangular and combined pulse shapes, can be used to control keyhole instabilities in aluminum. This research uniquely addresses this gap by offering both quantitative and conceptual new insights that have the potential to optimize laser welding processes and enhance industrial applications in fields such as automotive and aerospace manufacturing. Understanding these aspects is crucial for comprehending how laser–material interactions, molten pool dynamics, and keyhole behaviour contribute to instability, and how these factors can be controlled. Most research concentrated on rectangular pulse shapes and materials like steel and copper, with limited theoretical studies on aluminum. The present study addresses the gap in conducting pulse shaping in keyhole mode laser spot welding on aluminum using various triangular, variant rectangular pulse shapes, and their combinations. The aim was to investigate how pulse shaping can be used to control keyhole instability and improve process stability, and to assess the sensibility of instability on these pulse shapes. A quantitative analysis of instability-inducing forces, fluid flow behaviour, and keyhole morphology was conducted to analyze the instability. This study employed a novel numerical model using modified techniques, including a modified mixture theory, a modified

LS method, and the enthalpy–porosity technique, to investigate phase transformations and coupled physics in a 2D axisymmetric configuration. The modified mixture theory was applied comprehensively across liquid, solid, and gas phases, while the modified LS method tracked the vapour/liquid interface and included evaporation effects throughout the laser welding process. The enthalpy–porosity technique enhanced the model's capability to accurately capture phase transformations and fluid flow dynamics.

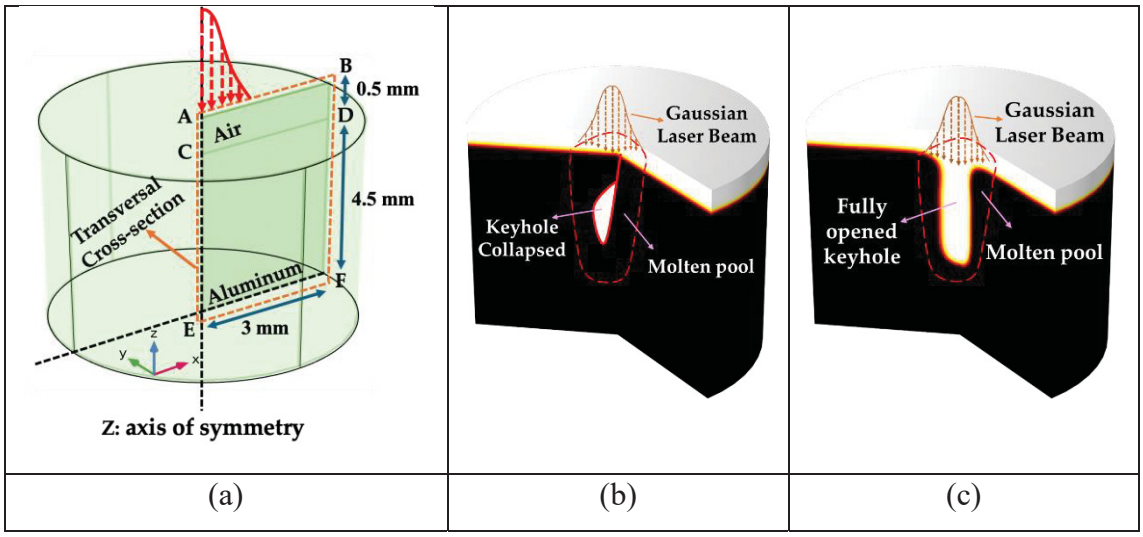

Figure 3.1 Schematic 3D representation of (a) the 2D axisymmetric laser welding setup with Gaussian beam profile, (b) laser-based welding process with keyhole collapse (closed keyhole) induced by instabilities, and (c) laser-based welding process with keyhole stability (open keyhole)

3.2 Materials and Methods

This research developed a 2D axisymmetric model of laser spot welding on aluminum to investigate the impact of pulse shaping on keyhole stability and process instabilities. This study analyzed triangular and rectangular pulse shapes and their combinations to improve efficiency and understand the forces and fluid behaviours causing instabilities. The choice of these particular pulse shapes was made based on their potential to reduce instabilities and defects in keyhole mode laser welding, as suggested by preliminary studies (SaediArdahaei & Pham, 2024a). These shapes were chosen to explore the full spectrum of their effects on keyhole instabilities and fluid dynamics through a thorough instability analysis.

The goal was to control and reduce these instabilities for defect-free weldments. Case studies based on various pulse shaping trends are detailed in Table 3.1 and Figure 3.2.

Table 3.1 Corresponding details of the case studies

Case No.	Laser Power	Pulse Width	Total Laser Energy	Number of Pulses	Pulse Shape	Total on Time
1	2 kW	10 ms	20 J	1	Continuous	10 ms
2	4 kW	5 ms	20 J	1	Rectangular constant	5 ms
3	1-3 kW	2.5 ms	20 J	1	Rectangular: ramp up–ramp down	10 ms
4	0.5-4 kW	2.5 ms	20 J	1	Rectangular: ramp down	10 ms
5	1-3 kW	2 ms	20 J	1	Rectangular: ramp down	10 ms
6	1-3 kW	2 ms	20 J	1	Rectangular: ramp up	10 ms
7	1.5-3 kW	2 ms	20 J	1	Rectangular: ramp down-up-down	10 ms
8	0-4 kW	10 ms	20 J	1	Triangular: single peaks	10 ms
9	0-4 kW	5 ms	20 J	2	Triangular: double peaks	10 ms
10	0-4 kW	2.5 ms	20 J	4	Triangular: quadruple peaks	10 ms
11	0-4 kW	1.25 ms	20 J	8	Triangular: octuple peaks	10 ms
12	0-6 kW	1 ms	18 J	3	Rectangular	3 ms
13	0-6 kW	2 ms	18 J	3	Triangular	6 ms
14	0-6 kW	1-2 ms	18 J	3	Rectangular–triangular	4 ms
15	0-6 kW	2 ms	18 J	3	Triangular–rectangular	6 ms

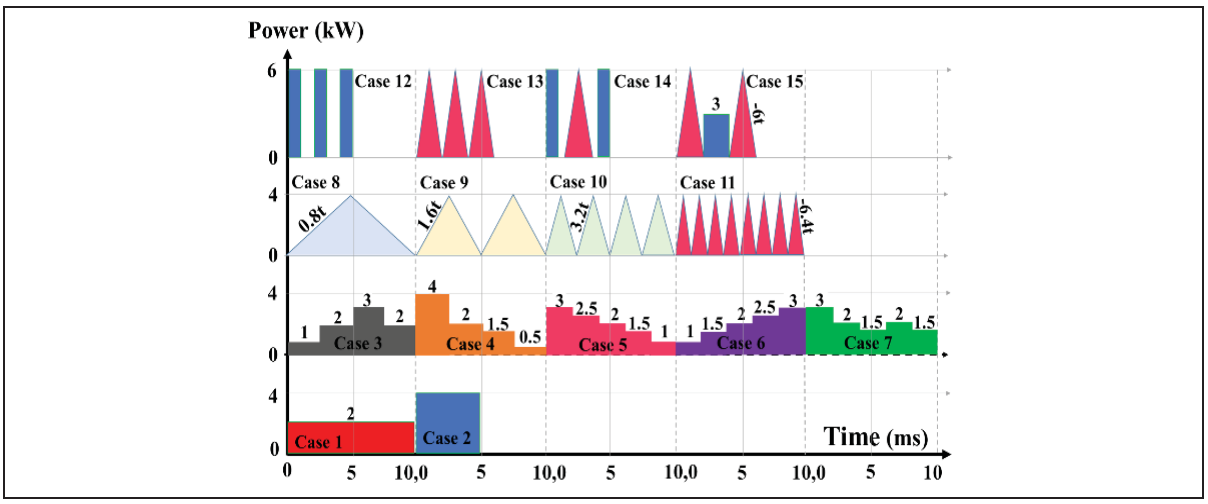

Figure 3.2 Full schematic illustrating the pulse shapes implemented for pulse modulation

3.2.1 Model Geometrics, Material, and Laser Heat Source

All simulations and generation of the results were conducted using the COMSOL Multiphysics 5.6 graphical user interface. The software allows an immediate transition from a 2D axisymmetric model to a 3D model and imposes symmetry conditions for axisymmetric assumptions. Aluminum, with dimensions of 4.5 mm (height) × 3 mm (width), was chosen as the base metal, with its thermophysical properties listed in Table 3.2. Aluminum was selected as the base material due to its widespread use in industrial applications, particularly in the automotive and aerospace industries. Its high thermal conductivity, reflectivity, and challenging weldability make it an ideal candidate for studying the effects of pulse modulation on keyhole stability and understanding the underlying reasons behind keyhole instability through sensibility analysis. A Gaussian laser distribution represented the heat source for stationary laser welding. The 3D schematic of the simulated 2D axisymmetric configuration is shown in Figure 3.1. This model was used because stationary spot laser welding keeps the laser beam fixed, ensuring rotational symmetry about the vertical z-axis as shown in Figure 3.1(a). This assumption was necessary to validate the numerical model and provided a robust foundation for future enhancements, facilitating the transition to more complex setups, including moving lasers and ensuring alignment with industrial applications.

Table 3.2 Thermal and physical characteristics of aluminum
Adapted from Mills et al., (2002), Cho et al., (2018), Zhang et al., (2014)

Property	Symbol	Magnitude
Solidus temperature	T_s	847 (K)
Liquidus temperature	T_l	905 (K)
Vaporization temperature	T_V	2743 (K)
Thermal conductivity of solid	k_s	238 (W/m/K)
Thermal conductivity of liquid	k_l	100 (W/m/K)
Density of solid	ρ_s	2700 (kg/m^3)
Density of liquid	ρ_l	2385 (kg/m^3)
Latent heat of melting	L_m	3.896×10^5 (J/kg)
Latent heat of vaporization	L_V	9.462×10^6 (J/kg)
Specific heat capacity of solid	$C_{p,s}$	917 (J/kg/K)
Specific heat capacity of liquid	$C_{p,l}$	1080 (J/kg/K)
Convective heat transfer coefficient	h	20 (W/m^2/K)
Coefficient of linear thermal expansion	β	2.36×10^{-5} (1/K)
Dynamic viscosity	μ	1.6×10^{-3} (Pa.s)
Coefficient of Surface tension	σ	$0.95 \times (1 + 0.13 \times (1 - T/T_m))^{1.67}$ (N/m)
Temperature-dependent surface tension coefficient	$\partial\sigma/\partial T$	-0.3×10^{-3} (N/m/K)
Radiation emissivity	ξ	0.2

3.2.2 Heat and Fluid Flow Model

This study used the modified LS method, an Eulerian technique, to capture the behaviour of the free surface and the vapor/liquid interface, and to compute the normal and tangential elements of the free surface. Moreover, previous studies utilized the modified mixture theory to model the simultaneous existence of solid and liquid phases within the mushy zone (Kong & Kovacevic, 2010; Y. Zhang et al., 2014). The current study extended the mixture theory to include all three phases (solid, liquid, and gas) within the whole domain, accounting for molten, vaporized, and solidified material. The mixture properties were defined by volume fractions of solid, liquid, and gas, ensuring an accurate representation of phase transitions and their impact on material behaviour during welding. These methodologies were employed to simulate keyhole formation and molten pool behaviour, taking into account free surface dynamics, recoil pressure, surface tension effects, buoyancy forces, evaporation effects, and mass loss due to vaporization. The numerical investigation was based on the following assumptions:

- The movement of molten material in the fusion zone was simulated assuming Newtonian behaviour, incompressibility, and laminar flow characteristics.
- Temperature-dependent changes in aluminum's thermophysical properties were disregarded. Instead, the modified mixture theory was applied to calculate thermophysical properties, such as thermal conductivity, specific heat, and density, for each element by utilizing fixed values for the solid, liquid, and gas phases of aluminum. These properties were then averaged according to the phase proportions within each element, yielding an effective constant thermophysical property for the simulation (SaediArdahaei & Pham, 2024a).
- The mushy zone was treated as a porous medium permeated by molten metal (Y. Zhang et al., 2014).
- Plasma effects and the Knudsen layer were excluded from the model.
- Multiple reflections of the laser beam within the keyhole were disregarded in this study. This assumption is justified for scenarios with low penetration depths, as multiple reflections become significant primarily in cases of deeper weld penetration (greater than 600 μm) (Lee et al., 2002). Moreover, the laser beam coefficient of absorption was assumed constant at keyhole walls.
- The vaporized material was modelled as an ideal gas that is transparent to the incoming laser beam.

The transport phenomena in all three phases (solid, liquid, vapour) present during the welding process were addressed by solving the conservation equations of energy (Equations (3.1) – (3.9)), mass conservation (Equation (3.10)), and momentum (Equations (3.11)– (3.15)). Also, the modified conservative equation of the LS method was solved to account for evaporation (Equations (3.16) and (3.17)). The governing equations are briefly provided below, with more detailed information available in our previous article on pulse wave modulation (SaediArdahaei & Pham, 2024a).

- Energy equation and its concerning parameters

The thermal field calculations were performed by solving the transient heat conservation equations across both the solid/liquid and gas regions:

$$\rho C_p \frac{\partial T}{\partial t} + \rho C_p \vec{u} \cdot \nabla T = \nabla \cdot (k \nabla T) + (q_{Laser} - Q_{vapor})\, \delta(\phi) \tag{3.1}$$

$$q_{Laser} = \frac{\alpha n P_{Laser}}{\pi R_{eff}^2} exp\,(\frac{-nr^2}{R_{eff}^2}) B_t \tag{3.2}$$

$$B_t = \begin{cases} 1, & t \le t_p \\ 0, & t > t_p \end{cases} \tag{3.3}$$

$$Q_{vapor} = -L_V \dot{m}_{H-L} \tag{3.4}$$

$$\dot{m}_{H-L} = \sqrt{\frac{M}{2\pi R}} \frac{P_{sat}(T)}{\sqrt{T}} (1 - \beta_r) \tag{3.5}$$

$$P_{Sat} = P_{atm}\, exp\left[\frac{M L_v}{R T_v}\left(1 - \frac{T_v}{T}\right)\right] \tag{3.6}$$

where T represents temperature, t denotes time, ρ is the density, C_p stands for specific heat capacity, k is the thermal conductivity, and $\vec{u}$ is the velocity vector. q_{laser} and Q_{vapor} are the heat sources, representing the laser energy and the energy loss by evaporation. α is aluminum's absorptivity. P_{Laser} represents the peak laser power, and B_t refers to the temporal distribution of the laser, applied to simulate the effects of the pulse wave laser welding, respectively. R_{eff} refers to the effective radius of the laser beam spot and t_p represents the duration of the pulse. To apply the laser heat flux to the material surface and account for evaporation-induced energy loss, the delta function associated with the LS variable ($\delta(\phi)$) was used. The energy loss through evaporation was deducted from the laser energy density, and the remaining energy was multiplied by the delta function of the LS variable to apply these effects on the vapour/liquid interface. In addition, $\dot{m}_{H-L}$ represents the evaporative mass loss, while P_{Sat} denotes the saturated vapour pressure expressed by the Hertz–Langmuir relation and the Clausius–Clapeyron law, respectively (Mayi et al., 2020). β_r stands for the retro-diffusion coefficient, whereas R refers to the universal gas constant and M represents the molar mass of vaporized particles. The enthalpy of fusion L_m and evaporation L_V were introduced through equivalent specific heat using Equations (3.7)– (3.9) (Mayi et al., 2020; Tomashchuk et al., 2016).

$$Cp_{eff} = Cp_{sl} + L_m D_m + L_V D_V \tag{3.7}$$

$$D_m = exp^{\left(\frac{-(T-T_m)^2}{dT_m{}^2}\right)} \Big/ \sqrt{\pi dT_m{}^2} \tag{3.8(a))}$$

$$T_m - dT_m \rightarrow T_m + dT_m \tag{3.8(b))}$$

$$D_V = exp^{\left(\frac{-(T-T_V)^2}{dT_V{}^2}\right)} \Big/ \sqrt{\pi dT_V{}^2} \tag{3.9(a))}$$

$$T_V - dT_V \rightarrow T_V + dT_V \tag{3.9(b))}$$

The functions D_m and D_V are Gaussian functions centred around the melting temperature (T_m) and vaporization temperature (T_V), respectively. The equivalent specific heat capacity was determined by incorporating the specific heat of the solid/liquid mixture Cp_{sl} into the calculation (mixture theory), as outlined in Equation (3.7). The smoothing range for the melting (dT_m) was chosen to be 29 K, based on half the difference between the solidus and liquidus temperatures of the material ($(T_l - T_s)/2$) (Mayi et al., 2020). For vaporization, the smoothing range (dT_V) was selected to be 50 K, as suggested by Tomashchuk et al. (Tomashchuk et al., 2016).

- Modified mass conservation equation and recoil pressure

The impact of recoil pressure was added to the continuity equation using a source term, which was suggested by Zhang et al. (Y. Zhang et al., 2014) and Courtois et al. (Courtois et al., 2014) as presented in Equation (10):

$$\nabla \cdot \vec{u} = \delta(\phi)\dot{m}_{H-L}\left(\frac{\rho_l - \rho_v}{\rho^2}\right) \tag{3.10}$$

where $\delta(\phi)$ introduced a Heaviside function for the LS variable to ensure smooth phase transitions and interface traversal in finite element computations (Y. Zhang et al., 2014). This method minimized discontinuities, particularly for temperature-sensitive material properties and forces such as surface tension, recoil pressure, and the laser heat source, which are confined to the interface. Multiplying these forces by $\delta(\phi)$, they were confined to the vapour/liquid interface during calculations, ensuring they only had non-zero values at that precise location.

- Momentum equation:

$$\rho\left(\frac{\partial\vec{u}}{\partial t}+(\vec{u}\cdot\nabla)\vec{u}\right)=\nabla\cdot[-pI+\mu(\nabla\vec{u}+(\nabla\vec{u})^{T})])+\rho\vec{g}-\rho_l\beta_l(T-T_m)\vec{g}\phi-\mu_l K\vec{u}+(\gamma\vec{n}k-\nabla_s\gamma)\delta(\phi) \tag{3.11}$$

$$\vec{F}_{st}=(\gamma\vec{n}k-\nabla_s\gamma)\delta(\phi) \tag{3.12}$$

$$\vec{F}_{Buoyancy}=-\rho_l\beta_l(T-T_m)\vec{g}\phi \tag{3.13}$$

$$F_{Darcy\ Damping}=-\mu_l K\vec{u} \tag{3.14}$$

$$K=\frac{\frac{180}{d^2}(1-V_l)^2)}{{V_l}^3+b} \tag{3.15(a))}$$

$$V_l=\begin{cases}1, & T>T_l\\ \dfrac{T-T_s}{T_l-T_s}, & T_s\le T\le T_l\\ 0, & T<T_s\end{cases} \tag{3.15(b))}$$

where μ is the dynamic viscosity, and $(\nabla\vec{u})^T$ indicates the transpose of the gradient of the velocity vector $\vec{u}$. ρg represents the effect of gravity, $\vec{F}_{st}$ is the surface tension effect, $\vec{F}_{Buoyancy}$ is the buoyancy effect with β_l serving as the liquid's volume expansion coefficient, and $F_{Darcy\ Damping}$ is Darcy's damping force. b was used to avoid division by zero, d is a constant proportional to the dendrite size and set to 10^{-2} cm (Pang et al., 2011), and V_l is the volume fraction of the fluid. It is noted that the direction of the Marangoni force in the surface tension force depends on the temperature gradient along the interface, not purely the geometric tangent direction. Due to the intense heating at the laser axis and cooler conditions radially outward, the primary temperature gradients along the interface occur horizontally (radially). This horizontal temperature gradient means the tangential surface tension gradient (Marangoni effect) strongly manifests itself in the radial direction. Thus, in an axisymmetric laser-welding configuration, the Marangoni force significantly influences radial fluid motion within the melt pool, while curvature forces influence the axial shaping of the keyhole.

- Modified transport equations of the LS method

The vapour/liquid interface tracing was carried out using the modified LS method, as described in Equation (3.16). This study introduced an improved conservative Level Set method,

combining the Volume of Fluid (VOF) approach with the narrow band LS method and included a gas dynamic source term (Olsson & Kreiss, 2005). This source term accounted for evaporation effects, caused by vapor pressure and mass loss at the interface. The equations were as follows:

$$\frac{\partial \phi}{\partial t} + \vec{u} \cdot \nabla \phi - \delta(\phi)\dot{m}_{H-L}\left(\frac{V_{f,1}}{\rho_v} + \frac{V_{f,2}}{\rho_l}\right) + \gamma_{ls}\nabla \cdot \left(\phi(1-\phi)\frac{\nabla \phi}{|\nabla \phi|} - \epsilon_{ls}\nabla \phi\right) = 0 \quad (3.16)$$

$$\phi(x,t) = \begin{cases} 0, & T > T_V, & dist(x, \Gamma(t)) < -\epsilon_{ls} \\ 0.5, & T_l < T < T_V, & |dist(x, \Gamma(t))| \leq \epsilon_{ls} \\ 1, & T < T_l, & dist(x, \Gamma(t)) > \epsilon_{ls} \end{cases} \quad (3.17)$$

where γ_{ls} refers to the reinitialization parameter associated with the flow velocity, while ϵ_{ls} regulates the thickness of the interface. Here, γ_{ls}, the reinitialization parameter, ensures that the level-set function $\phi(x,t)$ remains a signed distance function near the interface $\Gamma(t)$, where $\phi(x,t) \approx dist(x, \Gamma(t))$. Additionally, ϕ is the LS variable that varies smoothly between 0 and 1 within the interface layer, being set to 0.5 at the vapour/liquid interface, as shown in Equation (3.17). Defining this variable across all elements of the computational domain, and transporting it through fluid flow calculations, facilitated tracking the vapor/liquid interface and distinguishing between condensed and gaseous phases. The third term on the left side of Equation (3.16) is the source term added to the standard transport equations of the LS equation, enhancing the effect of evaporation-induced mass loss at the interface. This term facilitated the smooth transport of the LS variable (ϕ) in finite element calculations on both sides of the interface by using the $\delta(\phi)$, as well as the volume fractions and densities of the liquid and gaseous phases. Additionally, $V_{f,1}$ represents the volume fraction of gas, and $V_{f,2}$ denotes the volume fraction of a solid/liquid mixture.

- Boundary and initial conditions

As depicted in Figure 3.1(a), a Gaussian laser heat flux is applied to boundary CD, which is also subjected to convective heat transfer to the environment ($h(T_{ext} - T_a)$) and radiative heat transfer ($\xi K_b(T^4 - {T_a}^4)$), where K_b is the Stefan–Boltzmann constant, and T_a is the ambient temperature. The initial temperature was set to 296 K, with the initial velocity and pressure values considered zero at the surface and for all solid surfaces far from the heat source.

Boundary AE was designated as the axis of symmetry, ensuring that no flow crosses the axis (AE), and the temperature gradient remains zero along the axis. A wetted wall condition was imposed on boundaries BD, DF, and EF. All other boundaries were treated as thermally insulated.

3.2.3 Numerical Considerations

Melting and solidification were modelled using the thermal enthalpy–porosity technique (Y. Zhang et al., 2014), while evaporation was simulated with the modified conservative LS method (Olsson & Kreiss, 2005). Additionally, the modified mixture theory was employed to account for mixture effects, simplifying finite element calculations at the interface, particularly for the elements containing multiple phases (Kong & Kovacevic, 2010; Y. Zhang et al., 2014). The modified mixture theory, Level Set (LS) method, and enthalpy–porosity technique were employed due to their strong capability to model phase transformations, fluid flow, and keyhole morphology. These methods facilitate a comprehensive understanding of the complex vapour/liquid and solid/liquid interactions, thereby ensuring high fidelity and reliable results. Each of these methods was independently implemented within the LS, heat transfer in fluids, and laminar flow modules of COMSOL Multiphysics. To account for the coupling effects between the incorporated methods and interfaces, two COMSOL Multiphysics coupling interface modules were employed. The LS, mixture properties, and laminar flow were coupled using the two-phase flow interface. Additionally, the non-isothermal Multiphysics interface was used to couple the heat transfer in fluids and laminar flow interfaces. Finally, these two coupling modules were further integrated under the overarching Multiphysics interface within COMSOL to ensure comprehensive calculations.

3.2.3.1 Numerical Setup

The model was developed in the Multiphysics interface of COMSOL Multiphysics 5.6, using the coupling heat transfer, fluid motion, and transport equations of LS. A mapped mesh with quadrilateral elements and extra-fine meshes was used and calibrated for fluid dynamics (Figure 3.3). The element size chosen for the mesh was set at 0.02 mm. The simulation, which

modelled 10 ms of laser welding over 17 h, was run on a Lenovo ThinkStation P720 workstation, equipped with an Intel® Xenon® Gold 5118 CPU (12 cores, 24 logical processors) with 128 GB RAM. The CPU was manufactured by Intel corporation, head-quartered in Santa Clara, California, USA. The system was assembled by LENOVO, based in Beijing, China. Time steps were set at 10 μs. For fluid flow calculations, a PARDISO direct solver with a nested dissection multithreaded preordering algorithm was used, while the LS transport and heat transfer equations employed a PARDISO direct solver with an automatic preordering algorithm. Before running the simulation, mesh element count, reinitialization parameter, and interface thickness were verified to ensure reliable outcomes. Sensitivity analysis was conducted iteratively, refining parameters by monitoring convergence trends and keyhole depths. Mesh sensitivity analysis involved testing four different mesh counts: 16,968, 24,320, 37,500, and 48,045 elements. The optimal mesh element count was determined to be 37,500, as keyhole morphology and depth showed no significant changes with more elements. The best reinitialization parameter and interface thickness values for the LS technique were found to be 5 m/s and 0.03 mm, respectively, which provided better computational efficiency and convergence. Further variations in these parameters showed no significant impact on keyhole depth and morphology.

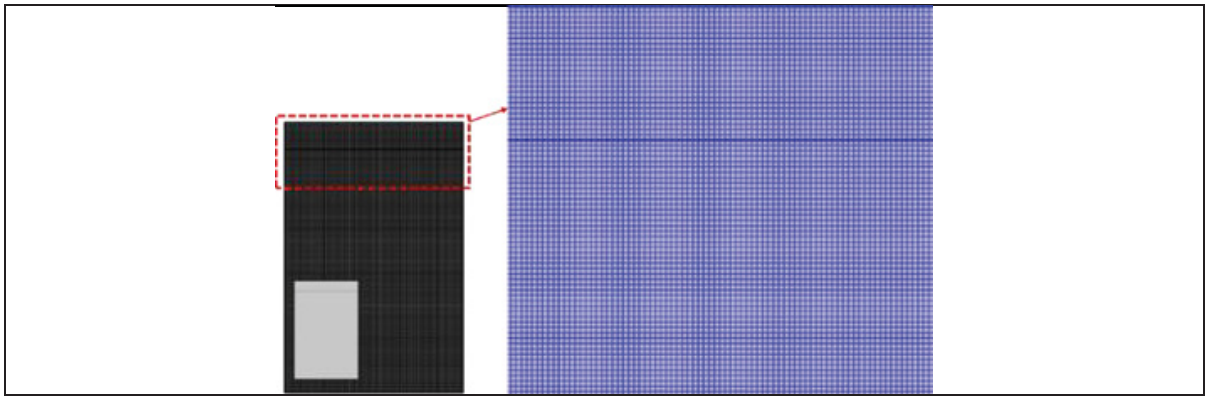

Figure 3.3 Computational domain with the corresponding extra-fine mapped mesh

3.2.3.2 Model Validation

The current numerical model was validated with the experimental work of Qin et al. (Qin et al., 2011) and presented in our previous article (SaediArdahaei & Pham, 2024a). Correspondingly, the keyhole penetration depth, shape, and width obtained from the current numerical model were compared to the observed keyhole morphology from Qin et al.'s experiments (Qin et al., 2011), as shown in Figure 3.4. The simulation used the same laser characteristics: total laser energy of 18 J, pulse width of 3 ms, and spot radius of 300 µm with the one utilized by Qin et al. (Qin et al., 2011). The numerical results showed a keyhole penetration depth of 3.837 mm, closely matching the experimental value of 3.824 mm. Simulated and experimental keyhole spot diameters on the surface were approximately 0.937 mm and 0.936 mm, respectively. The maximum keyhole width reported experimentally was about 0.407 mm, while the numerical simulations showed a width range of 0.310 mm and 0.51 mm. The model accurately predicted the keyhole depth and diameter, with slight deviations of 6–12% in keyhole width. These discrepancies could be attributed to differences in material properties, the neglect of multiple laser beam reflections, and assumptions about metallic vapour transparency and plasma effects. Despite these factors, the model successfully correlated with the experimental results, effectively predicting keyhole diameter and depth, and providing acceptable keyhole width values.

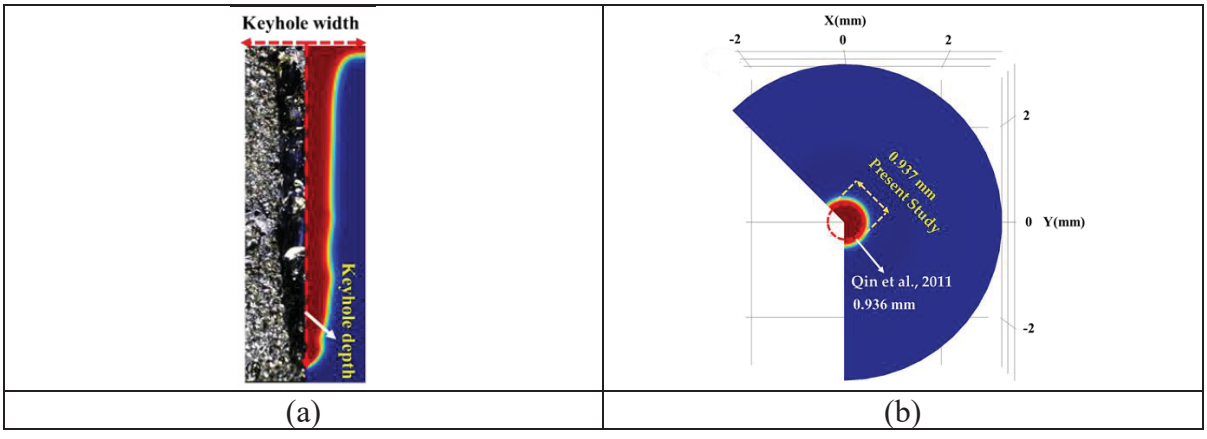

Figure 3.4 Comparison of (a) the keyhole morphology from the simulation with the experimental results taken from Qin et al. (2011) and (b) the keyhole surface diameter Adapted from Qin et al., (2011)

3.2.3.3 Instability Analysis Procedure

Increased instability directly correlates with keyhole collapse probability, leading to severe fluctuations, collapses, and defect formation. This study investigates the parameters contributing to keyhole instability by examining three main criteria as follows:
Geometry: keyhole stability is achieved by maintaining an open keyhole with slight fluctuations and a symmetrical shape with smooth transitions from top to bottom. Ensuring these geometrical characteristics reduces the risk of keyhole collapse. Force analysis: a stable keyhole is characterized by the equilibrium between the driving forces acting on the keyhole and the molten pool. Stability and a fully open keyhole are maintained as long as the equilibrium between recoil pressure and the forces contributing to keyhole collapse—such as surface tension, Darcy's damping force, gravity, and buoyancy is preserved (Chen et al., 2019; Schauer, 1977). The sensibility of these driving forces across different cases with various pulse shapes presented in this article was analyzed to understand the impact of fluctuations and magnitudes of these collapse-inducing forces on keyhole instability and overall process stability. Fluid behaviour: high-velocity magnitudes and multiple peaks indicate intense fluid flow behaviour, which might contribute to keyhole instability. Intense fluid flow within the keyhole and molten pool might increase instability due to chaotic fluid motion, leading to irregular keyhole walls and a higher risk of collapse.

3.3 Results and Discussion

This section provides an in-depth analysis of the impact of pulse shaping on keyhole instability and penetration depth. Keyhole instability is examined through detailed assessments of morphology, geometry, quantitative force analysis, and fluid flow behaviour, as discussed in the following sections.

3.3.1 Keyhole geometry Analysis

Keyhole mode laser welding begins with irradiating high laser energy density on the material, raising its temperature. When the material's temperature exceeds the melting and vaporization points, it undergoes fusion and evaporation, forming and propagating the keyhole due to recoil pressure and mass loss from the surface. Figure 3.5 shows different keyhole geometries at the end of the welding process, considering various laser energy pulse shapes defined in Table 3.1 and Figure 3.2. The penetration depth in Case 2 with PW laser welding was significantly greater than in Case 1 with continuous wave welding (CW), attributable to PW's higher laser energy density, which accelerated recoil pressure domination and keyhole formation. Moreover, both Cases 1 and 2 exhibited symmetrical keyholes. However, Case 2 demonstrated slightly steeper wall angles at the top, which suggests increased fluctuations, likely due to the use of higher initial laser power. For Cases 3 to 7, variant rectangular pulse shapes with fixed total laser energy of 20 J were analyzed, showing stable and cylindrical keyhole shapes. With higher initial laser power, Case 5, featuring a ramp-down pulse shape, generated a deeper and narrower keyhole compared to Case 6, which had a ramp-up shape. The faster keyhole formation and the dominance of recoil pressure in Case 5 contributed to greater penetration and concentrated energy at the bottom part of the keyhole, rather than dispersing it along the walls to widen the keyhole. Moreover, Case 4 showed a higher potential for keyhole collapse at the top due to steeper wall angles, leading to pinching and potentially causing the keyhole to become narrower and less stable. Additionally, the significant power drop from 4 kW to 2 kW at the second rectangular step promoted solidification and allowed other driving forces to dominate over recoil pressure, closing the keyhole. Simultaneous ramp-down/up pulse shapes, as seen in Cases 3 and 7, resulted in smoother transitions from top to bottom, enhancing stability without significantly affecting penetration depth. Cases 8 to 11 investigated triangular pulse numbers, maintaining total laser energy at 20 J. Increasing from one to eight triangular pulses (single, double, quadruple, and octuple peaks), Cases 8 and 10 exhibited more stable keyholes with smoother transitions from top to bottom. Case 8 showed a narrower and deeper keyhole compared to the wider keyhole in Case 10, and both cases showed no wall fluctuations or inward pulling of the walls in the top part of the keyhole. In contrast, Cases 9 and 11

displayed wall fluctuations and inward pulling of the keyhole walls at the top. Cases 12 to 15 explored higher laser energy densities with shorter pulse periods, reducing total laser energy to 18 J. Despite lower total energy, full penetration depth increased due to higher starting laser powers and accelerated keyhole formation. However, significant wall fluctuations were noted, indicating instability and collapse risk. Case 12 had the highest penetration depth but also the greatest instability. Mixed high-energy rectangular and triangular pulses (Cases 13 and 15) resulted in more stable keyholes, balancing depth and width to reduce collapse risk.

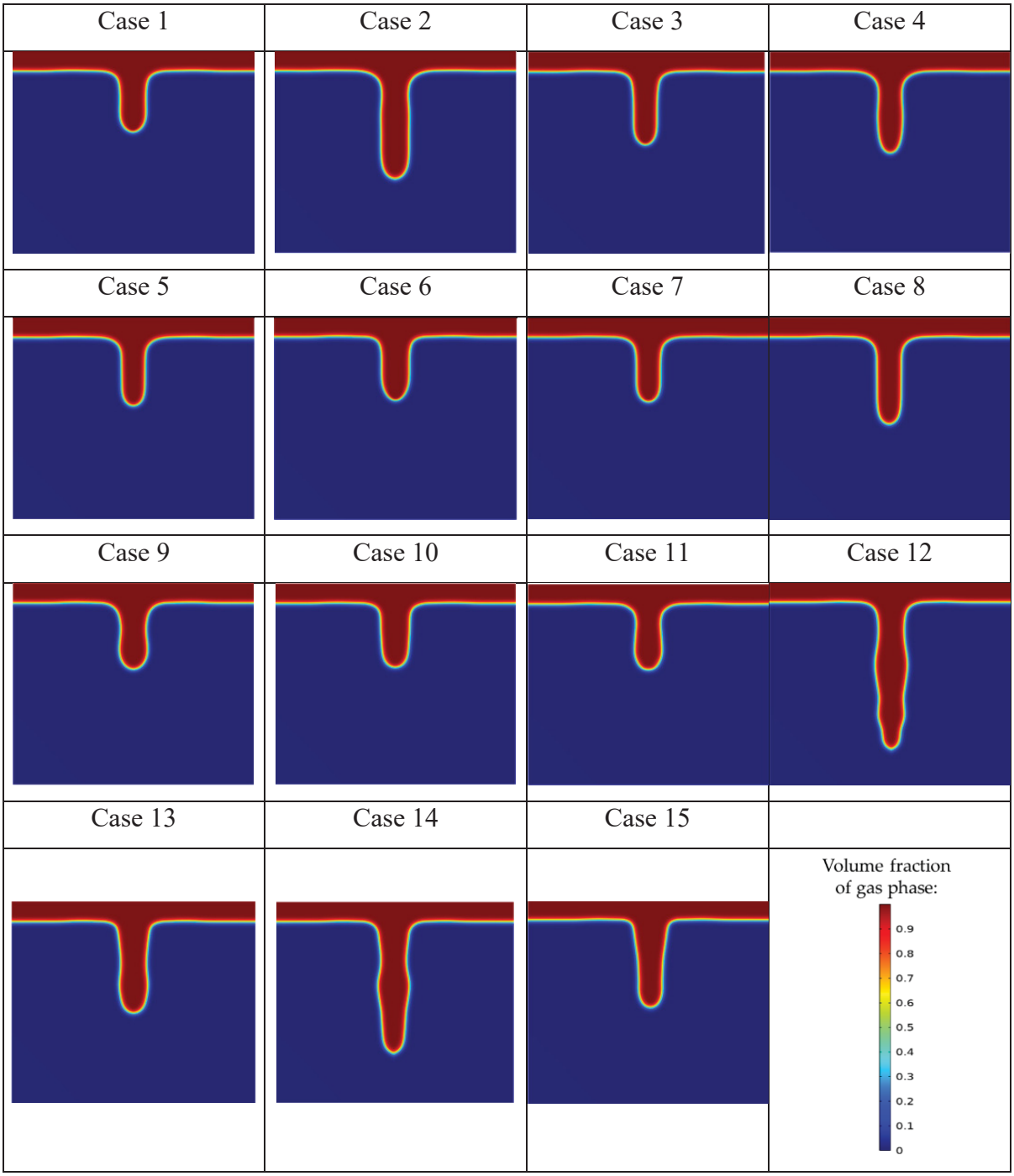

Figure 3.5 Three-dimensional depiction of keyhole morphology and temporal evolution with various pulse shaping cases

3.3.2 Instability-Inducing Forces: Quantitative Analysis

This section presents a quantitative analysis of forces contributing to keyhole collapse and instability, including surface tension forces (curvature effect and Marangoni effect), Darcy's damping forces, gravity, and buoyancy, as illustrated in Figure 3.6. These forces were extracted by calculating their maximum value per unit volume in the material domain using a pre-defined domain probe. It was found that buoyancy and gravity forces had a negligible impact compared to other forces. It is noted that in a 2D axisymmetric domain, surface tension forces can be decomposed into components in the r and z directions. The curvature-induced normal force mostly acts in the z-direction (inward/outward at the top of the keyhole), while the tangential component, associated with the Marangoni effect due to surface tension gradients along the interface, typically has a larger projection in the radial (r) direction. This is because, Correspondingly, the surface tension force in the axial direction (curvature effect) was more intense than in the radial direction (Marangoni effect), creating a pressure difference across the keyhole walls that pulled them inward, increasing the likelihood of collapse. The next dominant force was Darcy's damping force in the axial and radial directions, which contributed to keyhole instability by resisting fluid motion within the mushy zone. At the beginning of the laser pulse, a large amount of energy was abruptly deposited into the material, causing rapid temperature increases, intense fusion, vaporization, and keyhole formation. As vapour pressure rapidly increased due to steep temperature gradients, there was a sharp spike in Darcy's damping force and surface tension. As the laser continued to interact with the material, the system reached a quasi-steady state where the molten pool and keyhole stabilized to some extent with a fully opened keyhole, causing the forces to equilibrate. According to the diagrams, both the curvature and Marangoni effects are greater for PW compared to CW due to greater laser energy deposition in shorter pulse periods. Additionally, more erratic behaviour was seen for Darcy's damping force after turning off the laser in PW. In correlation with the keyhole morphology presented in Figure 3.5, it was found that erratic variations in Darcy's damping force and greater curvature and Marangoni effects contributed to steeper keyhole wall angles and inward pulling in the upper part of the keyhole, indicating more instability. Analyzing Cases 3 to 7, Case 3, which used a ramp-down varying rectangular pulse shape,

exhibited the maximum curvature effect with multiple peaks and erratic behaviour compared to other cases. This was supported by data indicated in Figure 3.5, showing less keyhole wall stability. The steeper wall angles at the top of the keyhole resulted from the inward pulling due to greater pressure differences associated with the higher curvature effect. Ramp-down varying rectangular pulse shapes (Cases 4, 5, and 7) showed faster force stabilization around and after 0.002 s compared to ramp-up cases (Cases 3 and 6), which exhibited prolonged fluctuations. Cases 5 and 7, with gradual ramp down and gradual ramps of down-up-down, showed fewer fluctuations and faster force stabilization. For Cases 8 to 11, increasing the number of triangular pulse peaks correlated with heightened erratic fluctuations, instabilities in the forces, and multiple peaks. Case 8 demonstrated relatively smoother force variations, which in correlation with its keyhole morphology, contributed to a smoother transition from the top to the bottom of the keyhole, resulting in greater stability. In comparing Cases 12 through 15, it was observed that Cases 12 and 13, utilizing single multi-pulse rectangular and triangular shapes, experienced stronger curvature effects and Darcy's damping forces than the combined multi-pulse shapes in Cases 14 and 15. This led to increased keyhole instability and greater fluctuations along the keyhole walls. Case 15 showed the least curvature effect and fluctuations in the Marangoni effect, along with the least Darcy's damping force, all contributing to a more stable and open keyhole, as corroborated in Figure 3.5.

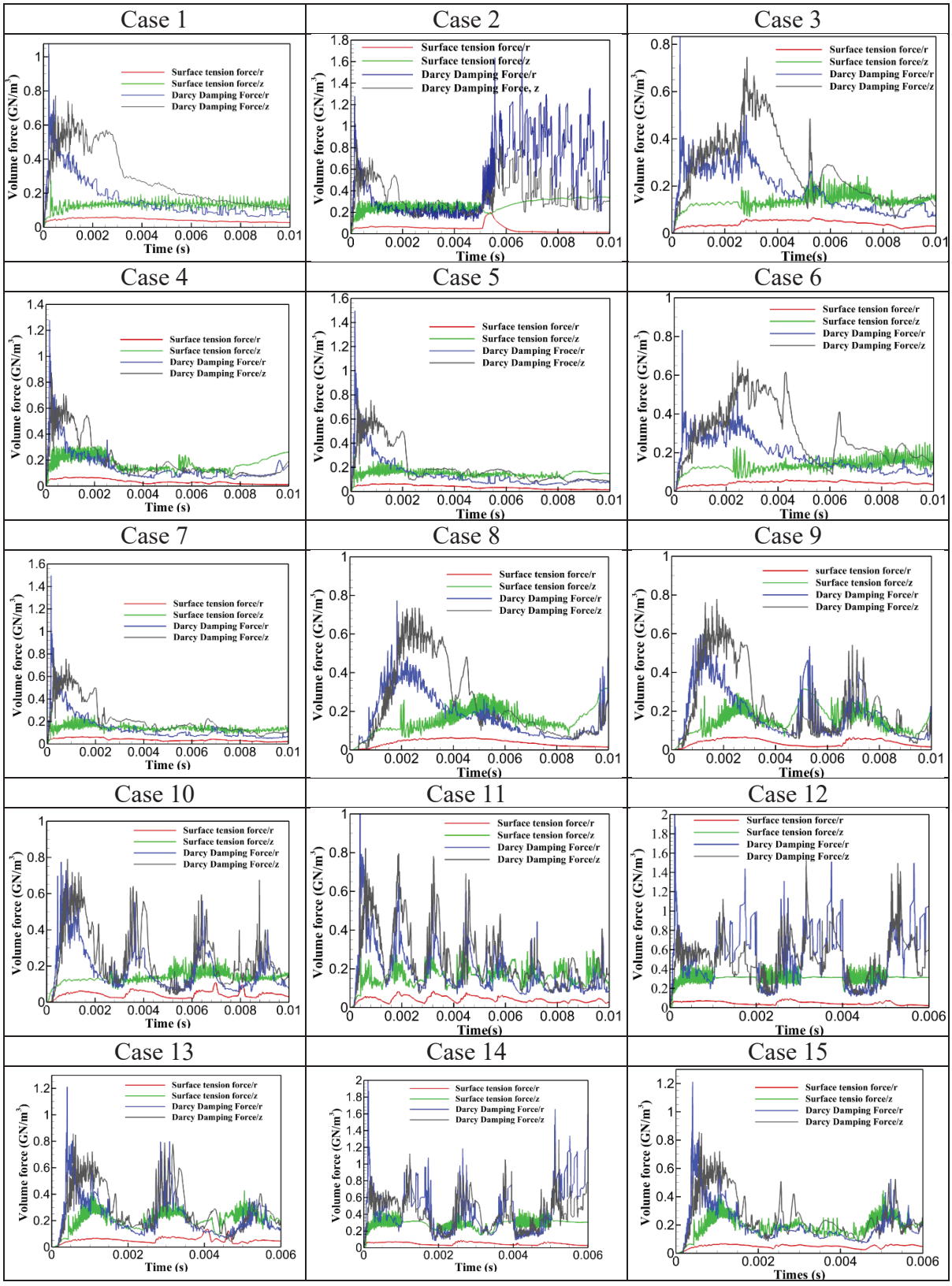

Figure 3.6 Quantitative force analysis for Cases 1 to 15

3.3.3 Fluid Behavior

This section presents the impact of pulse shaping on fluid flow behaviour, using diagrams and comparisons of velocity magnitudes for the investigated cases, as shown in Figure 3.7. The maximum velocity within the keyhole and molten pool correlates with the fluid flow behaviour inside these regions. High and erratic velocity magnitudes suggest strong convective currents, irregular heat and mass transfer, chaotic fluid motion, irregular keyhole walls, and higher chances of collapse. As shown in Figure 3.7, upon exposure to high laser energy density, followed by material fusion and evaporation, fluid velocity increased, exhibiting fluctuations in response to laser deactivation between pulses or due to specific flow dynamics and the influence of multiple forces. It was noted that PW had higher velocity magnitudes compared to CW due to the utilization of higher laser powers, which started to diminish after turning the laser off. As for the variant rectangular pulse shapes, Case 4 had the greatest velocity magnitudes with sudden spikes and falls, leading to more abrupt fluid flow behaviour within the keyhole, contributing to keyhole wall instability as corroborated in Figure 3.5 for keyhole morphology. Additionally, it was demonstrated that the reason for the more stable keyhole and stability in cases with single and quadruple triangular peaks compared to double and octuple triangular peaks is their smoother and lower velocity magnitudes. This led to smoother fluid flow, contributing to a more stabilized keyhole, as shown in their keyhole morphology in Figure 3.5. Similarly, it was further proved that the greater and more spontaneous velocity variations in Cases 12 and 14, compared to Cases 13 and 15, led to more spontaneous fluid flow, contributing to greater keyhole wall fluctuations and instability.

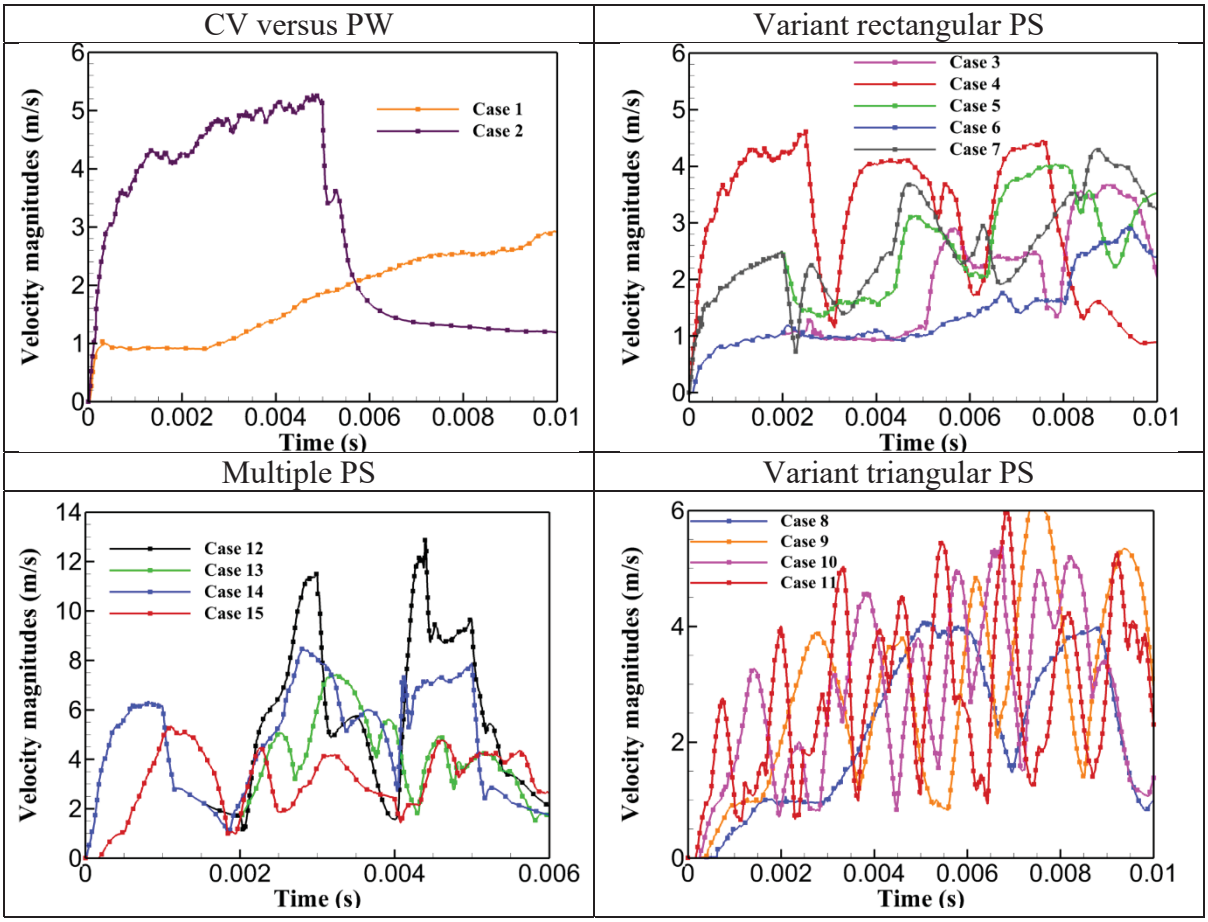

Figure 3.7 Maximum velocity magnitude for Cases 1 to 15

3.3.4 Understanding the Instability of Nature of Selected Cases

This section provides a comparative analysis of selected cases, considering all criteria used for instability analysis. Specifically, Case 8 and Cases 12–15 were selected to explore the correlation between keyhole stability, penetration, and process instability. Among cases with identical pulse shapes, Case 8 was chosen for its higher keyhole stability and penetration depth compared to Cases 1–11. In contrast, Cases 12–15, with multiple pulse shapes, were selected for their higher penetration depths but greater instabilities, allowing for a deeper understanding of instability behaviour and its underlying causes. Firstly, Cases 8, 12, and 15 were chosen and compared to understand the reasons behind different keyhole shapes and variant instabilities. Secondly, the impact of pulse shaping on reducing instability was analyzed to improve understanding of factors responsible for keyhole and process instability. As shown in Figure

3.8, Case 8 exhibited minimal keyhole instability with a smoother transition from top to bottom. In contrast, Case 12 showed significant wall fluctuations along the keyhole walls, indicating a tendency to collapse and increased instability. Case 15, however, provided a relatively shallow and wide keyhole with smoother walls, reducing the possibility of collapse. The intense instability of Case 12 was attributed to two main factors. Firstly, the utilization of high laser energy density resulted in greater Darcy's damping force and surface tension forces in both directions compared to Cases 8 and 15. Greater Darcy's damping force increased resistance to fluid flow, while the stronger curvature effect created a pressure difference across the keyhole walls, pulling them inward and leading to pinching, making the keyhole narrower and less stable. Secondly, Case 12 exhibited the highest and most fluctuated velocity magnitudes, indicating erratic fluid flow behaviour within the keyhole, contributing further to instability. Consequently, the combination of high-velocity magnitudes, fluctuations, pronounced curvature, Marangoni effects, and a stronger influence of Darcy's damping force led to the increased instability observed in Case 12.

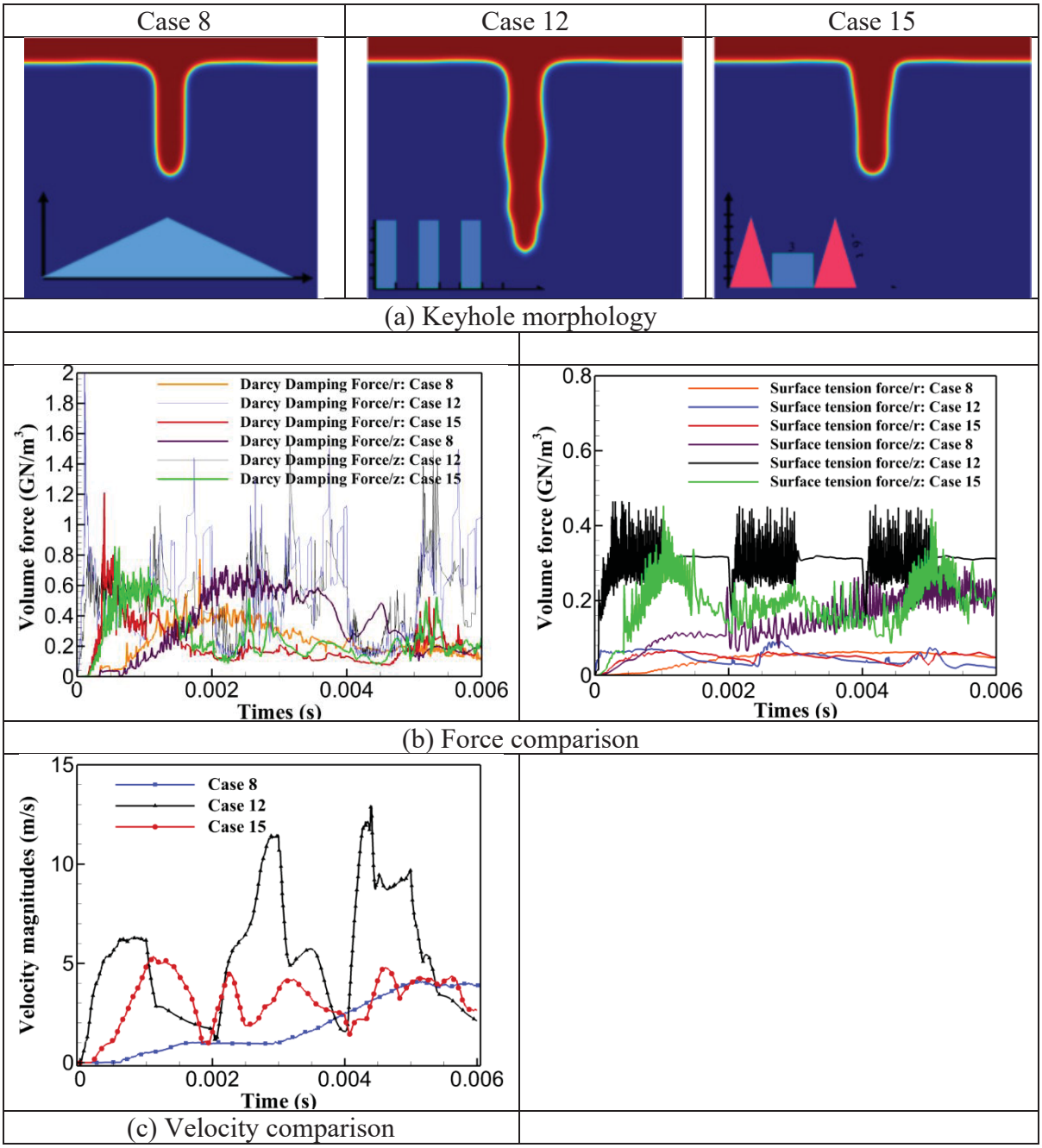

Figure 3.8 Selected cases for comprehensive and comparative instability analysis considering (a) keyhole morphology and (b,c) force analysis and velocity magnitude

Figure 3.9 shows the impact of using combined pulse shapes in reducing the instabilities and fluctuations in the forces, contributing to the keyhole stability. As demonstrated, using combined pulse shapes significantly reduced instability, as illustrated for Cases 12 to 15. The

curvature and Marangoni effects are compared as examples to show how combined pulse shapes improved process stability by reducing force instability and fluctuations. Figure 3.9 depicts that using combined pulse shapes positively contributed to decreasing the instability, fluctuations, and magnitudes of the curvature effect and Marangoni effect which can be seen in the red dashed-line circle. This reduction explains the lower keyhole wall instability observed in Cases 14 and 15 compared to Cases 12 and 13. Using pulse shaping, the abrupt spikes and falls were effectively controlled and smoothed. It is also noted that a similar impact was observed for Darcy's damping forces, although the diagrams are not provided here.

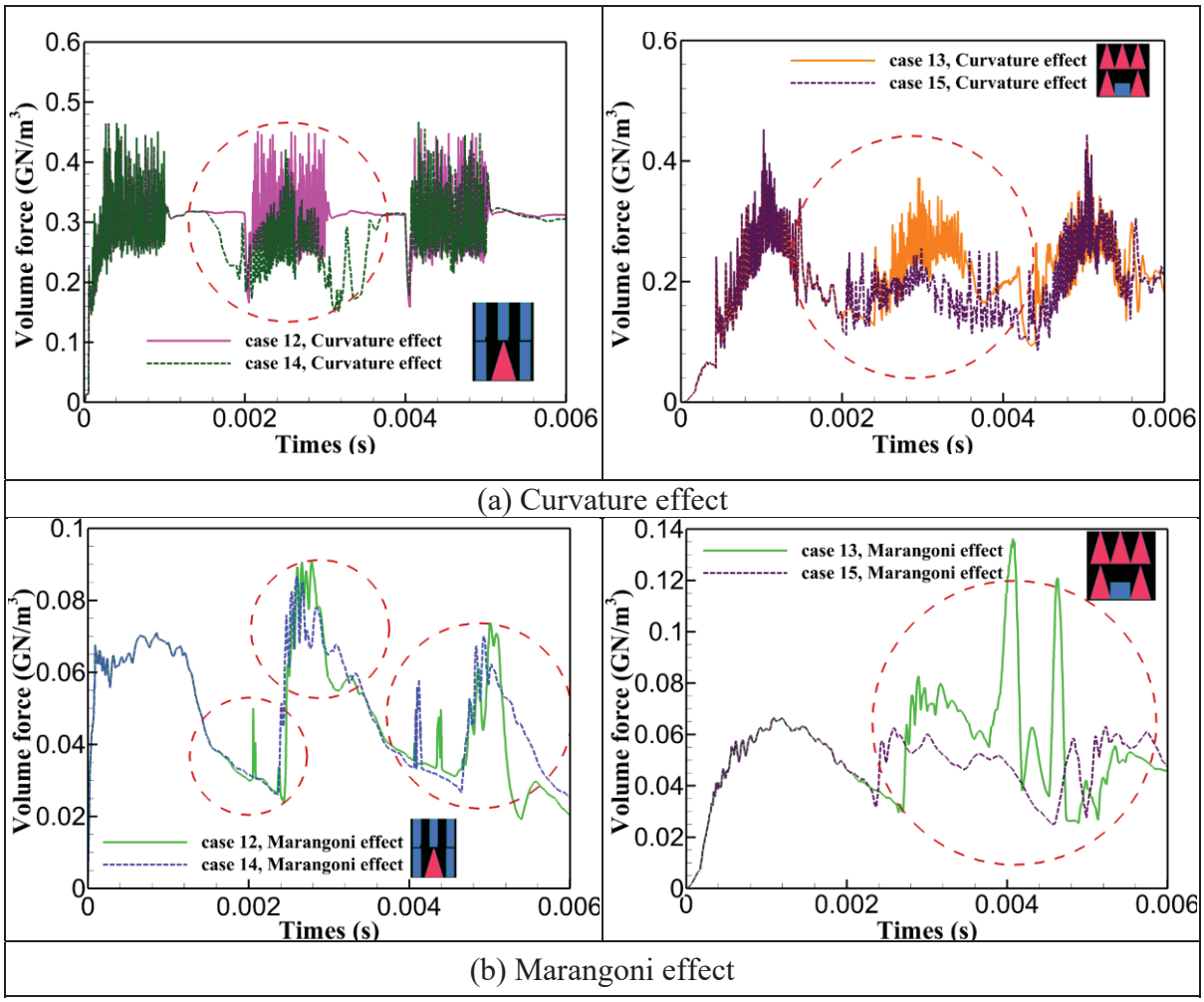

Figure 3.9 Impact of pulse shaping on instability reduction in forces for (a) the curvature effect and (b) the Marangoni effect

3.4 Conclusions and Future Avenues

Introducing a novel numerical approach for simulating the keyhole mode laser welding on aluminum, the impact of pulse shaping was investigated on the instability of the laser welding process. This study aims to improve the understanding of the underlying criteria contributing to the instability of the keyhole and laser welding process. The instability was comprehensively examined using analysis of the keyhole morphology, velocity magnitude and fluid flow behaviour, and instability-inducing forces such as surface tension, and Darcy's damping force. The following conclusions are observed:

- The combination of the curvature effect, Darcy's damping force, and more intense fluid flow behaviour contribute to the instability of the keyhole and the laser welding process.
- Using short pulse periods with higher laser energy density enhances instability and the possibility of keyhole collapse due to the increased curvature effect, Darcy's damping force, and more intense fluid flow behaviour.
- The instability of the keyhole and process can be controlled using variant rectangular pulse shapes with gradual laser power ramp-up and -down pulse shapes due to smoother variations in velocity, smoother flow behaviour, and fewer curvature effects.
- The instability of the keyhole and forces can be controlled using combinations of triangular and rectangular pulse shapes.
- To minimize instability, the laser power should be high enough to induce evaporation and recoil pressure for keyhole propagation but balanced to avoid the excessive curvature effect, Darcy's damping force, and fluid velocity that accompanies higher power and leads to increased instability.

Overall, this research provides key insights into the factors driving keyhole and process instability in aluminum laser welding. It quantitatively demonstrates how pulse shaping can effectively control and minimize these instabilities by influencing the forces and fluid flow behaviours involved. These findings advance understanding and offer a foundation for future research aimed at optimizing laser parameters by enhancing the understanding of the factors responsible for instability and offering strategies to control them to improve weld quality.

However, some limitations remain. One key limitation is the use of a 2D axisymmetric model. While highly effective for simulating stationary spot welding and serving as a crucial first step toward more complex models, it does not fully capture the complexities of real-world laser welding scenarios that involve laser movement and multiple reflections of laser beams. Future research could explore dynamic laser welding, including the impact of multiple reflections within the keyhole on the instability and how to control and minimize the instabilities induced by multiple reflections of laser beams. This will pave the way for more advanced models with optimized welding parameters, incorporating laser movement and other real-world conditions.

CHAPTER 4

MULTI-RESPONSE OPTIMIZATION OF ALUMINUM LASER SPOT WELDING WITH SINUSIODAL AND COSINUSIODAL POWER PROFILES BASED ON TAGUCHI–GREY RELATIONAL ANALYSIS

Saeid SaediArdahaei and Xuan-Tan Pham [a]

[a] Department of Mechanical Engineering, École de Technologie Supérieure, 1100, Notre-Dame West, Montreal, Quebec, Canada H3C 1K3

Paper published in *Materials*[3], June 2025

Abstract

Laser weld quality remains a critical priority across nearly all industries. However, identifying optimal laser parameter sets continues to be highly challenging, often relying on costly, time-consuming trial-and-error experiments. This difficulty is largely attributed to the severe fluctuations and instabilities inherent in laser welding, particularly keyhole instabilities. This study examines the impact of laser power modulation parameters, which, when properly applied, have been found effective in controlling and minimizing process instabilities. The investigated parameters include different pulse shapes (sinusoidal and cosinusoidal) and their associated characteristics, namely frequency (100–800 Hz) and amplitude (1000–4000 W). The impact of these modulation parameters on keyhole mode laser spot welding performance in aluminum is investigated. Using a Taguchi experimental design, a series of tests were developed, focusing on eight key welding responses, including keyhole dimensions, mean temperature, and the variability of instability-inducing forces and related factors affecting process stability. Grey relational analysis (GRA) combined with analysis of variance (ANOVA) is applied to identify the optimal combinations of laser parameters. The results indicate that low amplitude (1000 W), low-to-intermediate frequencies (100–400 Hz), and cosinusoidal waveforms significantly enhance weld quality by improving process stability and balancing penetration depth. Among the factors, amplitude has the greatest impact, accounting

[3] Material 2025, *18*(13), 3044

for over 50% of the performance variation, followed by frequency and pulse shape. The findings provide clear guidance for optimizing laser welding parameters to achieve stable, high-quality aluminum welds.

Keywords: Keyhole, surface tension, Darcy damping force, instability, optimization, RSD, GRA analysis, ANOVA

4.1 Introduction

Aluminum and its alloys are widely used in industry due to their high strength-to-weight ratio, corrosion resistance, and excellent electrical conductivity (Miller et al., 2000). Being nearly three times lighter than steel and about half the weight of titanium, they are particularly suitable for electric vehicle body structures and battery components (Bunaziv et al., 2024).

Laser welding is widely adopted in the automotive and aerospace sectors for producing deep, precise welds in aluminum alloys (Schubert et al., 2001; L. Wang et al., 2023). However, challenges persist due to aluminum's high reflectivity, thermal conductivity, and oxidation tendency (Bunaziv et al., n.d.). Pulsed wave (PW) lasers help address these issues by using high initial energy density to overcome reflectivity while maintaining controlled average power to reduce overall heat input (Cavilha Neto et al., 2021; Hajavifard et al., 2016). Keyhole-mode laser welding, a deep penetration technique for aluminum alloys, has been widely studied due to its complex process control. This mode typically initiates at a power density around 10^6 W/cm², where intense metal vaporization creates a keyhole and induces recoil pressure (Svenungsson et al., 2015). Keyhole-mode laser welding enhances productivity with welding speeds up to 20–30 times faster, while optimized parameters improve the mechanical properties of welded aluminum components (Fetzer et al., 2018).

Porosity is a common challenge in aluminum welding, mainly due to hydrogen solubility and keyhole instability. The evaporation of volatile alloying elements (e.g., Zn, Mg, and Li) further destabilizes the process (Bunaziv et al., n.d.). Additionally, the narrow process window and rapid keyhole formation within microseconds complicate experimental studies due to erratic weld pool and keyhole behavior (Pang et al., 2015). Inherent instabilities in keyhole laser

welding limit its broader industrial adoption. Keyhole stability depends on the dynamic interplay of highly transient and fluctuating forces, such as surface tension (Marangoni and curvature effects), recoil pressure, hydrostatic and hydrodynamic pressures, and Darcy damping. Balancing these forces is essential to improve stability and reduce defects (Chen et al., 2019; SaediArdahaei & Pham, 2024b).

Laser power manipulation has shown effectiveness in controlling instabilities. Ardahaei et al. provided insights into the numerical modeling of keyhole instabilities in laser spot welding of aluminum using power wave modulation (PWM) (SaediArdahaei & Pham, 2024b, 2024a). Their study revealed that curvature effects and Darcy damping forces are key contributors to keyhole instability. Optimized pulse shapes, such as single- or quadruple-peak triangular and ramp-down rectangular pulses, effectively reduced spontaneous force fluctuations, enhancing process stability and minimizing defect probability. In a separate study, they demonstrated that rectangular pulses increased penetration depth by over 80% compared to continuous wave (CW) lasers, with power and frequency modulation significantly affecting keyhole behavior. Matasunawa et al. (Matsunawa et al., 1998) showed that PWM considerably minimizes porosity by stabilizing keyhole and molten pool behavior. Tsukamoto et al. (Tsukamoto et al., n.d.) further demonstrated that aligning modulation frequency with the molten pool's natural oscillations significantly enhances keyhole stability and minimizes porosity formation. Zhang et al. (M. Zhang et al., 2022) investigated sinusoidal power modulation in fiber laser welding of AZ31B magnesium alloy, reporting improved energy coupling, reduced underfill, refined microstructure, and enhanced mechanical properties due to improved keyhole and melt pool stability. Heider et al. (Heider et al., 2015) studied copper welding and found that sinusoidal power modulation, particularly at normalized frequencies of 0.2–0.4, reduced defects like pores and melt ejections by up to 90%, while improving keyhole stability. They optimized parameters such as modulation frequency, amplitude, and focal size to achieve deeper, more stable penetration.

A review of the literature indicates a gap in multi-response optimization for keyhole-mode laser welding of aluminum. While several researchers have proposed such techniques, most studies have lacked a comprehensive approach to simultaneously optimize multiple desired outcomes. Omoniyi et al. (Omoniyi et al., 2025) applied the Taguchi method combined with

grey relational analysis (GRA) to optimize the laser welding of Ti6Al4V, balancing bead geometry and micro-hardness. Their study highlighted GRA's effectiveness in multi-objective welding problems where single-response optimization is insufficient. In another research, Tsai et al. (Tsai & Wu, 2022) used Taguchi-GRA to optimize multiple quality attributes such as roundness, taper, and (heat affected zone) HAZ in the laser drilling of acrylic. By integrating diverse metrics into a single grey relational grade, the method effectively identified optimal parameters and balanced trade-offs among competing objectives, demonstrating GRA's strength in multi-response optimization. This study presents a numerical investigation of keyhole-mode laser spot welding on aluminum, experimentally validated and optimized using Taguchi-based GRA. A novel cosinusoidal PWM profile was introduced and compared with continuous and sinusoidal profiles to assess its effectiveness in minimizing keyhole instabilities. GRA was employed to address the lack of robust multi-response optimization methods, enhancing simulation precision by reducing factors contributing to instability.

4.2 Experimental Details and Material

Figure 4.1 shows the experimental setup for laser spot welding on aluminum using continuous, sinusoidal, and cosinusoidal pulse profiles. A fiber pulsed laser machine (IPG YLS-6000: Ytterbium Laser) with a maximum output laser power of 6 kW and a laser wavelength of 1090 nm was utilized to perform laser spot welds on test samples. The focal length of the laser was 300 mm, producing a beam diameter of 0.3 mm. The laser system used in this study was manufactured by IPG photonics Corporation, headquartered in Marlborough, Massachusetts, United states. The material being used was Aluminum 6061 with a 2 mm thickness. A series of continuous, sinusoidal, and cosinusoidal laser pulses were used to create laser spots on the material. The surface was brushed prior to welding to remove contaminants and prevent oxidation. Due to aluminum's high reflectivity, a 7.5 degree deviation was applied to the laser head to avoid damaging the welding head. The thermal properties of aluminum 6061 are listed in Table 4.1.

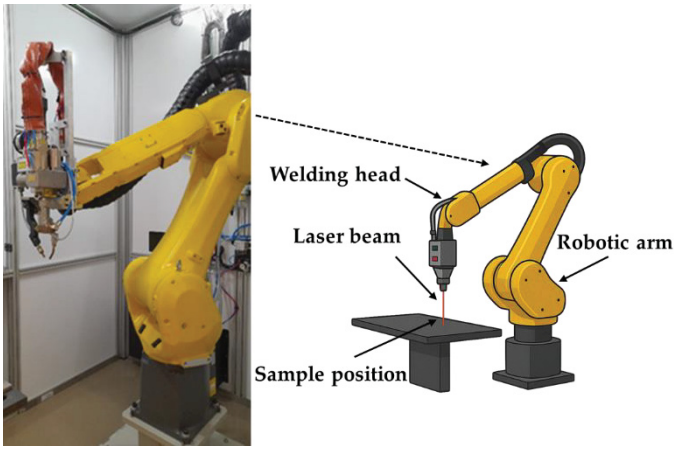

(a) (b)

Figure 4.1 Experimental setup of the laser welding system: (a) laser source (IPG YLS-6000: Ytterbium Laser), (b) laser welding head and components

Table 4.1 Thermophysical properties of 6061-T6 aluminum alloy
Adapted from Cai et al., (2025), Zhang et al., (2014), Wen at al., (2021)

Property	**Symbol**	**Magnitude**
Solidus temperature	T_s	873.13 (K)
Liquidus temperature	T_l	915.15 (K)
Vaporization temperature	T_V	2760 (K)
Thermal conductivity of solid	k_s	235 (W/m/K)
Thermal conductivity of liquid	k_l	90 (W/m/K)
Density of solid	ρ_s	2660 (kg/m^3)
Density of liquid	ρ_l	2380 (kg/m^3)
Latent heat of melting	L_m	3.87×10^5 (J/kg)
Latent heat of vaporization	L_V	1.05×10^7 (J/kg)
Specific heat capacity of solid	$C_{p,s}$	870 (J/kg/K)
Specific heat capacity of liquid	$C_{p,l}$	1170 (J/kg/K)
Convective heat transfer coefficient	h	20 (W/m^2/K)
Coefficient of linear thermal expansion	β	2.8×10^{-5} (1/K)
Dynamic viscosity	μ	1.3×10^{-3} (Pa.s)
Coefficient of Surface tension	σ	$0.95 \times (1 + 0.13 \times (1 - T/T_m))^{1.67}$ (N/m)
Temperature-dependent surface tension coefficient	$\partial\sigma/\partial T$	-0.15×10^{-3} (N/m/K)
Radiation emissivity	ξ	0.2

4.3 Methods and Configurations

Laser spot welding was simulated using a 2D axisymmetric model in COMSOL Multiphysics 5.6, justified by the rotational symmetry of the stationary laser beam around the vertical z-axis. This setup allowed for efficient representation of 3D behavior via symmetry. This study investigated the pulse modulation impact by applying sinusoidal and cosinusoidal laser power distributions, focusing on keyhole stability and overall welding efficiency. The study applied sinusoidal and cosinusoidal laser power profiles to examine their impact on keyhole stability and welding efficiency. The computational domain and power profiles are shown in Figure 4.2. Boundaries ABGF and EGCD represent air and aluminum, respectively. A Gaussian beam was used to model the laser heat source.

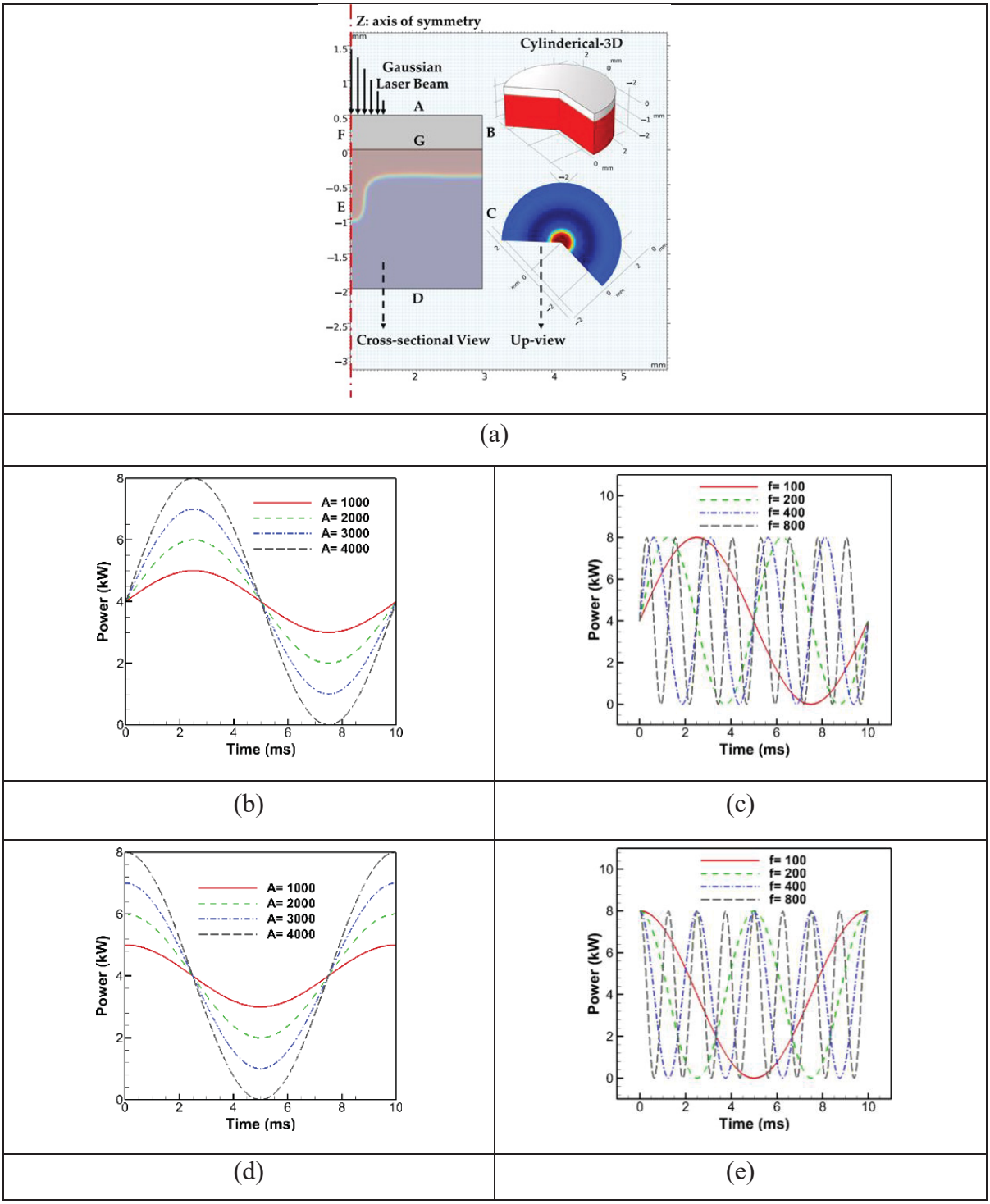

Figure 4.2 (a) Schematic 2D axisymmetric representation of numerical sample geometry and results in COMSOL Multiphysics, (b), and (c) Examples of sinusoidal power profiles under constant and variable amplitudes/frequencies, (d), and (e) Examples of cosinusoidal power profiles under constant and variable amplitudes/frequencies

4.3.1 Heat and Fluid Dynamics

A detailed description of the numerical methods, governing equations, and mesh sensitivity analysis used in this study is available and verified in our previous publications (SaediArdahaei & Pham, 2024a, 2024b). A brief summary is provided here, as the focus is on developing and applying a novel optimization technique. The modified level set (LS) method (Olsson & Kreiss, 2005), modified mixture theory (MMT) (Kong & Kovacevic, 2010; SaediArdahaei & Pham, 2024a), and the thermal enthalpy porosity technique (TEPT) (Ardahaie et al., 2019; Y. Zhang et al., 2014) were used to model multiphase interactions during laser welding. These models were employed due to their proven effectiveness in dealing with phase transformations, keyhole morphology, and fluid flow. These approaches effectively capture vapor/liquid interactions (via LS/MMT) and solid/liquid interactions (via MMT/TEPT), ensuring reliable simulation results. MMT also facilitates finite element calculations across multi-phase elements applying mixture effects (Kong & Kovacevic, 2010; SaediArdahaei & Pham, 2024a). The model incorporated recoil pressure, surface tension forces, Darcy damping force, evaporation and mass loss, buoyancy, and surface dynamics. The numerical framework of this study was based on several assumptions to simplify the complex multiphase simulation: (a) Newtonian, incompressible laminar flow; (b) temperature-independent thermophysical properties; (c) mushy zone as a porous medium (SaediArdahaei & Pham, 2024b); (d) neglecting multiple beam reflections; and (e) treating vaporized material as an ideal gas. The transport phenomena across all phases were modeled by solving the modified forms of energy (Equation (4.1)), mass (Equation (4.2)), and momentum (Equation (4.3)) conservation equations, and the LS (Equation (4.4)) equation.

$$\rho C_p \frac{\partial T}{\partial t} + \rho C_p \vec{u} \cdot \nabla T = \nabla \cdot (k \nabla T) + (q_{Laser} - Q_{vapor})\, \delta(\phi) \tag{4.1}$$

$$\nabla \cdot \vec{u} = \delta(\phi) \dot{m}_{H-L} \left(\frac{\rho_l - \rho_v}{\rho^2} \right) \tag{4.2}$$

$$\rho \left(\frac{\partial \vec{u}}{\partial t} + (\vec{u} \cdot \nabla)\vec{u} \right) = \nabla \cdot [-pI + \mu(\nabla \vec{u} + (\nabla \vec{u})^T)]) + \rho \vec{g} - \rho_l \beta_l (T - T_m) \vec{g} \phi - \mu_l K \vec{u} + (\gamma \vec{n} k - \nabla_s \gamma) \delta(\phi) \tag{4.3}$$

$$\frac{\partial \phi}{\partial t} + \vec{u} \cdot \nabla \phi - \delta(\phi)\dot{m}_{H-L}\left(\frac{V_{f,1}}{\rho_v} + \frac{V_{f,2}}{\rho_l}\right) + \gamma_{ls}\nabla \cdot \left(\phi(1-\phi)\frac{\nabla \phi}{|\nabla \phi|} - \epsilon_{ls}\nabla \phi\right) = 0 \qquad (4.4)$$

The energy equation (Equation (4.1)) includes the velocity vector $\vec{u}$, specific heat capacity Cp, temperature T, thermal conductivity k, and time t. The laser energy heat source q_{laser} is defined as $(2\alpha P_{Laser}/\pi R_{eff}^2)\, exp\,(-2r^2/R_{eff}^2)B_t$ where P_{Laser} is the peak laser power, B_t is the analytic pulse-shaping function, α is the aluminum absorptivity, and R_{eff} is the effective beam radius. Energy loss due to evaporation, Q_{vapor}, is calculated as $-L_V \dot{m}_{H-L}$, where L_V is the latent heat of vaporization and $\dot{m}_{H-L}$ refers to the mass loss due to evaporation, defined as $(1-\beta_r)\sqrt{M/2\pi R}\,(P_{sat}(T)/\sqrt{T})$. The saturated vapor pressure P_{sat} is determined by $P_{atm}\, exp[(1-(T_v/T))\, ML_v/RT_v]$ (Mayi et al., 2020). Here, β_r is the retro-diffusion coefficient, R the universal gas constant, and M the molar mass of vaporized particles. A delta function $\delta(\phi)$, characterized using the LS variable ϕ, applies the laser heat flux and energy loss due to evaporation only at the vapor/liquid interface (where $\phi = 0.5$). Equation (4.2) represents the modified mass conservation equation incorporating a source term to add the impact of recoil pressure (Courtois et al., 2014; Y. Zhang et al., 2014). Equation (4.3) represents the momentum conservation, including the dynamic viscosity μ, pressure and viscous stresses, gravity, buoyancy, Darcy damping, and surface tension forces. The Darcy drag coefficient K, is defined with a relation as $((180/d^2)(1-V_l)^2)/({V_l}^3 + b))$, with d, the dendrite size constant set to 10^{-2} cm (Pang et al., 2011), and b, the constant used to avoid division by zero. β_l and $(\nabla \vec{u})^T$ are the volume thermal expansion coefficient and the transpose of velocity vector gradient. V_l is the liquid volume fraction, assigned to one above the liquidus temperature, zero below the solidus temperature, and $(T-T_s)/(T_l-T_s)$ between the two (Ardahaie et al., 2019, 2021; Pahamli et al., 2022). Equation (4.4) is the modified LS equation, improved by adding a gas dynamic source term to model vaporization effects due to mass loss and vapor pressure at the vapor/liquid interface (Olsson & Kreiss, 2005). Parameters γ_{ls} and ϵ_{ls} are the reinitialization and the interface thickness values, respectively, set based on sensitivity analysis (SaediArdahaei & Pham, 2024a). $V_{f,1}$ and $V_{f,2}$ denote the gas and solid/liquid volume fractions.

4.4 Optimization Approach

The Taguchi-based GRA was performed to optimize the numerical data from cosinusoidal and sinusoidal power profiles for enhancing keyhole laser welding performance on aluminum.

4.4.1 Taguchi Design

The Taguchi method enhances product quality through system, parameter, and tolerance design strategies. This study adopted parameter design, focusing on identifying robust parameter settings through controlled experimentation. An orthogonal array (OA) was used to structure the experimental layout, minimizing the number of simulations. The selection of OA was guided by computational cost, time constraints, and study objectives (Pakrouh et al., 2015). The total degrees of freedom (DOF) of the experiment are defined in Equation (4.5).

$$DOF_{experiment} = \sum DOF_{factor} + \sum DOF_{interactions} \tag{4.5}$$

Table 4.2 lists the factors and levels used in the Taguchi design. The interaction DOF between two factors was calculated as the product of their individual DOFs, where each factor's individual DOF was one unit less than its number of levels.

Table 4.2 Investigated Factors and levels

Symbol	Parameters	Levels			
		1	2	3	4
A	Pulse Shape	Sinusoidal	Cosinusoidal	N/A	N/A
B	Frequency (Hz)	100	200	400	800
C	Amplitude (W)	1000	2000	3000	4000

This study considered three factor interactions: $A \times B, A \times C$, and $B \times C$. The total DOF yielded $[(2-1)+2\times(4-1)]_{DOF_{factor}} + [2\times(1\times 3)+(3\times 3)]_{\sum DOF_{interactions}} = 22$. A

suitable OA must have a DOF equal to or greater than this value. Accordingly, an L_{32} OA was selected to fully capture all main and interaction effects influencing the keyhole welding process, as shown in Table 4.3.

Table 4.3 Chosen L32 mixed OA values

Experiments	A	B	C
1	1	1	1
2	1	1	2
3	1	1	3
4	1	1	4
5	1	2	1
6	1	2	2
7	1	2	3
8	1	2	4
9	1	3	1
10	1	3	2
11	1	3	3
12	1	3	4
13	1	4	1
14	1	4	2
15	1	4	3
16	1	4	4
17	2	1	1
18	2	1	2
19	2	1	3
20	2	1	4
21	2	2	1
22	2	2	2
23	2	2	3
24	2	2	4
25	2	3	1
26	2	3	2
27	2	3	3
28	2	3	4
29	2	4	1
30	2	4	2
31	2	4	3
32	2	4	4

4.4.2 Grey Relational Analysis (GRA)

The primary objective of this study was to optimize the welding process by minimizing keyhole instability. Our previous work confirmed that large fluctuations in surface tension, Darcy damping force, and velocity significantly increase the likelihood of keyhole collapse by promoting instability (SaediArdahaei & Pham, 2024b). Additionally, parameters such as mean temperature, keyhole depth, and width are critical for ensuring mechanical integrity and welding efficiency. Therefore, a multi-response optimization technique was developed to simultaneously account for these key parameters and their desired behaviors.

4.4.2.1 Grey Relational Analysis (GRA): Formulation

The GRA approach is a technique that takes into account all the responses, and combines them into one particular response by transforming them into Grey relational grades (GRGs) (Omoniyi et al., 2025; Tsai & Wu, 2022). This study aimed to optimize desirable responses such as keyhole depth, width, and mean temperature, while minimizing relative standard deviations (RSDs) of the Darcy damping force, surface tension, and velocity as key contributors to instability. The response objectives are summarized in Table 4.4. Preprocessing involved converting the raw data into a comparable format. The equations for calculating the standard deviation (SD) and RSD of the fluctuating forces and velocity are shown in Equations (4.6) and (4.7). The GRG computation followed three steps: normalization, Grey relational coefficient (GRC) calculation, and final GRG evaluation, with normalization performed using either Equation (4.8) or Equation (4.9), depending on the objective type being chosen as 'larger-the-better' or 'smaller-the-better' (Kuo et al., 2008).

$$SD_j^{(i)} = \sqrt{1/n \sum_{t=1}^{n} (x_j^{(i)}(t) - \bar{x}_j^{(i)})^2} \tag{4.6}$$

$$RSD_j^{(i)} = (SD_j^{(i)} / \bar{x}_j^{(i)}) \times 100 \tag{4.7}$$

$$X_{ij}{}^{*} = (X_{ij} - \min(X_j)/(\max X_j - \min X_j) \quad (4.8)$$

$$X_{ij}{}^{*} = (\max X_j - X_{ij})/(\max X_j - \min X_j) \quad (4.9)$$

In Equations (4.6) and (4.7), $x_j^{(i)}(t)$ denotes the time-dependent value of the j-th response (e.g., surface tension, Darcy damping force) for the i-th test at time step t, and $\bar{x}_j^{(i)}$ represents its mean over all n = 1000 simulation steps sampled from t = 0 to t = 0.1 s. In Eqs. 4.8 and 4.9, X_{ij} and $X_{ij}{}^{*}$ are the original and normalized values of the j-th response of the i-th test. X_j is defined as a set of all values of the j-th response across all 32 experiments or test cases ($X_j = \{X_{1j}, X_{2j}, \ldots X_{32j}\}$). All the response values were scaled into [0, 1] using these equations (Equations (4.8) and (4.9)).

Table 4.4 Chosen responses for the optimization technique

Parameter	Objective	Reason
Keyhole depth/width	Higher the better	Deeper welds
Mean temperature	Smaller the better	less overall material heat exposure
RSD of Darcy damping force RSD of surface tension force RSD of velocity	Smaller the better	Reduced variability of parameter over time Fewer fluctuations; less instability

The next steps are devoted to calculating the deviation from the ideal normalized value and the GRC, which are shown in Equations (4.10) and (4.11) (Kuo et al., 2008). Finally, the GRG can be calculated using Equation (4.12).

$$\Delta_{ij} = \left|X_{ij}{}^{*,ideal} - X_{ij}{}^{*}\right| \quad (4.10)$$

$$GRC_{ij} = (\Delta_{min} + \xi\Delta_{max})/(\Delta_{ij} + \xi\Delta_{max}) \quad (4.11)$$

$$GRG_i = (1/m)\sum_{j=1}^{m} GRC_{ij} \quad (4.12)$$

where Δ_{ij} denotes the deviation of the normalized response from the ideal normalized response (typically taken as 1), while Δ_{min} and Δ_{max} represent the minimum and maximum possible deviations, usually set to 0 and 1. The distinguishing coefficient ξ, ranging from 0 to 1, was set to 0.5 for stability (Kuo et al., 2008; Omoniyi et al., 2025). In Equation (4.12), m is the total number of responses considered in this analysis (here, m=8).

4.4.2.2 Analysis of Variance (ANOVA)

The performance of the tests, factors, and levels in the Taguchi method was analyzed using a statistical measurement approach known as ANOVA. This quantified the contribution of each factor, their main effects, interactions, and associated errors on the overall response. Since the optimization data were obtained from single-run numerical simulations, standard ANOVA was applied without considering noise factors. The analysis assessed the statistical significance of each factor on the optimized response, represented by the grey relational grade (GRG).

4.4.3 System, Software and Calculation Details

COMSOL Multiphysics 5.6 was used for simulations on a Lenovo ThinkStation P720 equipped with an Intel® Xeon® Gold 5118 CPU (12 cores, 24 threads) and 128 GB RAM. The CPU was produced by Intel corporation, based in Santa Clara, California, USA. The system was assembled by LENOVO, headquartered in Beijing, China. Three physics interfaces, including Heat Transfer in Fluids, Laminar Flow, and Level Set, were employed and coupled using the Non-Isothermal Flow and Two-Phase Flow interfaces. These ensured accurate modeling of three-phase phenomena by linking the heat transfer, fluid flow, and level set dynamics. A time step of 10 μs was used, with an extra-fine mapped mesh (0.02 mm quadrilateral elements) optimized for fluid dynamics. PARDISO solvers were applied: a nested dissection multithreaded version for fluid flow and an automatic preordering version for the Heat Transfer and LS equations. The optimal interface thickness and reinitialization parameter for the Level Set method were set to 5 m/s and 0.03 mm, respectively, ensuring better computational

efficiency. All mathematical calculations related to the optimization technique were performed using Microsoft Excel.

4.5 Results and Discussion

This section presents the experimental and numerical results, optimization outcomes, and ANOVA analysis for laser spot welding on aluminum using sinusoidal and cosinusoidal power profiles. Eight key criteria were used to guide the optimization, with emphasis on minimizing keyhole instabilities and enhancing penetration depth and width. Parameters such as the mean temperature, RSDs of surface tension and Darcy damping forces, maximum fluid velocity, and keyhole geometry were analyzed to determine the optimal welding conditions.

4.5.1 Experimental Results and Validation

The effects of the sinusoidal and cosinusoidal laser power profiles were evaluated against the conventional continuous profile through laser spot welding trials. Cross-sectional and top-view images (Figures 4.3 and 4.4) illustrate that both the weld depth and width increased with modulated profiles. Specifically, the depth and width increased from 0.755 mm and 1.788 mm (continuous) to 0.900 mm and 1.985 mm (cosinusoidal, 2000 W amplitude), and further to 1.119 mm and 2.011 mm (sinusoidal, 2000 W amplitude). Moreover, increasing the amplitude from 1000 W to 2000 W at 100 Hz further enhanced the weld geometry. For the cosinusoidal profiles, the depth and width increased from 0.781 mm and 1.874 mm to 0.900 mm and 1.985 mm; for the sinusoidal profiles, they increased from 0.813 mm and 1.890 mm to 1.119 mm and 2.011 mm.

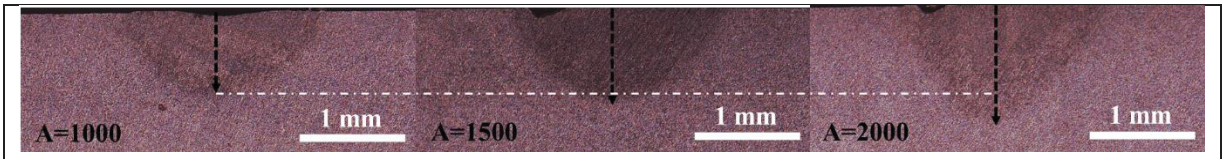

(a) Sinusoidal laser power profile

(b) Continuous laser power profile

(c) Cosinusoidal laser power profile

Figure 4.3 Cross-sectional view of the samples under different laser power profiles using an identical total laser energy of 40 j (4kW over 10 ms) for (a) sinusoidal laser power profile under various laser power amplitudes, (b) continuous laser power profile, and (c) cosinusoidal laser power profile under various laser power amplitudes

Figure 4.4 presents top-view images of the laser spots under different power profiles. The weld width increased with both sinusoidal and cosinusoidal profiles and further widened with higher power amplitudes compared to the continuous mode. These results confirm the superiority of modulated profiles in achieving greater depth-to-width ratios using the same total laser energy.

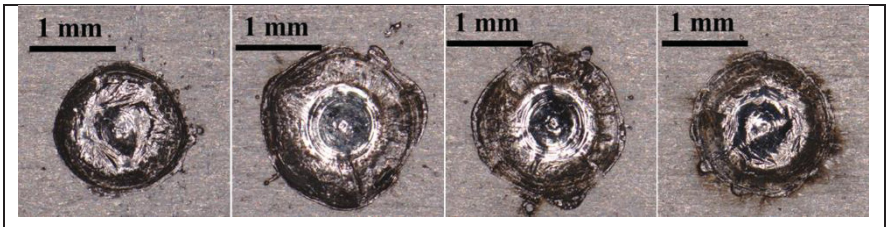

(a) CW versus sinusoidal laser power profile

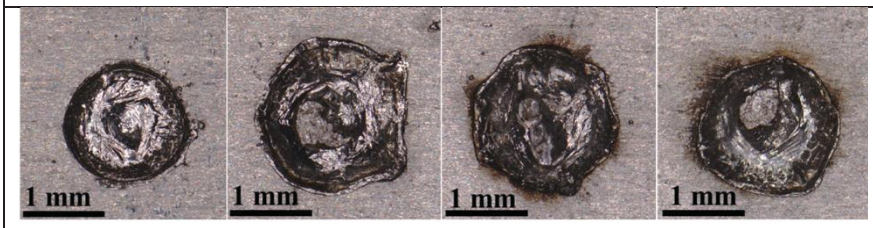

(b) CW versus cosinusoidal laser power profile

Figure 4.4 Top view of the laser spots produced under CW and sin/cosinusoidal laser power profiles for (a) comparison of CW with sinusoidal laser power profiles with varying laser power amplitudes (left to right: CW, Sin: A=2000, 1500, 1000) and (b) comparison of CW with cosinusoidal laser power profiles with varying laser power amplitudes (left to right: CW, Cos: A=2000, 1500, 1000)

The numerical simulation was validated by comparing the simulated weld width and depth with the experimental results for three cases: the sinusoidal, cosinusoidal (100 Hz, 2000 W), and continuous power profiles. As shown in Figure 4.5, the simulated keyhole and molten pool dimensions closely matched the experimental measurements, with minimal error. This strong agreement confirms the reliability of the simulation approach in accurately predicting weld geometry and keyhole behavior.

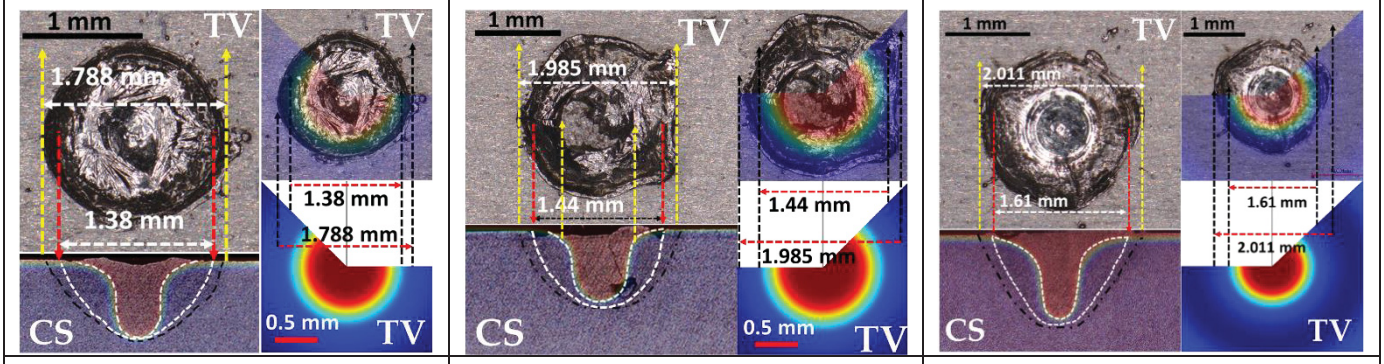

Continuous	Cosinusoidal	Sinusoidal

Figure 4.5 The numerical and experimental results of the top view and cross-section comparisons for (a) CW, (b) cosinusoidal (A=2000, f=100), and (c) sinusoidal (A=2000, f=100); the black dashed lines in the cross-section images represent the weld zone and HAZ while the white dashed lines represent the numerically-derived weld zone and keyhole lines; CS is short for cross-section view and TV is the top view

4.5.2 Numerical Results and Optimization Procedures

Following the confirmed improvements in weld geometry using the sinusoidal and cosinusoidal profiles, the numerical study was extended to explore various frequencies and amplitudes under a constant total laser energy of 40 J for consistency. Using the Taguchi method (Tables 4.2 and 4.3), 32 simulations were performed. GRA and ANOVA were applied to determine the optimal welding parameters. The numerical results for the eight optimization criteria are summarized in Table 4.5 and Figure 4.6, with GRA-related and ANOVA data presented in Tables 4.6, and 4.7.

Table 4.5 The obtained results of tests for eight response variables under varying frequencies and amplitudes (RSD $Sur_{r,z}$: RSD of surface tension in the radial or axial direction)

Test	Keyhole Depth (mm)	Keyhole Width (mm)	RSD Velocity (%)	Mean Temp (K)	RSD $Darcy_r$ (%)	RSD $Darcy_z$ (%)	RSD Sur_r (%)	RSD Sur_z (%)
1	0.793	1.500	46.9	2682	62.4	56.8	42.4	23.1
2	0.930	1.610	53.2	2403	58.0	72.0	54.8	36.9
3	1.067	1.670	56.8	2112	74.4	62.6	62.0	39.8
4	1.218	1.728	52.8	1941	77.8	62.2	67.1	39.5
5	0.852	1.434	44.9	2684	60.3	52.5	35.3	22.3
6	0.951	1.516	48.8	2439	58.7	63.4	48.9	34.9
7	1.008	1.580	53.3	2152	71.5	58.0	54.4	38.9
8	1.116	1.616	47.9	1995	78.4	58.2	57.8	38.9
9	0.848	1.384	46.4	2692	58.5	42.8	27.0	23.0
10	0.880	1.446	54.4	2543	63.2	55.6	43.8	28.6
11	0.945	1.488	62.4	2298	62.9	57.3	50.9	36.7
12	0.997	1.508	59.8	2135	75.2	55.4	53.0	37.6
13	0.784	1.350	53.9	2698	56.9	39.8	23.6	27.4
14	0.777	1.396	58.2	2665	59.1	46.9	35.6	26.8
15	0.801	1.444	54.5	2531	67.4	59.2	46.5	28.7
16	0.886	1.502	62.0	2358	67.2	59.9	50.0	31.1
17	0.754	1.350	30.6	2695	53.3	45.7	28.2	23.7
18	0.776	1.436	29.5	2382	54.1	49.8	51.2	35.7
19	0.857	1.474	29.5	2114	73.4	43.9	56.5	34.5
20	0.984	1.514	32.2	1948	75.1	41.7	59.7	33.5
21	0.762	1.404	42.8	2697	55.0	40.5	29.9	25.0
22	0.784	1.492	44.6	2444	56.4	56.3	49.0	34.1
23	0.881	1.536	52.0	2162	73.5	49.8	56.2	36.5
24	1.062	1.576	54.1	1999	73.4	48.3	60.9	35.0
25	0.810	1.396	45.2	2697	53.4	39.6	26.7	21.8
26	0.903	1.442	53.0	2548	59.6	55.0	43.8	27.1
27	0.995	1.496	62.2	2293	69.4	57.4	52.8	35.7
28	1.076	1.528	64.6	2125	74.2	58.5	57.7	37.4
29	0.839	1.360	54.6	2689	51.2	41.2	25.0	25.8
30	0.863	1.380	58.7	2641	54.4	48.4	39.9	24.8
31	0.882	1.420	57.4	2505	63.1	61.8	49.8	27.8
32	0.931	1.466	62.4	2344	66.4	57.9	51.6	32.2

Table 4.6 GRC of the response variable results, their corresponding GRG for each test, and the rank performance (RSD $Sur_{r, z}$: RSD of surface tension in the radial or axial direction)

Test	GRC								GRG	Rank
	Keyhole Depth	Keyhole width	RSD Velocity	Mean Temp	RSD $Darcy_r$	RSD $Darcy_z$	RSD Sur_r	RSD Sur_z		
1	0.35	0.45	0.50	0.34	0.55	0.48	0.54	0.88	0.511	15
2	0.45	0.62	0.43	0.45	0.67	0.33	0.41	0.37	0.465	24
3	0.61	0.77	0.39	0.69	0.37	0.41	0.36	0.33	0.491	17
4	1.0	1.00	0.43	1.00	0.34	0.42	0.33	0.34	0.607	5
5	0.39	0.39	0.53	0.34	0.60	0.56	0.65	0.95	0.551	11
6	0.46	0.47	0.48	0.43	0.64	0.41	0.46	0.41	0.470	21
7	0.52	0.56	0.42	0.64	0.40	0.47	0.41	0.34	0.472	20
8	0.69	0.63	0.49	0.88	0.33	0.47	0.39	0.34	0.527	14
9	0.39	0.35	0.51	0.34	0.65	0.86	0.86	0.88	0.605	7
10	0.41	0.40	0.41	0.39	0.53	0.50	0.52	0.57	0.466	23
11	0.46	0.44	0.35	0.51	0.54	0.48	0.44	0.38	0.449	27
12	0.51	0.46	0.37	0.66	0.36	0.51	0.43	0.36	0.457	26
13	0.35	0.33	0.42	0.33	0.71	0.99	1.00	0.62	0.592	8
14	0.34	0.36	0.38	0.34	0.63	0.69	0.64	0.64	0.505	16
15	0.36	0.40	0.41	0.39	0.46	0.45	0.49	0.57	0.440	32
16	0.41	0.46	0.35	0.48	0.46	0.44	0.45	0.49	0.443	31
17	0.33	0.33	0.94	0.33	0.87	0.73	0.83	0.83	0.649	2
18	0.34	0.39	1.00	0.46	0.83	0.61	0.44	0.39	0.559	10
19	0.39	0.43	1.00	0.69	0.38	0.79	0.4	0.41	0.561	9
20	0.45	0.47	0.87	0.98	0.36	0.89	0.38	0.43	0.609	4
21	0.34	0.37	0.57	0.33	0.78	0.95	0.77	0.74	0.607	6
22	0.35	0.44	0.54	0.43	0.72	0.49	0.46	0.42	0.482	19
23	0.41	0.50	0.44	0.63	0.38	0.61	0.40	0.38	0.468	22
24	0.6	0.55	0.42	0.87	0.38	0.65	0.37	0.40	0.530	13
25	0.36	0.36	0.53	0.33	0.86	1.00	0.88	1.00	0.666	1
26	0.42	0.40	0.43	0.38	0.62	0.51	0.52	0.63	0.489	18
27	0.51	0.45	0.35	0.52	0.43	0.48	0.43	0.39	0.444	29
28	0.62	0.49	0.33	0.67	0.37	0.46	0.39	0.37	0.462	25
29	0.38	0.34	0.41	0.34	1.00	0.91	0.94	0.69	0.626	3
30	0.40	0.35	0.38	0.35	0.81	0.65	0.57	0.75	0.532	12
31	0.41	0.38	0.39	0.40	0.53	0.42	0.45	0.60	0.448	28
32	0.45	0.42	0.35	0.48	0.47	0.47	0.44	0.46	0.443	30

Table 4.7 Results of ANOVA analysis (contribution was calculated as (Adj SS of Factor/total Adj SS) × 100).

Analysis of Variance						
Source	**DF**	**Adj SS**	**Adj MS**	**F-Value**	**P-Value**	**Contribution (%)**
Amplitude	3	0.076427	0.025476	111.28	0	51.9
Pulse Shape	1	0.008454	0.008454	36.93	0	5.7
Frequency	3	0.015007	0.005002	21.85	0	10.2
Frequency × Amplitude	9	0.035032	0.003892	17	0	23.8
Pulse Shape × Amplitude	3	0.005416	0.001805	7.89	0.007	3.7
Pulse Shape × Frequency	3	0.004968	0.001656	7.23	0.009	3.4
Error	9	0.00206	0.000229			
Total	31	0.147366				

4.5.2.1 Keyhole Depth and Width

Analysis of Table 4.5 shows that the keyhole depth was primarily influenced by the laser power amplitude, with pulse frequency and shape having secondary effects. Increasing the amplitude consistently deepened the keyhole across all profiles. For example, at 100 Hz with sinusoidal pulses, raising the amplitude from 1000 W to 4000 W increased depth by the 54% (0.793 mm to 1.218 mm). A similar trend occurred for other frequencies (Figure 4.6), though the magnitude of the depth increase diminished at higher frequencies (e.g., 800 Hz). Physically, at lower frequencies, longer pulse durations allowed high-amplitude peaks to deliver sustained energy, resulting in deeper keyholes. In contrast, at 800 Hz, where each pulse lasted approximately 1.25 ms, the shorter duration limits the energy delivered per pulse, reducing the effectiveness of higher peak power in increasing depth. Frequency alone had a mild impact on the depth at low amplitudes but showed a stronger effect at higher amplitudes. For instance, sinusoidal depth dropped by 27%, with increasing frequency from 100 Hz to 800 Hz at 4000 W. Cosinusoidal depth also declined but less significantly (5%). This suggests a strong interaction between frequency and amplitude, which is important for optimization. Overall, frequencies 100 to 400 Hz yielded comparable depths (around 0.9–1.0 mm at mid-to-high amplitudes), with a notable drop at 800 Hz. The slight decline in depth with very high

frequency can be attributed to reduced energy per pulse and rapid cycling, which prevented the keyhole from fully developing before the pulse ended. The pulse shape had a subtle yet frequency-dependent influence on penetration. On average, sinusoidal pulses yielded slightly deeper welds (0.928 mm vs. 0.885 mm). At 100 Hz and 4000 W, the sinusoidal profiles produced 24% deeper penetration than the cosinusoidal profiles (1.218 mm vs. 0.984 mm), likely due to their gradual power increase, which facilitated stable keyhole formation before delivering the peak energy, enhancing penetration. Conversely, at 800 Hz, cosinusoidal pulses outperformed the sinusoidal pulses (0.931 mm vs. 0.886 mm), as early power peaks became more effective during brief pulse durations. Overall, frequencies between 100 and 400 Hz at mid-to-high amplitudes provided the most consistent depth performance.

The keyhole width followed trends similar to the depth but showed smaller relative variations. Higher amplitudes slightly increased the width; for example, at 100 Hz, sinusoidal pulses widened the keyhole from 1.50 mm to 1.73 mm (15% increase), compared to a 54% increase in depth. The width generally decreased with higher frequencies. Sinusoidal pulses at 100 Hz produced the widest melt pools (≈1.5 mm at low amplitude), while 800 Hz pulses yielded narrower widths (≈1.35 mm). This trend reflects the effects of longer, more energetic pulses promoting lateral heat diffusion, whereas high-frequency pulsing concentrated energy locally.

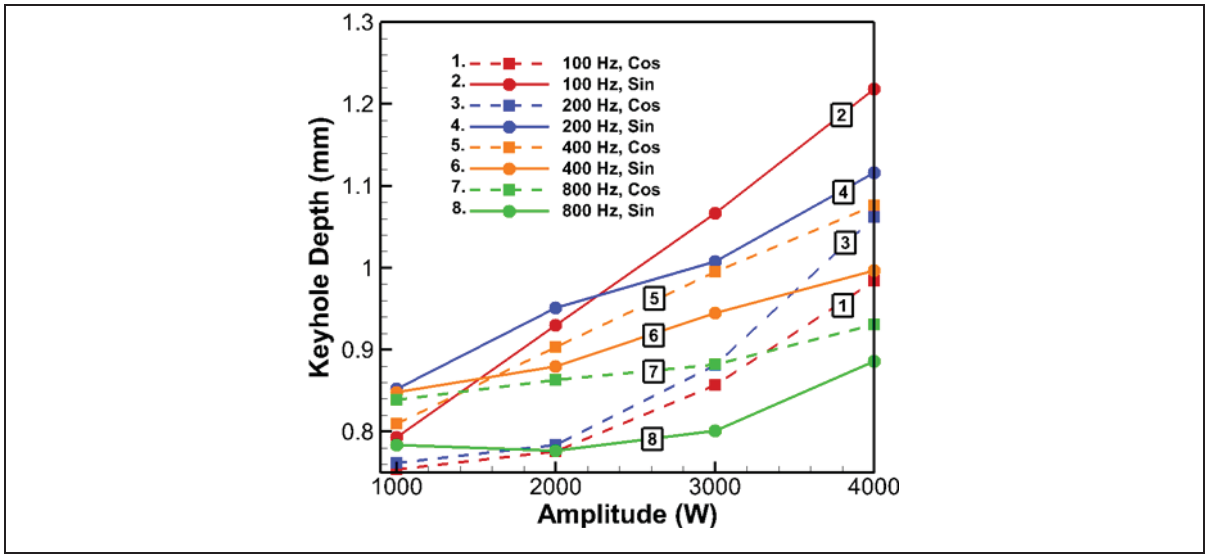

Figure 4.6 Keyhole depth versus amplitude at different frequencies for sinusoidal and cosinusoidal laser profiles

4.5.2.2 Thermal Response (Mean Temperature)

The mean material temperature showed a clear dependence on the pulse parameters. An increasing amplitude consistently reduced the mean temperature across all frequencies. For example, with sinusoidal pulses at 100 Hz, the mean temperature dropped from 2682 K at an amplitude of 1000 W to 1941 K at an amplitude of 4000 W. Similar reductions (≈500–600 K) were observed for cosinusoidal pulses and at other frequencies (Table 4.5). This inverse relationship is attributed to higher amplitude pulses causing intense but brief heating, followed by longer cooling periods, which lowers the time-averaged temperature. Thus, higher amplitudes not only enhanced penetration but also promoted lower mean temperatures, which may benefit heat-sensitive materials. Conversely, higher frequencies increased the mean temperature by reducing the time between pulses and promoting more continuous energy input. The pulse shape had a negligible direct impact on the mean temperature, which was expected since shape altered the temporal distribution within a pulse but not the overall energy per pulse in these tests.

4.5.2.3 Process Stability and Fluctuations (Velocity and Forces)

Table 4.5 reveals that the pulse parameters significantly influenced process stability. Amplitude was the primary contributor to instability, with increased values consistently raising the relative standard deviation (RSD) of key forces. For instance, increasing the amplitude from 1000 W to 4000 W more than doubled the RSD of surface tension force on average (from ~30% to ~57%). Physically, a larger amplitude means higher peak power, causing stronger vapor recoil pressure and fluid flow surges during the pulse peak, followed by a low-power period producing a violent stirring of the melt pool, leading to greater variability. Pulse frequency had a dual effect. Higher frequencies generally reduced the RSDs of surface tension and Darcy damping forces (e.g., averaging over shapes, radial surface tension RSD dropped from 52.7% at 100 Hz to 40.3% at 800 Hz), likely due to more frequent but smaller perturbations. However, the RSD of fluid velocity increased with frequency, from ~41% at 100 Hz to ~58% at 800 Hz (averaging over shapes) as rapid pulsing kept the molten pool in

continuous motion, preventing flow stabilization. These frequency effects highlight that different aspects of the process responded differently to the pulse rate: the instantaneous flow became more vigorous with fast repetition, yet the forces driving or resisting that flow might have fluctuated less extremely due to the more continuous application. Pulse shape also played a role in stability, especially at low frequencies. At 100 Hz and 4000 W, cosinusoidal pulses significantly outperformed sinusoidal ones: the velocity RSD was 32.2% vs. 52.8%, the Darcy force RSD (z) was 41.7% vs. 62.2%, and the radial surface tension RSD was 59.7% vs. 67.1%. This may be due to the cosinusoidal profile delivering peak power at the start of the pulse, followed by a gradual decline, allowing oscillations to settle before the next pulse. In contrast, sinusoidal pulses sustained excitation longer, promoting inter-pulse oscillations. However, the stabilizing advantage of the cosinusoidal profiles diminished at higher frequencies. By 400 Hz and 800 Hz, differences between the two shapes became negligible or even reversed slightly. For example, at 800 Hz and 4000 W, the radial surface tension RSD was 51.6% for cosinusoidal and 50.0% for sinusoidal pulses. Consequently, shape–frequency interaction was important in the optimization procedure. Additionally, radial fluctuations were consistently higher than axial ones under the same conditions, indicating that lateral oscillations (widening/narrowing) of the keyhole and melt pool were more pronounced than vertical (depth) fluctuations.

4.5.3 GRA and ANOVA

To evaluate the overall welding behavior across all eight response variables, the GRA was conducted on the 32 Taguchi-designed trials. Each response was first normalized according to its objective functions specified in Table 4.4. The GRA analysis and the corresponding ANOVA results are presented in this section.

4.5.3.1 Response Table for GRG

The GRC for each response (Table 4.6) was averaged to obtain the GRG for each trial, serving as an overall performance index. Higher GRG values corresponded to deeper and wider welds

with reduced fluctuations, instabilities, and thermal load. The GRG values ranged from approximately 0.44 (lowest quality) to 0.67 (highest quality), indicating significant variation in weld quality across different pulsing conditions.

The GRG-based performance ranking reveal clear trends related to pulse shape, frequency, and amplitude. As shown in Table 4.6, the highest GRG (0.666) was obtained for Test 25 (cosinusoidal, 400 Hz, 1000 W), followed by Test 17 (cosinusoidal, 100 Hz, 1000 W, GRG = 0.649) and Test 29 (cosinusoidal, 800 Hz, 1000 W, GRG = 0.626). Notably, six of the top eight tests used the lowest amplitude (1000 W), indicating that low power amplitude significantly improved the overall weld quality when all eight criteria were considered. Although lower amplitudes resulted in reduced penetration depth, this was offset by substantial improvements in process stability. Stability-related responses (e.g., velocity and force fluctuations) showed GRC values close to 1 (low variability and high stability) at low amplitudes, while high-amplitude conditions often had GRCs near 0.33 (less stability). Conversely, high amplitudes yielded higher GRCs for depth and width, but overall GRG values favored the stability benefits of lower power amplitude. Thus, GRA effectively balanced competing objectives, and the optimal performance occurred at the lowest tested amplitude. Pulse frequency also influenced weld quality. The average GRG was highest at 100 Hz (~0.557) and declined with increasing frequency. However, the top-ranked case occurred at 400 Hz, suggesting that an optimal combination of pulse shape and amplitude can compensate for the negative effects of higher frequency. This highlights the importance of interaction effects between parameters. Pulse shape had a smaller main effect compared to amplitude and frequency, but still played a role. On average, the cosinusoidal profile yielded a higher mean GRG (0.536) than the sinusoidal profile (0.504). This was especially evident at low amplitude, where early peak power in cosinusoidal pulses likely aided initial keyhole formation without destabilizing the melt pool. For example, at 100 Hz and 1000 W, the cosinusoidal case (Test 17, GRG = 0.649) significantly outperformed its sinusoidal counterpart (Test 1, GRG = 0.512), suggesting that an early power surge was beneficial at low frequency. Similar trends were observed at 400 Hz and 800 Hz. However, at higher amplitudes or when averaged across all frequencies, the shape advantage diminished. Thus, pulse shape alone had a modest effect (ranked third among the three factors), but its impact emerged in combination with frequency

and amplitude settings. Overall, amplitude had the strongest influence on GRG, followed by frequency and then shape. Lower amplitude and frequency, especially with a cosinusoidal waveform, provided the most favorable combination of weld quality and process stability. Conversely, the lowest-ranked tests often involved high frequencies and higher amplitudes with sinusoidal profiles.

4.5.3.2 ANOVA Analysis of GRG and Key Factor Effects

To evaluate the statistical significance and influence of each control factor on overall welding performance, ANOVA was conducted on the GRG results. Table 4.7 summarizes the effects of the three main factors, including pulse shape (A), frequency (B), and amplitude (C), and their two-way interactions (A×B, A×C, B×C). The analysis revealed that all three main factors and the major interactions had a significant effect on the GRG (p-values < 0.01). The error term was very small (only ~1.4% of the total variation), indicating that the chosen factors and interactions explained ~98.6% of the variability in the multi-response performance. This confirms the effectiveness of the proposed optimization design in capturing the key influences on weld quality.

Among the main factors, laser power amplitude (Factor C) had the strongest influence, accounting for 51.9% of the total GRG variation. This quantitatively confirms its dominant role, as previously observed in the GRA trends. While higher amplitudes improved penetration, they also increased melt pool turbulence, reducing the overall GRG. In contrast, lower amplitudes enhanced stability and yielded a better balance between penetration and process control, supporting the recommendation to minimize amplitude within practical limits for improved weld quality. Pulse frequency was the third most influential factor (10.2% of GRG variation), followed by pulse shape (5.7%), which also showed statistically significant effects. Cosinusoidal waveforms generally outperformed sinusoidal ones, especially at low amplitudes and frequencies, due to their early energy delivery, which promoted more stable keyhole formation. Significant interaction effects were also observed: frequency–amplitude accounted for 23.8% of GRG variation, while shape–frequency and shape–amplitude interactions contributed approximately 3–4% each. These results highlight the importance of tuning

parameter combinations rather than individual factors alone. For instance, high amplitude was more tolerable at low frequencies but led to substantial instability at high frequencies. Similarly, the benefits of cosinusoidal pulses were most pronounced under low-frequency, low-amplitude conditions, diminishing at higher frequencies.

4.6 Conclusion

This study introduced a Taguchi-based multi-response optimization approach using GRA to determine the optimal conditions for keyhole-mode laser spot welding of aluminum. The effects of a novel cosinusoidal laser power profile were evaluated alongside sinusoidal and continuous profiles. Welding performance was analyzed and optimized based on eight key response variables, including keyhole depth and width (larger-the-better), and the relative standard deviations of surface tension, Darcy damping force, and fluid velocity (smaller-the-better). The key findings are summarized as follows:

- The GRA results demonstrate that the best welding performances were achieved at a low amplitude of 1000 W (six among the top ten performances). However, increasing the amplitude to its maximum (4000 W) reached its best performance (fourth place among all) only when the frequency was set to its minimum (100 Hz).
- High-frequency and high-power amplitude pulses tend to destabilize the process and degrade the multi-objective outcome, whereas low-amplitude power, slow pulses foster stable keyhole dynamics and uniform heating, even if the penetration is lower.
- Selecting lower frequencies (100–400 Hz) is crucial for maximizing weld quality, offering adequate penetration with significantly improved process stability.
- Amplitude, frequency, and the two-way interaction between them contributed the most to the weld quality and system performance, with amplitude having the most contribution.

CONCLUSION

In this section, a comprehensive overview of key findings of this PhD project all connected to each other are highlighted, organized and presented.

The research presented in this thesis has advanced our understanding of keyhole dynamics in laser welding of aluminum. By leveraging high-fidelity numerical modeling across three complementary studies, we systematically explored how laser parameters influence keyhole formation, stability, and collapse, and how we can manipulate and mitigate these instabilities. Moreover, a multi-response optimization technique is also introduced to provide the trade off compromise to achieve the highest welding efficiency by choosing best sets of parameters to minimize instabilities with acceptable deep welds.

A major finding is that aggressive laser settings (high power density, long or frequent pulses, small beam spot size) greatly increase weld penetration depth but also push the keyhole toward instability. Under such intense conditions, the keyhole was observed to oscillate violently, increasing the possibility of collapse, which will increase probabilities of defects formation like porosity. This behavior underscores a fundamental trade-off between penetration and stability: maximizing energy input can yield deeper welds, but without careful control it also triggers fluid flow and unstable keyhole behavior that jeopardize weld integrity.

Crucially, this work identified the physical mechanisms behind these instabilities. It was found that surface tension and related curvature effects, along with the resistance of the semi-solid mushy zone (modeled as Darcy's damping), are two of the dominant forces driving keyhole fluctuations when conducting power wave modulation. These forces negatively counteract and sometimes may overpower the recoil pressure from vaporization, responsible for keeping the keyhole open, contributing to keyhole instabilities and increasing the probability of keyhole collapse and defect formation. This insight shifts the focus toward managing melt pool fluid dynamics and solidification behavior as a means to stabilize the keyhole. In practical terms,

controlling factors like how smoothly the molten walls of the keyhole are maintained (to avoid sharp curvature variations) and how quickly the melt solidifies (affecting flow damping) can be as important as controlling the laser's intensity.

Equally important, the thesis demonstrated that by intelligently modulating laser parameters one can mitigate keyhole instability while still achieving deep penetration. The studies showed that introducing the laser energy in a more gradual or controlled manner, for example, using ramp-down pulse shapes, triangular pulses, or other tailored waveforms, leads to a steadier keyhole. Such pulse profiles avoid the abrupt pressure spikes associated with square-wave (instant on/off) energy delivery, thereby preventing sudden expansions or collapses of the vapor cavity. Notably, the research identified specific modulation conditions that yield the best outcomes. For instance, using a cosinusoidal power waveform at moderate frequency and lower amplitude produced a more stable keyhole with only minimal sacrifice in penetration depth. In contrast, extremely high amplitudes or very high frequencies were shown to induce chaos in the melt pool and keyhole. This result provides a clear guideline: laser welding can be optimized by using the lowest intensity necessary to achieve penetration and by modulating that intensity in a smooth, periodic fashion rather than in harsh bursts. By following this principle, one can maintain a more constant keyhole geometry throughout the welding process, which directly translates to fewer defects.

Finally, since the keyhole mode laser welding on aluminum, is a Multiphysics problem, with highly fluctuating and competing forces and other affecting parameters, along with its original practical contribution in producing deep welds, it is shown in this thesis that a multi-response objective optimization procedure is a must in finding the best sets of parameters to not only achieve the best overall welding efficiency but also produce deep welds without jeopardizing mechanical integrity and quality of the weld. Also, the multi-response objective procedure developed in this thesis succeeded to cover more than 98 percent of the contributing factors and interactions responsible for having deep but a stable welding and high efficiencies.

The thesis also highlights the value of simulation as a tool for industry. By simulating the welding process in software like COMSOL before actual production, engineers can predict potential instability issues under different parameter sets and adjust accordingly, saving time and materials that would otherwise be spent in trial-and-error testing.

From industrial standpoint, along with additive manufacturing, various laser material processing applications can benefit from findings of this project. Any process that involves intense laser heating and material vaporization, such as laser drilling, or cutting can experience analogous cavity instabilities. For example, in laser drilling of thick plates, an unstable keyhole can cause irregular hole geometry or excessive spatter. Implementing a controlled pulse regime, by manipulating the laser power, might produce a more uniform hole by preventing sudden keyhole collapse. Similarly, in laser surface treatment, maintaining a stable melt pool (avoiding keyhole mode oscillations) could result in smoother, more uniform deposited layers. In essence, understanding the interplay of forces in the melt pool enables process engineers to tune their lasers not just for energy input, but for stability of the melting process. This represents a shift from the traditional mindset of maximizing laser power and speed, toward a more nuanced approach of maximizing quality through stability control.

RECOMMENDATIONS

Similar to many research projects, there remains many opportunities for future investigation and developments in this field. The perspectives originated from this work emphasize the importance of continuing this research to develop our understanding of keyhole dynamics, laser welding process, and instability-inducing factors, reaching to an ultimate goal of having a controlled welding process with minimized defects and maximized efficiency.

Considering limitations of our work and future avenues ahead of this complex multiphysical process, we propose the following recommendations for future researches.

- Build on this work by investigating keyhole dynamics under different conditions and materials. This includes moving beyond 2D axisymmetric models to full 3D simulations of laser welding, examining welding in motion (continuous weld seams vs. stationary spots), and studying other alloys (e.g., steels or titanium) to see how differing material properties affect instability and whether the same stabilization strategies is applicable.

- Explore new laser modulation techniques and hybrid approaches to further stabilize the keyhole. Additionally, investigating non-traditional pulse waveforms (beyond those studied in this thesis) or combining beam modulation with techniques like beam oscillation or dual-laser setups could reveal further reductions in instability.

- Prioritize further validation of numerical models with high-quality experimental data. Employ advanced diagnostics such as high-speed videography, optical coherence tomography, or in situ X-ray imaging to observe keyhole behavior in real welds. Matching these observations with simulation results will increase confidence in the models and reveal any physics that might be missing (for instance, plasma effects or multiple reflection dynamics).

- Although surface tension effects, Darcy damping forces and fluid flow behavior are presented as great contributors to keyhole and process instability, the complex nature of this multiphysical problem and the ignored physics and effects such as plasma effect, optics and multiple reflections of the laser beam within the keyhole can also further add complexity and instabilities to the process. Therefore, adding these phenomena to the current model, and inserting their effect into the multi-response optimization technique developed in this thesis will further improve and increase our chances of having minimum instabilities and defects.

- Investigate how controlling keyhole stability impacts the final weld microstructure and mechanical properties. Future research could quantitatively correlate metrics of keyhole oscillation (frequency, amplitude of fluctuations) with phenomena like grain structure, porosity distribution, or fatigue performance of the weld. This will deepen the understanding of why stability matters not just during welding, but for the integrity and performance of the finished product, thereby broadening the impact of keyhole dynamics research.

- Although COMSOL Multiphysics showed great potential in developing and executing the proposed 2D-axysimmetric model in this project, there remain doubts about its applicability and fast-responses, and good convergency trends when adapting this model for the 3D moving keyhole mode laser welding simulation. More specifically, with the fast progress in new software and modules, other new softwares such as flow-3D also show great potential in dealing with 3D transient moving laser welding. This necessitates the need for having an eye and try these new software to save calculation times and accuracy.

BIBLIOGRAPHY

Aggarwal, A., Shin, Y. C., & Kumar, A. 2024. *Unravelling keyhole instabilities and laser absorption dynamics during laser irradiation of Ti6Al4V: A high-fidelity thermo-fluidic study.* International Journal of Heat and Mass Transfer, 219, 124841.

Amara, E. H., & Fabbro, R. 2008. *Modelling of gas jet effect on the melt pool movements during deep penetration laser welding*. Journal of Physics D: Applied Physics, 41(5),

Ardahaie, S. S., Hosseini, M. J., Eisapour, M., Eisapour, A. H., & Ranjbar, A. A. 2021. *A novel porous metal hydride tank for hydrogen energy storage and consumption assisted by PCM jackets and spiral tubes*. Journal of Cleaner Production, 311, 127674.

Ardahaie, S. S., Hosseini, M. J., Ranjbar, A. A., & Rahimi, M. 2019. *Energy storage in latent heat storage of a solar thermal system using a novel flat spiral tube heat exchanger*. *Applied Thermal Engineering*, *159*, 113900.

Assuncao, E., & Williams, S. 2013. *Comparison of continuous wave and pulsed wave laser welding effects*. Optics and Lasers in Engineering, 51(6), 674–680.

Assuncao, E., & Williams, S. 2014. *Effect of material properties on the laser welding mode limits.* Journal of Laser Applications, 26(1), 012008.

Assuncao, E., Williams, S., & Yapp, D. 2012. *Interaction time and beam diameter effects on the conduction mode limit.* Optics and Lasers in Engineering, 50(6), 823–828.

Bonacina, C., Comini, G., Fasano, A., & Primicerio, M. 1973. *Numerical solution of phase-change problems*. International Journal of Heat and Mass Transfer, 16(10), 1825–1832.

Brackbill, J. U., Kothe, D. B., & Zemach, C. 1992. *A continuum method for modeling surface tension.* Journal of Computational Physics, 100(2), 335–354.

Bunaziv, I., Akselsen, O. M., Ren, X., Nyhus, B., & Eriksson, M. (n.d.). *Laser Beam and Laser-Arc Hybrid Welding of Aluminium Alloys*.

Bunaziv, I., Dørum, C., Nielsen, S. E., Suikkanen, P., Ren, X., Nyhus, B., Eriksson, M., & Akselsen, O. M. 2020. *Laser-arc hybrid welding of 12- and 15-mm thick structural steel.* The International Journal of Advanced Manufacturing Technology, 107(5–6), 2649–2669.

Bunaziv, I., Hovig, E. W., Godinez Brizuela, O. E., Zhang, K., Ma, X., Ren, X., Eriksson, M., & Skjetne, P. 2024. *CFD modeling for predicting imperfections in laser welding and additive manufacturing of aluminum alloys.* Journal of Laser Applications, 36(3), 032010.

C Mills, K. (n.d.). *Recommended values of thermophysical properties for selected commercial alloys*. Woodhead Publishing Limited. online.<https://books.google.ca/books?hl=en&lr=&id=GaOooR231aAC&oi=fnd&pg=PR7&dq=Mills,+K.C.+Recommended+Values+of+Thermophysical+Properties+for+Selected+Commercial+Alloys%3B+Woodhead+Publishing+Ltd.:+Cambridge,+UK,+2002&ots=WnKzPiotuA&sig=80VxhRUY84UJjy2Exa8LA6paY6g&redir_esc=y#v=onepage&q&f=false>.

Cai, J., Jin, H., Ouyang, Z., Guo, K., Wei, Y., & Chen, J. 2025. *Study on asymmetric forming and performance strengthening mechanisms of 6061-T6 aluminum alloy joints fabricated by oscillating laser based on keyhole characteristics and molten pool dynamic behaviors.* International Journal of Thermal Sciences, 207, 109377.

Cavilha Neto, F., Pereira, M., dos Santos Paes, L. E., & Fredel, M. C. 2021. *Assessment of power modulation formats on penetration depth for laser welding*. Journal of the Brazilian Society of Mechanical Sciences and Engineering, 43(6), 286.

Chen, G., Liu, J., Shu, X., Gu, H., & Zhang, B. 2019. *Numerical simulation of keyhole morphology and molten pool flow behavior in aluminum alloy electron-beam welding.* International Journal of Heat and Mass Transfer, 138, 879–888.

Cho, W.-I., Schultz, V., & Woizeschke, P. 2018. *Numerical study of the effect of the oscillation frequency in buttonhole welding.* Journal of Materials Processing Technology, 261, 202–212.

Courtois, M., Carin, M., Le Masson, P., Gaied, S., & Balabane, M. 2014. *A complete model of keyhole and melt pool dynamics to analyze instabilities and collapse during laser welding.* Journal of Laser Applications, 26(4), 042001.

Courtois, M., Carin, M., Masson, P. L., & Gaied, S. 2012. *Keyhole Formation During Spot Laser Welding. Heat and Fluid Flow Modeling in a 2D Axisymmetric Configuration*. 6.

Courtois, M., Carin, M., Masson, P. L., Gaied, S., & Balabane, M. 2013. *A new approach to compute multi-reflections of laser beam in a keyhole for heat transfer and fluid flow modelling in laser welding*. Journal of Physics D: Applied Physics, 46(50), 505305.

Cunningham, R., Zhao, C., Parab, N., Kantzos, C., Pauza, J., Fezzaa, K., Sun, T., & Rollett, A. D. 2019. *Keyhole threshold and morphology in laser melting revealed by ultrahigh-speed x-ray imaging*. Science, 363(6429), 849–852.

Dal, M., & Fabbro, R. 2016. [INVITED] *An overview of the state of art in laser welding simulation.* Optics & Laser Technology, 78, 2–14.

Duggirala, A., Kalvettukaran, P., Acherjee, B., & Mitra, S. 2021. *Numerical simulation of the temperature field, weld profile, and weld pool dynamics in laser welding of aluminium alloy*. Optik, 247, 167990.

Eshtayeh, M., Hijazi, A., & Hrairi, M. 2015. *Nondestructive Evaluation of Welded Joints Using Digital Image Correlation.* Journal of Nondestructive Evaluation, 34(4), 37.

Fetzer, F., Sommer, M., Weber, R., Weberpals, J.-P., & Graf, T. 2018. *Reduction of pores by means of laser beam oscillation during remote welding of AlMgSi.* Optics and Lasers in Engineering, 108, 68–77.

Frostevarg, J. 2018. *Factors affecting weld root morphology in laser keyhole welding.* Optics and Lasers in Engineering, 101, 89–98.

Gao, Z., Jiang, P., Mi, G., Cao, L., & Liu, W. 2018. *Investigation on the weld bead profile transformation with the keyhole and molten pool dynamic behavior simulation in high power laser welding.* International Journal of Heat and Mass Transfer, 116, 1304–1313.

Geiger, M., Leitz, K.-H., Koch, H., & Otto, A. 2009. *A 3D transient model of keyhole and melt pool dynamics in laser beam welding applied to the joining of zinc coated sheets.* Production Engineering, 3(2), 127–136.

Guo, W., Wan, Z., Peng, P., Jia, Q., Zou, G., & Peng, Y. 2018. Microstructure and mechanical properties of fiber laser welded QP980 steel. *Journal of Materials Processing Technology*, *256*, 229–238.

Hajavifard, R., Motahari, M., Özden, H., Miyanaji, H., & Kafashi, S. 2016. *The Effects of Pulse Shaping Variation in Laser Spot-Welding of Aluminum*. Procedia Manufacturing, 5, 232–247.

He, X., Elmer, J. W., & DebRoy, T. 2005. *Heat transfer and fluid flow in laser microwelding.* Journal of Applied Physics, 97(8), 084909.

Heider, A., Weber, R., Herrmann, D., Herzog, P., & Graf, T. 2015. *Power modulation to stabilize laser welding of copper.* Journal of Laser Applications, 27(2), 022003.

Herbinger, F., Bhouri, M., & Groulx, D. 2016. *Numerical study of a PCM-air heat exchanger's thermal performance.* Journal of Physics: Conference Series, 745, 032127.

Hong, K.-M., & Shin, Y. C. 2017. *Prospects of laser welding technology in the automotive industry: A review*. Journal of Materials Processing Technology, 245, 46–69.

Huang, L., Hua, X., Wu, D., & Li, F. 2018. *Numerical study of keyhole instability and porosity formation mechanism in laser welding of aluminum alloy and steel.* Journal of Materials Processing Technology, 252, 421–431.

Huang, Y., Xu, S., Yang, L., Zhao, S., Liu, Y., & Shi, Y. 2019. *Defect detection during laser welding using electrical signals and high-speed photography.* Journal of Materials Processing Technology, 271, 394–403.

Jia, Z., Zhang, P., Yu, Z., Shi, H., Liu, H., Wu, D., Ye, X., Wang, F., & Tian, Y. 2021. *Effect of pulse shaping on solidification process and crack in 5083 aluminum alloy by pulsed laser welding.* Optics & Laser Technology, 134, 106608.

Jiang, M., Chen, X., Chen, Y., & Tao, W. 2019. *Increasing keyhole stability of fiber laser welding under reduced ambient pressure.* Journal of Materials Processing Technology, 268, 213–222.

Katayama, S., Kawahito, Y., & Mizutani, M. 2010. *Elucidation of laser welding phenomena and factors affecting weld penetration and welding defects.* Physics Procedia, 5, 9–17.

Kawahito, Y., Mizutani, M., & Katayama, S. 2009. H*igh quality welding of stainless steel with 10 kW high power fibre laser*. Science and Technology of Welding and Joining, 14(4), 288–294.

Ke, W., Bu, X., Oliveira, J. P., Xu, W., Wang, Z., & Zeng, Z. 2021. *Modeling and numerical study of keyhole-induced porosity formation in laser beam oscillating welding of 5A06 aluminum alloy.* Optics & Laser Technology, 133, 106540.

Khedr, M., Hamada, A., Järvenpää, A., Elkatatny, S., & Abd-Elaziem, W. 2022. *Review on the Solid-State Welding of Steels: Diffusion Bonding and Friction Stir Welding Processes. Metals, 13(1), 54.*

Ki, H., Mazumder, J., & Mohanty, P. S. 2002. *Modeling of laser keyhole welding: Part I. mathematical modeling, numerical methodology, role of recoil pressure, multiple reflections, and free surface evolution.* Metallurgical and Materials Transactions A, 33(6), 1817–1830.

Kong, F., & Kovacevic, R. 2010. *Modeling of Heat Transfer and Fluid Flow in the Laser Multilayered Cladding Process.* Metallurgical and Materials Transactions B, 41(6), 1310–1320.

Kumar, P., & Sinha, A. N. 2018. *Studies of temperature distribution for laser welding of dissimilar thin sheets through finite element method.* Journal of the Brazilian Society of Mechanical Sciences and Engineering, 40(9), 455.

Kuo, Y., Yang, T., & Huang, G.-W. 2008. *The use of grey relational analysis in solving multiple attribute decision-making problems.* Computers & Industrial Engineering, 55(1), 80–93.

Lee, J. Y., Ko, S. H., Farson, D. F., & Yoo, C. D. 2002. *Mechanism of keyhole formation and stability in stationary laser welding.* Journal of Physics D: Applied Physics, 35(13), 1570–1576.

Li, Z., Yu, G., He, X., Li, S., Li, H., & Li, Q. 2019. *Study of thermal behavior and solidification characteristics during laser welding of dissimilar metals.* Results in Physics, 12, 1062–1072.

Lin, R., Wang, H., Lu, F., Solomon, J., & Carlson, B. E. 2017. *Numerical study of keyhole dynamics and keyhole-induced porosity formation in remote laser welding of Al alloys.* International Journal of Heat and Mass Transfer, 108, 244–256.

Liu, P., Huang, L., Gan, L., & Lei, Y. 2020. *Effect of plate thickness on weld pool dynamics and keyhole-induced porosity formation in laser welding of Al alloy.* The International Journal of Advanced Manufacturing Technology, 111(3–4), 735–747.

Ma, B., Gao, X., Huang, Y., Zhang, Y., & Huang, Y. 2024. *Effect of different pulse shapes on the laser welding of aluminum and copper.* Optics & Laser Technology, 171, 110312.

Mathivanan, K., & Plapper, P. 2019. *Laser welding of dissimilar copper and aluminum sheets by shaping the laser pulses*. Procedia Manufacturing, 36, 154–162.

Matsunawa, A. 2002. *Science of laser welding—Mechanisms of keyhole and pool dynamics.* International Congress on Applications of Lasers & Electro-Optics, 290.

Matsunawa, A., Kim, J.-D., Seto, N., Mizutani, M., & Katayama, S. 1998. *Dynamics of keyhole and molten pool in laser welding.* Journal of Laser Applications, 10(6), 247–254.

Matsunawa, A., Seto, N., Kim, J.-D., Mizutani, M., & Katayama, S. 2000. *Dynamics of keyhole and molten pool in high-power CO2 laser welding* (X. Chen, T. Fujioka, & A. Matsunawa, Eds.; p. 34).

Matsunawa, A., Seto, N., Kim, J.-D., Mizutani, M., & Katayama, S. 2001. *Observation of Keyhole and Molten Pool Behaviour in High Power Laser Welding: Mechanism of Porosity Formation and Its Suppression Method* (No. 1). Joining and Welding Research Institute, Osaka University.

Mayi, Y. A., Dal, M., Peyre, P., Bellet, M., Metton, C., Moriconi, C., & Fabbro, R. (n.d.). *An Original Way of Using COMSOL® Application Builder to Enhance Multiphysical Simulation of Laser Welding Processes*. 7.

Mayi, Y. A., Dal, M., Peyre, P., Bellet, M., Metton, C., Moriconi, C., & Fabbro, R. 2020. *Laser-induced plume investigated by finite element modelling and scaling of particle entrainment in laser powder bed fusion.* Journal of Physics D: Applied Physics, 53(7), 075306.

Medale, M., Xhaard, C., & Fabbro, R. 2007. *A thermo-hydraulic numerical model to study spot laser welding.* Comptes Rendus Mécanique, 335(5–6), 280–286.

Miller, W. S., Zhuang, L., Bottema, J., Wittebrood, A. J., De Smet, P., Haszler, A., & Vieregge, A. 2000. *Recent development in aluminium alloys for the automotive industry.* Materials Science and Engineering: A, 280(1), 37–49.

Mohanta, A., Leistner, M., & Leparoux, M. 2020. *Influence of temporal and spectral profiles of lasers on weld quality of titanium.* Optics and Lasers in Engineering, 134, 106173.

Moraitis, G. A., & Labeas, G. N. 2008. *Residual stress and distortion calculation of laser beam welding for aluminum lap joints.* Journal of Materials Processing Technology, 198(1–3), 260–269.

Nabavi, S. F., Farshidianfar, A., & Dalir, H. 2023. *A comprehensive review on recent laser beam welding process: Geometrical, metallurgical, and mechanical characteristic modeling.* The International Journal of Advanced Manufacturing Technology, 129(11–12), 4781–4828.

Okon, P. (n.d.). *Laser Welding of Aluminium Alloy 5083*.

Olsson, E., & Kreiss, G. 2005. *A conservative level set method for two phase flow.* Journal of Computational Physics, 210(1), 225–246.

Omoniyi, P., Acharya, U., Akinlabi, S., Jen, T.-C., & Akinlabi, E. 2025. *Taguchi-Grey relational analysis driven multi-objective optimization of weld bead geometry and hardness in laser welded Ti6Al4V Alloy.* International Journal on Interactive Design and Manufacturing (IJIDeM), 19(1), 423–434.

Özişik, M. N. 1993. *Heat conduction* (2. ed). Wiley.

Pahamli, Y., Hosseini, M. J., Ardahaie, S. S., & Ranjbar, A. A. 2022. *Improvement of a phase change heat storage system by Blossom-Shaped Fins: Energy analysis.* Renewable Energy, 182, 192–215.

Pakrouh, R., Hosseini, M. J., Ranjbar, A. A., & Bahrampoury, R. 2015. *A numerical method for PCM-based pin fin heat sinks optimization.* Energy Conversion and Management, 103, 542–552.

Pang, S., Chen, L., Zhou, J., Yin, Y., & Chen, T. 2011. *A three-dimensional sharp interface model for self-consistent keyhole and weld pool dynamics in deep penetration laser welding.* Journal of Physics D: Applied Physics, 44(2), 025301.

Pang, S., Chen, W., & Wang, W. 2014. *A Quantitative Model of Keyhole Instability Induced Porosity in Laser Welding of Titanium Alloy.* Metallurgical and Materials Transactions A, 45(6), 2808–2818.

Pang, S., Chen, W., Zhou, J., & Liao, D. 2015. *Self-consistent modeling of keyhole and weld pool dynamics in tandem dual beam laser welding of aluminum alloy.* Journal of Materials Processing Technology, 217, 131–143.

Pang, S., Chen, X., Li, W., Shao, X., & Gong, S. 2016. *Efficient multiple time scale method for modeling compressible vapor plume dynamics inside transient keyhole during fiber laser welding.* Optics & Laser Technology, 77, 203–214.

Panwisawas, C., Perumal, B., Ward, R. M., Turner, N., Turner, R. P., Brooks, J. W., & Basoalto, H. C. 2017. *Keyhole formation and thermal fluid flow-induced porosity during laser fusion welding in titanium alloys: Experimental and modelling.* Acta Materialia, 126, 251–263.

Qin, Y., Dai, G., Wang, B., Ni, X. W., Bi, J., & Zhang, X. H. 2011. *Investigating the effect of gravity on long pulsed laser drilling.* Optics & Laser Technology, 43(3), 563–569.

Quintino, L., Costa, A., Miranda, R., Yapp, D., Kumar, V., & Kong, C. J. 2007. *Welding with high power fiber lasers – A preliminary study.* Materials & Design, 28(4), 1231–1237.

Ready, J. F. 1997. *Industrial Applications of Lasers* (second).

Ribic, B., Palmer, T. A., & DebRoy, T. 2009. *Problems and issues in laser-arc hybrid welding.* International Materials Reviews, 54(4), 223–244.

Saadlaoui, Y., Feulvarch, É., Delache, A., Leblond, J.-B., & Bergheau, J.-M. 2018. *A new strategy for the numerical modeling of a weld pool.* Comptes Rendus Mécanique, 346(11), 999–1017.

SaediArdahaei, S., & Pham, X.-T. 2024a. *Comparative Numerical Analysis of Keyhole Shape and Penetration Depth in Laser Spot Welding of Aluminum with Power Wave Modulation*. Thermo, *4*(2), 222–251.

SaediArdahaei, S., & Pham, X.-T. 2024b. *Toward Stabilizing the Keyhole in Laser Spot Welding of Aluminum: Numerical Analysis.* Materials, 17(19), 4741.

Schauer, D. A. 1977. *Thermal and dynamic effects in electron beam welding cavities* (No. UCRL-52331, 5313807; p. UCRL-52331, 5313807).

Schubert, E., Klassen, M., Zerner, I., Walz, C., & Sepold, G. 2001. *Light-weight structures produced by laser beam joining for future applications in automobile and aerospace industry.* Journal of Materials Processing Technology, 115(1), 2–8.

Steen, W. M., & Mazumder, J. 2010. *Laser Material Processing*. Springer London.

Svenungsson, J., Choquet, I., & Kaplan, A. F. H. 2015. *Laser Welding Process – A Review of Keyhole Welding Modelling*. Physics Procedia, 78, 182–191.

Tan, W., Bailey, N. S., & Shin, Y. C. 2013. *Investigation of keyhole plume and molten pool based on a three-dimensional dynamic model with sharp interface formulation.* Journal of Physics D: Applied Physics, 46(5), 055501.

Tan, W., & Shin, Y. C. 2014. *Analysis of multi-phase interaction and its effects on keyhole dynamics with a multi-physics numerical model.* Journal of Physics D: Applied Physics, 47(34), 345501.

Tomashchuk, I., Bendaoud, I., Sallamand, P., Cicala, E., Lafaye, S., & Almuneau, M. 2016. *Multiphysical modelling of keyhole formation during dissimilar laser welding*. 8.

Tsai, M.-J., & Wu, L.-F. 2022. *Multi-Objective Optimization of Nd: YAG Laser Drilling of Optical-Grade Acrylic Plate Using Taguchi-Based Grey Relational Analysis.* Materials, 15(24), 8998.

Tsukamoto, S., Kawaguchi, I., Arakane, G., & Honda, H. (n.d.). *Keyhole Behaviour in High Power Laser Welding*.

Volpp, J., & Vollertsen, F. 2019. *Impact of multi-focus beam shaping on the process stability.* Optics & Laser Technology, 112, 278–283.

Wang, H., Shi, Y., & Gong, S. 2007. *Effect of pressure gradient driven convection in the molten pool during the deep penetration laser welding.* Journal of Materials Processing Technology, 184(1–3), 386–392.

Wang, L., Yao, M., Gao, X., Kong, F., Tang, J., & Jun Kim, M. 2023. *Keyhole stability and surface quality during novel adjustable-ring mode laser (ARM) welding of aluminum alloy.* Optics & Laser Technology, 161, 109202.

Wang, X., Liu, W., Xu, G., Zhu, J., Hu, Q., & Du, B. 2022. *Numerical analysis of dynamic coupling between the keyhole and molten pool in the rotating laser welding process of aluminum alloy.* The International Journal of Advanced Manufacturing Technology, 121(7–8), 5491–5502.

Wei, Z., Jin, G., & Wang, Y. 2016. *Numerical simulation of melt ejection during the laser drilling process on aluminum alloy by millisecond pulsed laser* (W. Bao & Y. Lv, Eds.; p. 979621).

Wen, X., Wu, D., Zhang, P., Liu, S., Luo, Z., Jia, Z., Ye, X., Shi, H., & Yu, Z. 2021. *Influence mechanism of the keyhole behavior on penetration depth by in-situ monitoring in pulsed laser welding of aluminum alloy.* Optik, 246, 167812.

Wu, D., Hua, X., Li, F., & Huang, L. 2017. *Understanding of spatter formation in fiber laser welding of 5083 aluminum alloy*. International Journal of Heat and Mass Transfer, 113, 730–740.

Wu, D., Hua, X., Ye, Y., Huang, L., Li, F., & Huang, Y. 2018. *Experimental and numerical study of spatter formation and composition change in fiber laser welding of aluminum alloy.* Journal of Physics D: Applied Physics, 51(18), 185604.

Xu, L., Tang, X., Zhang, R., Lu, F., & Cui, H. 2021. *Weld bead characteristics for full-penetration laser welding of aluminum alloy under electromagnetic field support.* Journal of Materials Processing Technology, 288, 116896.

Yang, L., & Jiang, H. 2021. *Weld defect classification in radiographic images using unified deep neural network with multi-level features.* Journal of Intelligent Manufacturing, 32(2), 459–469.

You, D., Gao, X., & Katayama, S. 2015. *Detection of imperfection formation in disk laser welding using multiple on-line measurements.* Journal of Materials Processing Technology, 219, 209–220.

Young, Z. A., Guo, Q., Parab, N. D., Zhao, C., Qu, M., Escano, L. I., Fezzaa, K., Everhart, W., Sun, T., & Chen, L. 2020. *Types of spatter and their features and formation mechanisms in laser powder bed fusion additive manufacturing process.* Additive Manufacturing, 36, 101438.

Yu, T., & Zhao, J. 2023. *Quantifying the mechanisms of keyhole pore evolutions and the role of metal-vapor condensation in laser powder bed fusion*. Additive Manufacturing, 72, 103642.

Zhang, D., Li, C., Liu, X., Cao, Y., & Wu, D. 2018. *Numerical study of spatter formation during fiber laser welding of aluminum alloy.* Journal of Manufacturing Processes, 31, 72–79.

Zhang, M., Wu, J., Mao, C., Cheng, B., Shakhawat, H. M. D., Li, H., Wang, K., Zhang, J., Hu, Y., & Bi, Z. 2022. *Impact of power modulation on weld appearance and mechanical properties during laser welding of AZ31B magnesium alloy.* Optics & Laser Technology, 156, 108490.

Zhang, T., Zhang, L., Zhang, C., Chen, X., & Li, J. 2021. *Physical study of spatter and melt pool dynamics during millisecond laser metals drilling.* Optics Communications, 482, 126627.

Zhang, T.-Z., Jia, Z.-C., Cui, H.-C., Zhu, D.-H., Ni, X.-W., & Lu, J. 2016. *Analysis of melt ejection during long pulsed laser drilling.* Chinese Physics B, 25(5), 054206.

Zhang, Y., Shen, Z., & Ni, X. 2014. *Modeling and simulation on long pulse laser drilling processing.* International Journal of Heat and Mass Transfer, 73, 429–437.

Zhang, Y.-X., Han, S.-W., Cheon, J., Na, S.-J., & Gao, X.-D. 2017. *Effect of joint gap on bead formation in laser butt welding of stainless steel.* Journal of Materials Processing Technology, 249, 274–284.

Zhao, H., Niu, W., Zhang, B., Lei, Y., Kodama, M., & Ishide, T. 2011. *Modelling of keyhole dynamics and porosity formation considering the adaptive keyhole shape and three-phase coupling during deep-penetration laser welding.* Journal of Physics D: Applied Physics, 44(48), 485302.

Zhou, J., Tsai, H.-L., & Wang, P.-C. 2006. *Transport Phenomena and Keyhole Dynamics during Pulsed Laser Welding.* Journal of Heat Transfer, 128(7), 680–690.